Aeroacoustics of Airborne Wind Energy Systems

N. Bouman

Technische Universiteit Delft

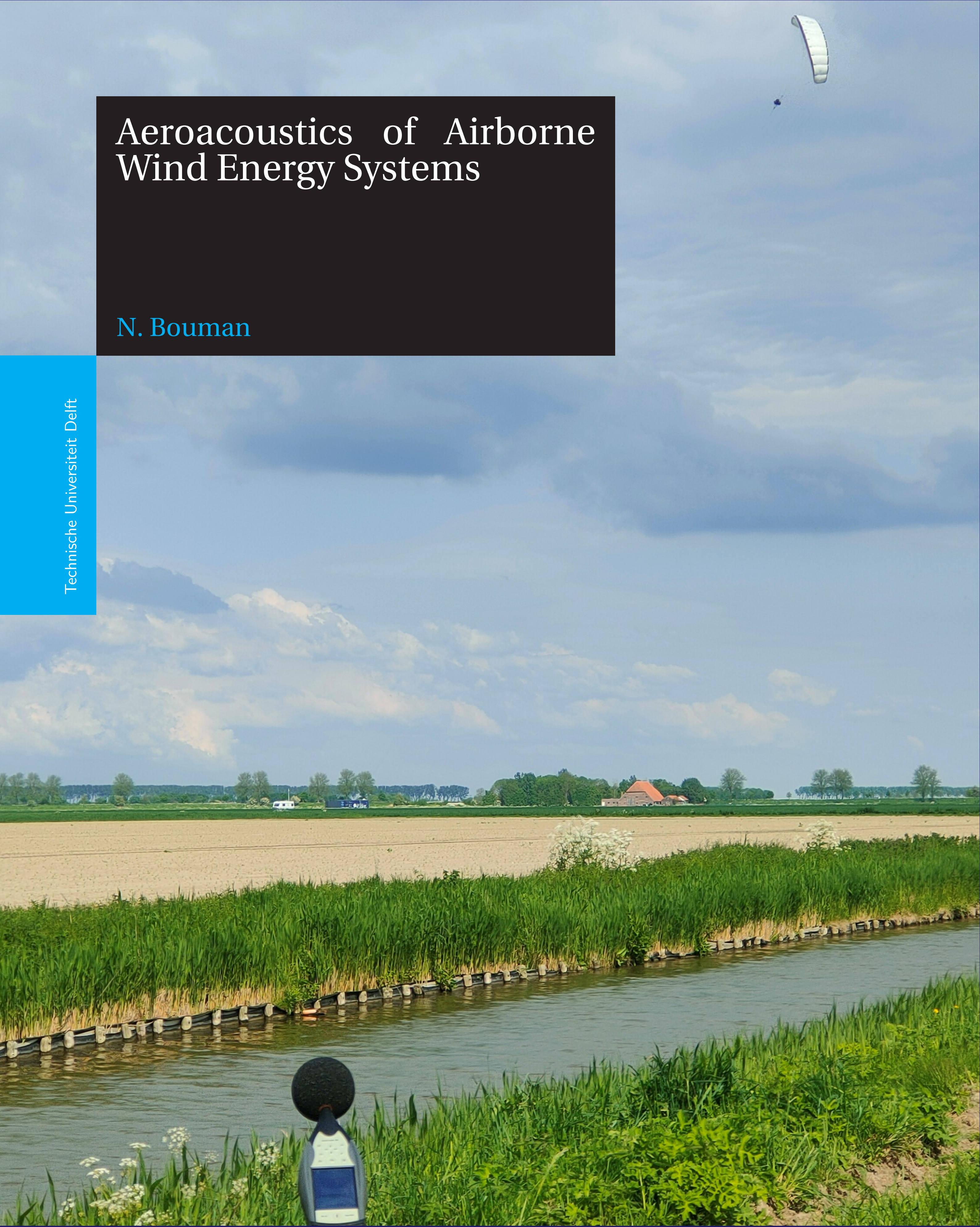

Delft University of Technology

Challenge the future

Note. The cover photo is taken in Dirksland, The Netherlands, showing the kite and microphone during the acoustic measurements at the test flight of Kitepower on May 12, 2023.

Aeroacoustics of Airborne Wind Energy Systems

by

N. Bouman

in partial fulfillment of the requirements for the degree of

Master of Science
in Aerospace Engineering

at the Delft University of Technology,
to be defended publicly on Wednesday June 28, 2023 at 13:00 PM.

Supervisor:	Dr.-Ing. R. Schmehl	
	Dr. D. Ragni	
Thesis committee:	Dr. ir. M. F. M. Hoogreef,	TU Delft
	Dr. R. Merino-Martinez,	TU Delft

PREFACE

I am pleased to present this report titled **"Aeroacoustics of Airborne Wind Energy Systems"**. The objective of this thesis is to identify the noise sources of airborne components in airborne wind energy systems that utilize a fixed-wing kite and a Leading-Edge Inflatable (LEI), soft kite. This research combines analytical simulations and experimental measurements to achieve its goals. The analytical simulations provide predictions of the noise spectra, which are then compared to the experimental results to identify the noise sources and differences between the two kite types. Additionally, this study aims to establish a foundation for future research in this emerging field and has the potential to contribute to noise reduction in airborne wind energy systems.

The intended audience of this report includes individuals and organizations involved in the field of airborne wind energy, ranging from companies working with these systems to researchers investigating the environmental impact and social acceptance of such systems. It also appeals to researchers interested in further exploring the aeroacoustics of airborne wind energy systems.

My motivation for undertaking this research stems from the increasing global demand for renewable energy sources and the need to address climate change. While wind energy is a well-established renewable energy source, traditional wind turbines face challenges such as noise and visual impact complaints, as well as logistical difficulties in transportation and installation. Airborne Wind Energy (AWE) systems offer a promising alternative by requiring less materials and being easily transportable. This research focuses on two AWE systems, namely the *Kitepower* system using a leading-edge inflatable kite and the *Kitemill* system using a fixed-wing kite.

One relevant aspect of AWE systems is the noise they generate, which affects not only (future) regulatory compliance, but also social acceptance and environmental impact. Therefore, this thesis concentrates on investigating the noise emissions, aiming to enhance our understanding of its acoustic characteristics and provide a basis for future noise regulations and noise reduction strategies.

Throughout the research process, several challenges were encountered. Limited resources related specifically to the acoustics of airborne wind energy systems required exploring related fields for valuable insights. Furthermore, the study relied on a limited number of measurements from *Kitepower* and *Kitemill*, emphasizing the need for more extensive data collection and analysis in future research efforts.

The key findings and recommendations resulting from this study offer valuable insights for the optimization and noise reduction of AWE systems. Notably, velocity control and targeted noise reduction strategies, such as modifying the tether or tripping the boundary layer, can help manage noise emissions and mitigate dominant noise sources.

I would like to express my sincere gratitude to *Kitepower* and *Kitemill* for their invaluable support throughout this research. Their willingness to provide access to their test sites, allow measurements, and share (flight) data, significantly contributed to the analysis. I would also like to extend my appreciation to my supervisors, who provided guidance and support throughout the entire research process.

I hope that this report serves as a valuable resource for researchers, industry professionals, and all those interested in the aeroacoustics of airborne wind energy systems. By addressing the noise challenges associated with AWE systems, we can further advance this exciting and promising technology to meet our renewable energy needs.

N. Bouman
Delft, June 2023

Abstract

Airborne wind energy systems offer a promising approach for renewable energy generation. However, the noise emissions associated with these systems should be understood and minimized as well to promote their integration and (social) acceptance. This thesis aims to identify the noise sources of airborne wind energy systems and establish a foundation for future research in this field. Analytical simulations using the Brooks, Pope, and Marcolini model and the Amiet model were combined with experimental measurements conducted at *Kitepower* and *Kitemill* test sites.

The analysis of *Kitemill*'s airborne wind energy system revealed prominent peaks around 1500 Hz and 2000 Hz in the noise spectra, with the higher frequency peak observed at higher kite velocities. Analytical predictions indicated laminar boundary layer vortex shedding and tether vortex shedding as the main noise sources. The study also investigated the directivity of the turbulent boundary layer trailing edge noise, which revealed dipoles that exhibited slight deformations at higher frequencies.

For *Kitepower*'s system, noise analysis identified peaks in the sound pressure level around 300-400 Hz and 1000-2000 Hz. Analytical predictions highlighted turbulent boundary layer trailing edge noise and vortex shedding from the tether and bridle lines as the dominant noise sources. Differences between predictions and measurements were likely attributed to phenomena characteristic for soft kites not fully accounted for in the models.

The findings have implications for noise reduction strategies in airborne wind energy systems. Implementing velocity control mechanisms can help manage noise emissions, with lower velocities reducing noise for fixed-wing kites, as well as for soft kites. However, for soft kites also phenomena like trailing edge flutter and seam-rippling have to be investigated and taken into account to ensure this mitigation to have the desired effect. Refining analytical models, modifying the tethers, tripping the laminar boundary layer of fixed-wing kites, and reinforcing critical areas of soft kites are recommended possible noise reduction measures.

Furthermore, the research provides valuable insights for (future) regulatory compliance and minimizing the environmental impact of airborne wind energy systems. Limitations in the analytical methods and data collection were identified, emphasizing the need for future research to refine models, expand data collection, and investigate additional factors influencing noise emissions.

By considering the implications of these findings and addressing the identified research opportunities, the noise impact of airborne wind energy systems can be minimized, fostering their sustainable deployment and acceptance.

Acknowledgements

I would like to express my sincere gratitude to the following individuals and organizations who have contributed significantly to the successful completion of this research:

First and foremost, I want to express my appreciation to *Kitepower* and *Kitemill* for their invaluable support and collaboration. Their willingness to share their knowledge and data, provide access to their test sites, and allow me to take acoustic measurements during their test flights were essential to the completion of this study. I would like to extend my special thanks to Espen Oland and Thomas Hårklau of *Kitemill* for their hospitality and assistance during my stay in Norway. Additionally, I am grateful to Jonas Kampermann of *Kitepower* for his instrumental role in facilitating the tests, ensuring the success of the measurements.

I am very thankful to Daniele Ragni and Roland Schmehl of the TU Delft for their unwavering guidance, feedback, and support throughout the entire research process. Their expertise and insights have been extremely valuable in shaping the direction of this study and enhancing its quality.

I would like to express my appreciation to Roberto Merino Martinez for his contribution to this research as well. His support in providing the necessary measurement equipment, as well as his insightful discussions, tips, and feedback, have been helpful in the successful execution of the experimental aspects of this study.

I am grateful to the Aerospace Faculty of the TU Delft for their generous support and financial assistance, which made it possible for me to conduct measurements in Norway and access the necessary resources for this research.

I would like to extend my heartfelt thanks to Inge Gerrits for her unwavering support, companionship, and understanding. Her presence and willingness to listen to my challenges and study together have been a source of motivation and inspiration throughout this research journey. I am also grateful to Santiago Valencia for our shared study moments and dedication to our theses.

Finally, I would like to express my deepest appreciation to my partner, Morghana Heberle dos Santos, for her unending patience, understanding, and support. Her encouragement, belief in my abilities, and willingness to listen to my challenges have been of great influence in my research success. I would also like to thank my family, particularly my parents, for their constant support, unwavering faith in me, and assistance throughout my academic journey. Lastly, a special mention to my sister, Yvette Bouman, for providing me with the much-needed leisure time and diversion when I needed it the most. Even more so, for always being by my side to get me through tough times and support me in whatever way needed.

Their collective support and encouragement have played an essential role in the completion of this research, and I am truly grateful for their contributions.

Contents

1 Introduction 1
1.1 Research Questions . . . 2
1.2 Hypothesis . . . 2
1.3 Objective . . . 2

2 Literature Review 5
2.1 Airborne Wind Energy . . . 5
2.1.1 Kitemill . . . 6
2.1.2 Kitepower . . . 9
2.2 LEI Kite Deformation Modes . . . 12
2.3 AWES Noise . . . 14
2.3.1 Pioneering Study . . . 14
2.3.2 System Noise Sources . . . 15
2.3.3 Tether (and Bridle Lines) . . . 16
2.3.4 Fixed-Wing Kite . . . 19
2.3.5 Soft LEI Kite . . . 20
2.3.6 KCU (*Kitepower*) . . . 28
2.3.7 Propellers . . . 30
2.4 Sound Propagation . . . 31

3 Methodology 33
3.1 Analytical Methods . . . 33
3.1.1 Amiet Model . . . 34
3.1.2 BPM Model . . . 35
3.1.3 Boundary Layer Parameters . . . 37
3.1.4 Validation . . . 37
3.1.5 Sensitivity Analysis . . . 38
3.1.6 Tether Vortex Shedding Prediction Model . . . 39
3.2 Experimental Methods . . . 40
3.2.1 Test Setup . . . 40
3.2.2 Acoustic Measurement System . . . 44

4 Results 53
4.1 Experimental Results and Analysis . . . 53
4.1.1 Kitemill . . . 53
4.1.2 Kitepower . . . 57
4.2 Experimental-Analytical Comparison . . . 60
4.2.1 Kitemill . . . 61
4.2.2 Kitepower . . . 63
4.3 Key Findings . . . 66
4.3.1 Kitemill . . . 66
4.3.2 Kitepower . . . 67
4.4 Previous Study Comparison . . . 68

5 Discussion 69
5.1 Implications and Recommendations for AWE . . . 69
5.2 Limitations and Future Research . . . 70

6 Conclusion 73

A Soft LEI Kite Characteristics 75
A.1 Flow on 2D Flexible Sails . . . 75

B Boundary Layer Parameters **77**
B.1 Boundary Layer Thickness . . . 77
B.2 Displacement Thickness . . . 77
B.3 Momentum Loss Thickness . . . 77
B.4 Shape Factor . . . 78
B.5 Skin Friction Coefficient . . . 78

C Validation Analytical Methods **81**
C.1 Amiet Model . . . 81
C.2 BPM Model . . . 82
C.2.1 Turbulent Boundary Layer Trailing Edge Noise . . . 82
C.2.2 Laminar Boundary Layer Vortex Shedding Noise . . . 83
C.2.3 Bluntness Trailing Edge Vortex Shedding Noise . . . 84
C.2.4 Tip Vortex Formation Noise . . . 85

D Sensitivity Analysis Analytical Methods **87**
D.1 Input Parameters . . . 87
D.2 Amiet Model . . . 88
D.3 BPM Model . . . 90

NOMENCLATURE

SYMBOLS

a, d, e, h^*	model parameters used in the Amiet model	-
A	wing area	m^2
A, B	empirical functions or generic parameters	-
c	chord length	m
$\mathscr{C}$	Corcos' constant	-
c_f	skin friction coefficient	-
$C_{L,rms}$	root mean square lift coefficient	-
C_s	chord length of slat	m
d	diameter	m
$\overline{D}_h, \overline{D}_l$	directivity functions	-
f	frequency	Hz
F	tensile force	N
G_1, G_2, G_3, G_4, G_5	empirical function	-
H	shape factor	-
h	height	m
k_0	acoustic wavenumber	-
k_B	bending wavenumber	-
$K_1, K_2, \Delta K_1$	empirical functions	-
l, L	length	m
L_A	A-Weighted Overall Sound Pressure Level	dBA
l_c	spanwise correlation length	m
L_p	sound pressure level	dB
M	Mach number	-
n	numeric parameter	-
p	pressure	Pa
r	distance source to observer	m
Re	Reynolds number	-
R_T	ratio of time scales of p	-
St	Strouhal number	-
t	time	s
u	velocity profile boundary layer	m/s
U	velocity	m/s
u_τ	friction velocity	m/s
w	width	m

GREEK SYMBOLS

α	wing angle of attack	°
β	elevation angle (wind window projection)	°
β_c	Clauser's parameter	-
β_s	side slip angle	°
δ	boundary layer thickness	m
Δ	Zagarola and Smits's parameter in Amiet model	-
δ^*	boundary layer displacement thickness	m
ϵ	excessive length ratio	-
θ	the angle of a tether from perpendicular to the flow	°
θ	angle from perpendicular to flow in the vortex shedding of the tether	°
θ	momentum thickness boundary layer in the boundary layer parameters	m

λ[1]	line angle in the geometry of the kite	$^\circ$
λ	mass per unit length in the calculation of the natural frequency of a tether	kg/m
ν	kinematic viscosity	m^2/s
Π	Cole's wake parameter in Amiet model	-
ρ	density	kg/m^3
σ	standard deviation	-
τ_w	wall/skin shear stress	Pa
ϕ	azimuth (wind window projection)	$^\circ$
Φ_{pp}	power spectral density of surface pressure fluctuations	Pa^2/Hz
Ψ	angle parameter related to surface slope at TE	$^\circ$
ω	angular frequency	rad/s
Ω	vacuum bending wave Mach number	-

ABBREVIATIONS & ACRONYMS

ADC	Analog-to-Digital Converter	
AoA	Angle of Attack	$^\circ$
AWE(S)	Airborne Wind Energy (System)	
BLT	Blunt Trailing Edge	
BPF	Blade Passing Frequency	Hz
BPM	Brooks-Pope-Marcolini model	
CFD	Computational Fluid Dynamics	
DNS	Direct Numerical Simulation	
FFT	Fast Fourier Transform	
HPF	High-Pass Filter	
HTOL	Horizontal Take-Off and Landing	
KCU	Kite Control Unit	
LE	Leading Edge	
LEI	Leading Edge Inflatable	
OSPL	Overall Sound Pressure Level	dB
OASPL	A-Weighted Overall Sound Pressure Level	dBA
PWL	Sound Power Level	dB
PS	Pressure Side	
RAT	Ram Air Turbine	
RMS	Root Mean Square	
SPL	Sound Pressure Level	dB
SS	Suction Side	
STFT	Short Time Fourier Transform	
TE	Trailing Edge	
TIP	Tip of wing	
VS	Vortex Shedding	
VTOL	Vertical Take-Off and Landing	

SUB- & SUPERSCRIPTS

8	related to the figure eight movement of the kite
∞	free-stream
a	related to the typical characteristic aerodynamic frequency of the kite
BE	related to the bunny-ear deformation mode
CB	related to canopy buckling
$Collapse$	related to the collapse deformation mode

[1] Note that λ in Airborne Wind Energy theory generally refers to the tangential velocity.

d	related to the depower angle or diameter of cylinder in case of Reynolds number
eff	effective
FD	related to the general flight dynamics of the kite
$flat$	flattened
IDM	related to leading edge indentation
JF	related to jelly-fishing
k	related to the kite
LBL	laminar boundary layer
m	related to the measured inflow angle
max	maximum
N	Nyquist-Shannon sampling
p	pressure side
$peak$	peak
$proj$	projected
S or s	related to shedding or scattering
s	suction side for boundary layer parameters
s	sampling frequency for signal processing
SR	related to seam-rippling
t	related to the tether
TBL	turbulent boundary layer
TEF	related to trailing edge fluttering
vs	vortex shedding

1

INTRODUCTION

The concept of using kites to generate energy dates back to the early years of the 20th century. Several concepts were developed in that time that varied from kites that were used to deploy wind turbines at higher altitudes [1] to trains of large lifter kites that had been used for high altitude measurements by observatories around the world [2]. The idea of harvesting high altitude wind was concretized in the 1980s by Hermann Oberth, who proposed it as an alternative energy source [3]. Only a few years later, Miles L. Loyd laid the foundation for quantitative analysis of Airborne Wind Energy (AWE) systems [4].

In the early 2000s, interest in AWE technology renewed, spurred on by concerns about climate change and the need for renewable energy sources. Even more so, the desire to move from fossil fuels to renewable energy has been even increasing more within the last decade and becomes a more urgent topic every day [5, 6]. Currently, there are five major renewable energy sources, which include: solar energy, geothermal energy, wind energy, biomass and hydropower. This report takes a closer look into one of the fastest-growing energy sources in the world: wind energy [7]. Wind energy is commonly associated with towered wind turbines. Wind turbines have been around for multiple centuries now [8] and many improvements and innovations regarding wind turbines have been implemented, such as more efficient blade shapes and add-ons to reduce the produced noise [9]. However, despite these improvements, there still remain some downsides to wind turbines, which makes them not suitable for all applications and locations. Noise and visual impact complaints remain an issue for the building of wind plants. Additionally, those 80 meter tall wind turbines require a lot of material with a weight that can reach over 366 tons for a 3.45 MW turbine [10]. Also, transporting these heavy and large structures to their desired location requires a special and costly operation [11]. As a 20-foot wind turbine requires approximately 100 square foot of empty space surrounding it, in order to have optimum working conditions [12], one can imagine, it might not always be the best and most practical solution to place a wind turbine at a location to provide energy. This is where AWE systems could potentially provide a solution. The AWE system of *Kitepower* for example only requires little ground space, can be transported in one 20ft container and can be integrated into existing microgrids, such as batteries, solar, diesel or grid [13].

AWE is a wind energy technology that is based on a flying component, which are often blades or wings, that are attached to the ground by a tether and generate power. AWE systems are divided into two main categories: on-board power generation and ground power generation [14]. This research focuses on two systems which make use of ground power generation systems: *Kitepower BV* and *Kitemill AS*. The system used by *Kitepower* makes use of a Leading Edge inflatable (LEI) kite, while *Kitemill* makes use of a fixed-wing kite [15].

As the AWE systems are a relative new technology, there are no regulations yet related to noise emission as there are for wind turbines. However, as the technology is upcoming, there definitely will be regulations in the future.Therefore, this thesis focuses on the noise of the kite power system of *Kitepower* and *Kitemill*. As noise will not only play part in the regulations, but also in the (social) acceptance [16] and the environmental impact on its surroundings, it is important to obtain knowledge in this area.

The AWE system can be divided into different components. Each component can be analyzed separately for its expected noise characteristics. The focus for this research is into the airborne components of the system, which in general includes the tether and kite. It is important to understand the characteristics of the components, which is why each component and their acoustic characteristics will be discussed.

An analytical method is used to predict the noise spectra, and field experiments are carried out to measure the noise produced by the systems. Due to flight test limitations and time constraints, the field experiments are limited to a single weather condition and a single flight for each of the systems.

Ultimately, the goal of this research is to gain insight into the aeroacoutics of AWE systems and to establish fundamental knowledge for optimizing these systems to reduce their noise levels as much as possible.

This report is structured such that it first discusses the literature, which includes the AWE systems and its components, as well as the different aeroacoustic characteristics that one may encounter in AWE systems. The next chapter then discusses the methodology for both the analytical methods, as well as for the experimental methods. The analytical methods include the Amiet model for the directivity of the noise and the Brooks, Pope and Marcolini model for the airfoil self-noise components. The experimental methods present the test setup and the acoustic measurement system, meaning the measurement characteristics, as well as the signal processing of the audio. In the chapter following, the results of the experiments are analyzed and compared to the analytical methods, as well as a previous study. Eventually, the discussion follows, as well as some recommendations that are made based on the outcome of this research.

1.1. RESEARCH QUESTIONS

The main research question of this thesis is: *"What are the primary noise sources and acoustic properties exhibited by the airborne components of a fixed-wing kite system, as used by Kitemill, and of a soft, Leading Edge Inflatable (LEI) kite system, as used by Kitepower?"*

From the main research question, the sub-research questions, that follow, which shall be answered for both systems, are:

1. What are the distinct noise sources exhibited by the airborne components of the fixed-wing kite system used by *Kitemill* and the soft, LEI kite system used by *Kitepower*, and how do these sources contribute to the overall noise emissions?

2. What are the characteristics of the boundary layer at the trialing edge of the kite for the positions of the kite during normal operation?

3. How do the noise characteristics, including frequency spectra and sound pressure levels, differ between the fixed-wing kite system and the soft, LEI kite system?

4. What are the key factors influencing the noise characteristics of the airborne components in the *Kitemill* and *Kitepower* systems?

1.2. HYPOTHESIS

The following hypothesis was formulated for this study:

> The noise generated by the tether will significantly contribute to the overall noise emissions in both the *Kitepower* and *Kitemill* systems. Additionally, the *Kitepower* system is expected to exhibit turbulent boundary layer noise, while the *Kitemill* system is expected to primarily produce laminar vortex shedding noise.

1.3. OBJECTIVE

The objective of this thesis is to identify the noise sources of the airborne components of airborne wind energy systems that make use of a fixed-wing kite and a leading-edge inflatable, soft kite. This will be achieved through a combination of analytical simulations and experimental measurements. The analytical simulations will provide a prediction of the noise spectra, which will then be compared to the experimental results to identify the noise sources. This also makes it possible to identify the differences between the noise emitted by the two different kites. Additionally, the aim is to establish a foundation for future research in this area. As no research has been conducted in this field, the study aims to set the fundamentals for future investigations. This research results in potential implications for the improvement of the systems, as it can be used to reduce the noise production.

2

Literature Review

2.1. Airborne Wind Energy

The fundamental working principles in AWE technology are fly-gen and ground-gen. Fly-gen systems generate the electricity in the airborne subsystem, while ground-gen systems generate electricity on ground. Besides the fundamental working principles, there are more variations, such as design choices and methods of takeoff and landing. As for the design choices, the kite designs vary from fixed wing to soft wing and even hybrid wings. An overview of different concepts of AWE systems as the status of 2019 can be found in Figure 2.1. However, it is worth noting that the landscape within the airborne wind energy field has been undergoing rapid and significant changes since 2019, with continuous advancements, new technologies, and evolving system classifications shaping the current state of the field.

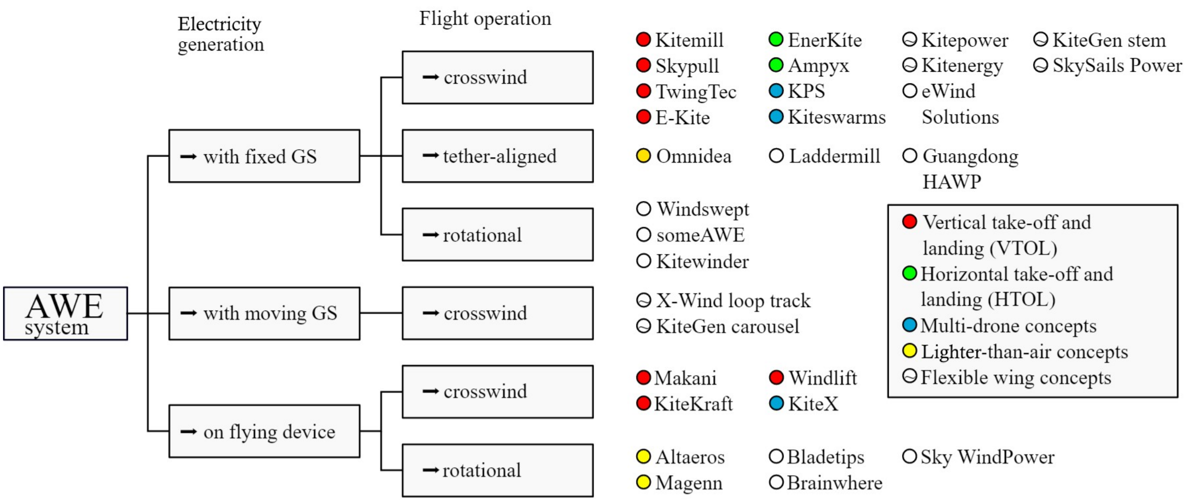

Figure 2.1: Overview of the classification of AWE systems as the status of 2019. Obtained from Schmehl [17].

The positions of the kite are indicated by using the ground station as a reference. The direction of the wind is indicated as upwind or downwind. The kite is only flown in the downwind area of the ground station. This area can be represented by a quarter spherical region, which is often referred to as the wind window. The angle between the downwind direction and the kite's perpendicular projection on the surface of the earth is the azimuth (ϕ) and the angle between the kite and the surface of the earth is the elevation (β).

Along the wind window of the kite, common phases and states can be indicated. Continuously flying towards the kite towards 12 o'clock is referred to as parking. In case the kite is flown to a more downward position in the wind window, it reaches the power zone, where the kite experiences the highest angle of attack (α) and therefore also the highest pulling force. In order to keep the kite close to the power zone, figure-of-eight or, in case of crosswind operation, circular patterns are flown. The figure-of-eight pattern can be performed in both an up-loop or down-loop manner. While flying these patterns, the tether is reeled off, which is referred to as the traction phase. The traction phase is then followed by the reel-in or retraction phase, which then results in a completed cycle.

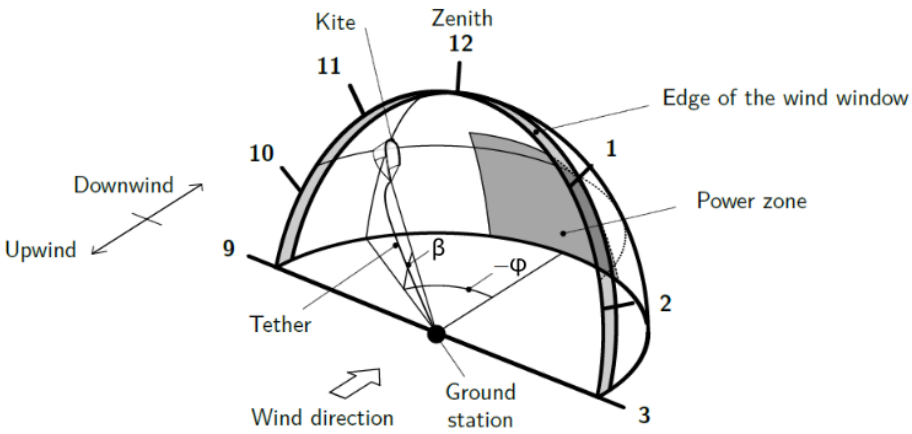

Figure 2.2: Wind window and basic terminology in the kite's flight envelope. Obtained from Friedl [18].

This report looks at two different types of kites: fixed-wing kite and soft, LEI kite. For the fixed-wing kite, the *Kitemill* kite is analyzed, while for the soft, LEI kite the kite of *Kitepower* is analyzed. Both kites are discussed in the next subsections. Additionally, also the flight envelopes and operational conditions are discussed of both systems.

2.1.1. KITEMILL

Kitemill is a Norwegian company working on the development of an AWES. *Kitemill*'s kite allows vertical takeoff and landing, also referred to as VTOL. Its design consists of a fixed-wing, vertical and horizontal stabilizers and four propellers. Out of these four propellers, two are in use during normal operation, while the remaining two allow for the VTOL procedures. The latest system of *Kitemill* is the KM1 system, which has a wingspan of 7.4 m [19] and a mean aerodynamic chord of 431.047 mm. The *Kitemill* KM1 kite is shown in Figure 2.3. The kite is attached to a tether, which has a diameter of 3.5 mm. The tether connects the kite to the winch, which allows for tether to be reeled-in or reeled-out. The tether and winch of the *Kitemill* system are shown in Figure 2.4. From Figure 2.4 it can be seen that a braided tether is used. To get a better idea of what a braided tether looks like from up close, Figure 2.5 is presented. The advantage of a braided tether is that it does not untwist when loaded [20], which is particularly relevant for the application of airborne wind energy systems.

Figure 2.3: *Kitemill* KM1 prototype. Obtained from Oland and Van der Brink [19].

The *Kitemill* KM1 kite flies at an average altitude of 220 m, where it flies a circular, crosswind trajectory. The trajectory can be seen in Figure 2.7, which includes both the traction and the retraction phase. During the traction phase, or production phase, the traction force is converted to electricity in the ground system. Once this phase is completed, the kite is withdrawn to the starting point during the retraction phase. During the flight tests in 2022, where the kite flew continuous cycles for more than one hour, shows the system reaches the targeted average of 20 kW and even already peaks beyond the 20 kW [21].

Figure 2.4: Tether and winch of the *Kitemill* system.

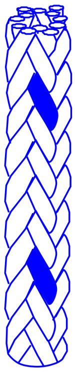

Figure 2.5: Braided tether. Obtained from Bosman et al. [20].

Taking a closer look at the kite, it can be observed that the airfoil along the wing span varies, due to the shape of the wing and the rounded wing tips. For research purposes the NACA6615 airfoil is used, due to the unavailability of proprietary airfoil data, as well as the NACA6615 airfoil showing great resemblance to the actual main airfoil used for the KM1 kite. The differences between the two airfoils can be seen from Figure 2.6.

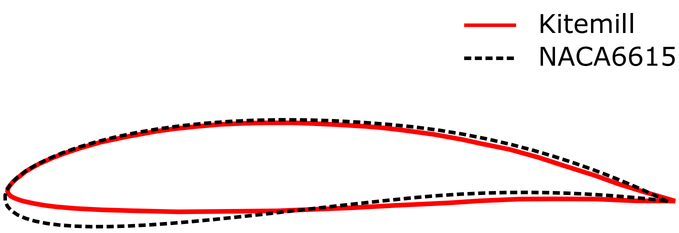

Figure 2.6: Comparison between the NACA6615 airfoil and the airfoil of *Kitemill*.

The characteristics of the kite, such as the velocity and angle of attack (AoA), are relevant pieces of information when trying to get an understanding of the sources of the noise generated by the system. During the test flight in June 2022, the measured airspeed of the kite was about 30 m/s to 50 m/s, as can be found in Figure 2.8a. For those same measurements, the altitude of the kite varied between approximately 160 meters to 300 meters (Figure 2.8b) and the tether length varied between 415 meters to 455 meters (Figure 2.8c) during the production phase. Additionally, the wind speed was measured to be around 9.26 m/s (Figure 2.8d). Although the angle of attack is not accurately measured by *Kitemill*, there are some estimates available, which show values varying from 0° to 10°.

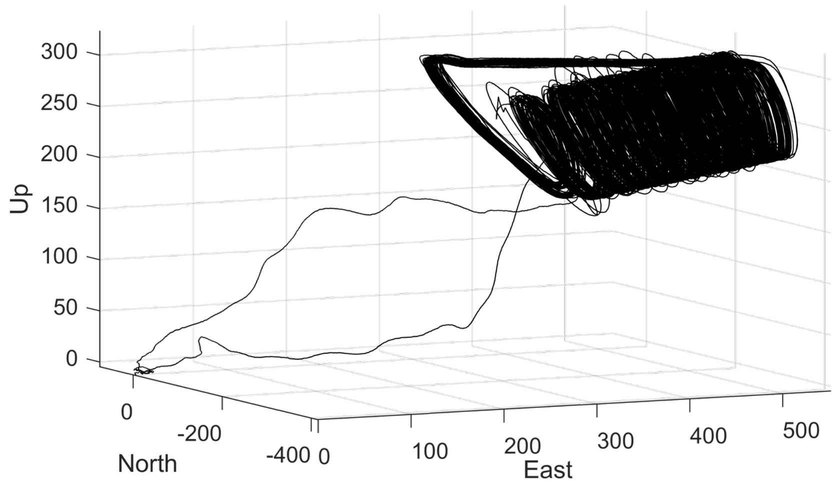

Figure 2.7: *Kitemill* kite trajectory. Obtained from *Kitemill* [21].

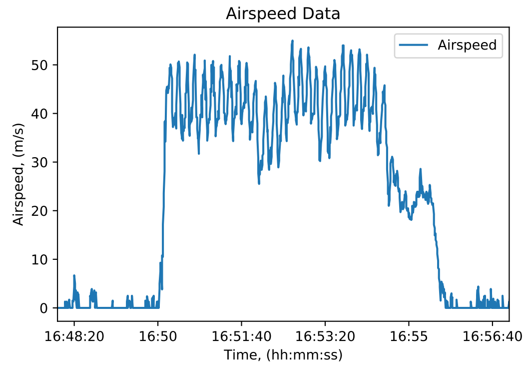

(a) Airspeed of kite

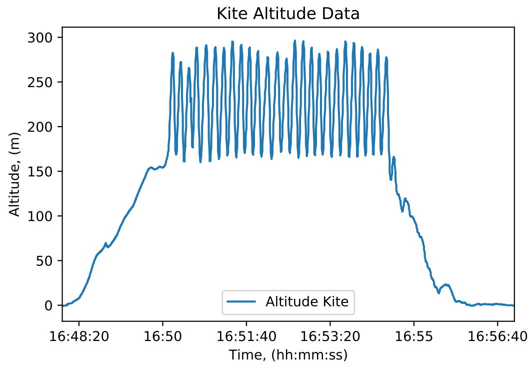

(b) Altitude of kite

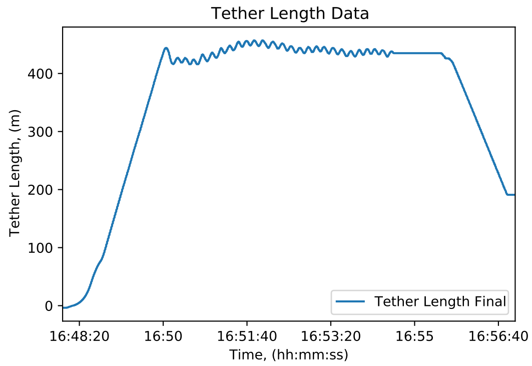

(c) Tether length

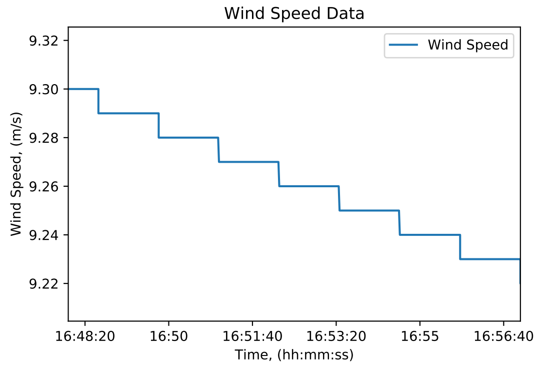

(d) Wind speed

Figure 2.8: Data measured during a test flight of *Kitemill* conducted in June 2022. Obtained from *Kitemill*.

2.1.2. KITEPOWER

The *Kitepower* system currently makes use of the 60 square meter kite V9.60, as shown in Figure 2.9. The kite has an arc-shape with inflated tube struts starting from the leading edge inflated tube to the trailing edge of the kite. Spanwise the kite is divided into thirteen canopy sections by twelve inflated tube struts. Out of these twelve inflated tube struts, two are located relatively close to half-span of the kite. This means that one of the thirteen canopy sections is considerably smaller than the other sections. The membrane out of which each canopy section consists, is a tensile structure with a very small thickness in comparison to the chordwise and spanwise length of the section. The V9.60 kite is part of the *Kitepower* Falcon system, which has a rated power of 100 kW [22].

Figure 2.9: Photo of the 60 m^2 compared to the smaller kite designs (25 m^2 and 40 m^2) of *Kitepower*. Obtained from *Kitepower* [23].

At the tips of the kite, the leading edge and the trailing edge join smoothly, leading to a chord length of 0 m at the tips. The projected area of the kite is $A_{proj} = 47\ m^2$ with a flattened area of $A_{flat} = 60\ m^2$. The largest strut is located at the center of the wing, which has a chord length of about 4 meters, while the smallest strut is located at the tip. The airfoil of the mid-strut of the V3 kite is shown in Figure 2.10. The airborne components of the kite power system are shown in Figure 2.12. Although the dimensions in Figure 2.12 are of the older 25 m^2 V3 kite design, the components and angle indication are still representative for the 60 m^2 kite design. As can be seen from Figure 2.12, the kite is attached to bridle lines, which are at their turn attached to the tether. The tether used for this specific research is a braided rope with a diameter of 14 mm [24], which has a similar structure are the braided tether presented in Figure 2.5. The bridle lines are present in a wide range of diameters, namely 2 mm, 3 mm, 4 mm, 5 mm, 6 mm and 8 mm.

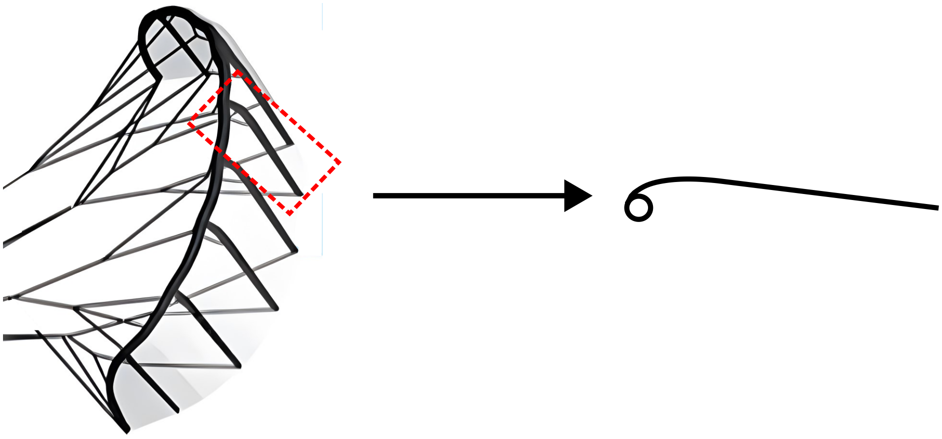

Figure 2.10: Visualization of the airfoil of the mid-strut of *Kitepower* LEI V3 kite.

The cycle of operation of the kite is also referred to as the pumping cycle, which can be divided into two phases, reel-out and reel-in, as shown in Figure 2.13. These two phases can be further divided into the following three states: reel out, reel in and transition states. During the reel out phase, the kite flies a figure-of-eight pattern. These flight phases and their respective height and ground distance from the perspective of the ground station are visualized in Figure 2.11.

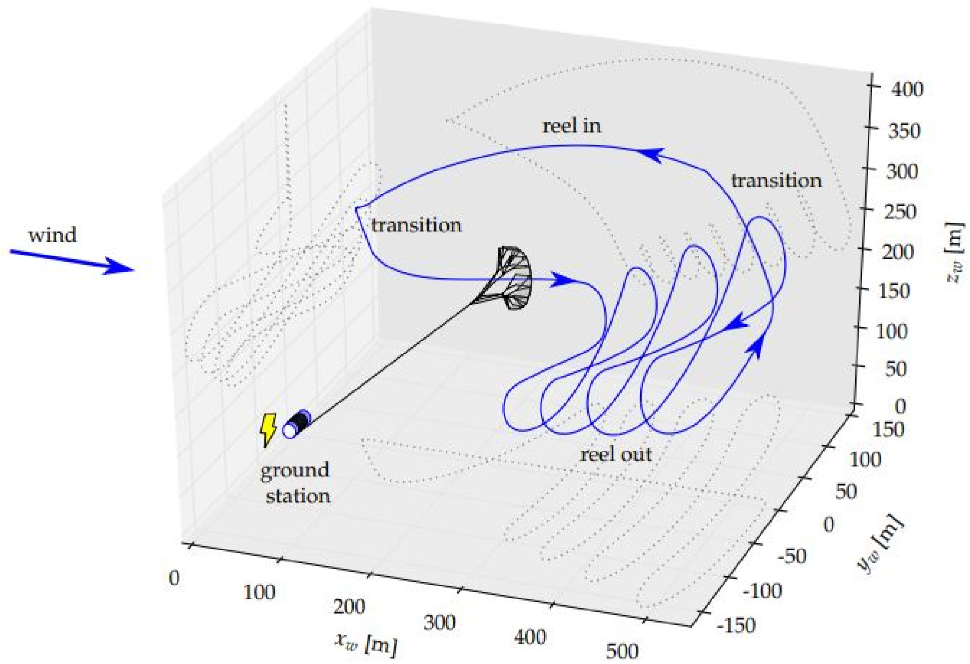

Figure 2.11: Computed flight path of a kite power system using a flexible wing with suspended kite control unit and single tether (kite and drum not to scale). Retrieved from Schmehl [17].

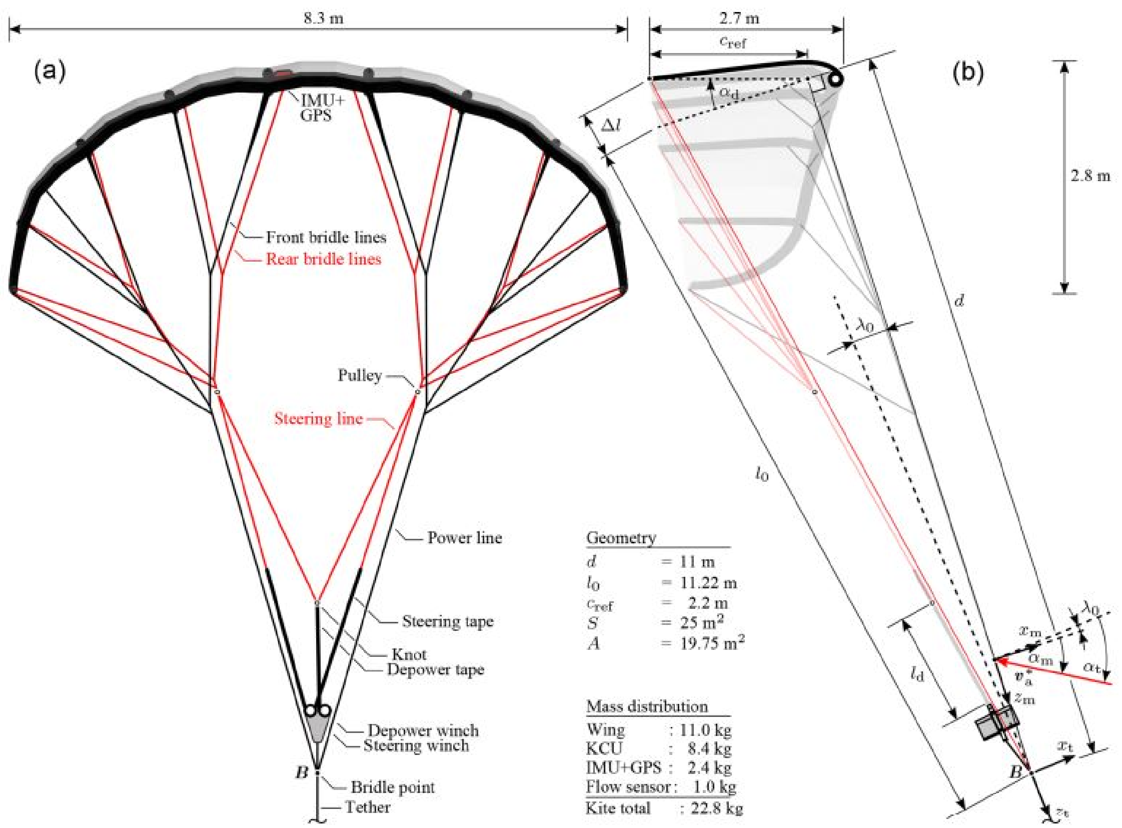

Figure 2.12: Front view (**a**) and side view (**b**) of the LEI V3 kite. Obtained from Oehler & Schmehl [25].

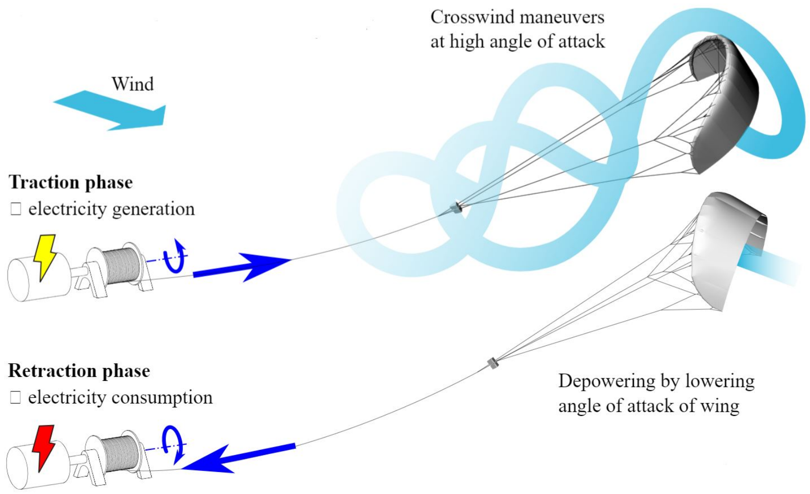

Figure 2.13: The reel-out (top) and reel-in (bottom) of the tether, combining to the periodic pumping cycles. Retrieved from Vlugt et al. [26].

From an aerodynamic perspective, the angle of attack of the kite is of interest. On March 24, 2017, a test flight was performed by *Kitepower* of which the results are available. Based on the results of the one hour test flight of the prototype of the LEI V3 kite [27], the range of angles of attack is obtained. The definition of the angle of attack of the relative flow with respect to the reference chord for these results is calculated from the measured inflow angle (α_m) and the depower angle (α_d):

$$\alpha = \alpha_m - \alpha_d. \tag{2.1}$$

Additionally, the angle of attack of the relative flow with respect to the tether angle of attack (α_t) is calculated as:

$$\alpha_t = \alpha_m + \lambda_0, \tag{2.2}$$

with λ_0 being the contribution of the line angle, which is caused by the pitch of the entire kite.

In total, the angle of attack thus consists of three contributions:

$$\alpha = \alpha_t - \lambda_0 - \alpha_d. \tag{2.3}$$

All mentioned angles are indicated in Figure 2.12.

The results of the test flight showing the lift-to-drag ratio over the angle of attack (α) is illustrated in Figure 2.14a. Important to note is that the angles of attack are defined as discussed earlier. The plot of Figure 2.14a can be divided into the two main flight phases: retraction and traction. For the retraction phase, a lower angle of attack region can be distinguished, being $-7° < \alpha < 3°$, while for the traction phase a higher angle of attack region can be distinguished, being $7° < \alpha < 15°$.

Besides the angle of attack, also the turning maneuvers of the kite are of interest, as they influence the flow over the kite. Steering induces deformation of the wing as well as possible additional drag and causes a change in side slip angle, which refers to the angle between the kite's flight direction and the wind direction. These factors attribute to a change in the flow over the kite. Figure 2.14b shows the results of the lift-to-drag ratio over the angle of attack colored by the steering intensity. This figure clearly shows that the high steering intensities mainly occur at angles of attack ranging from $9° < \alpha < 17°$. This coincides with higher steering intensities being applied during the traction phase of the flight.

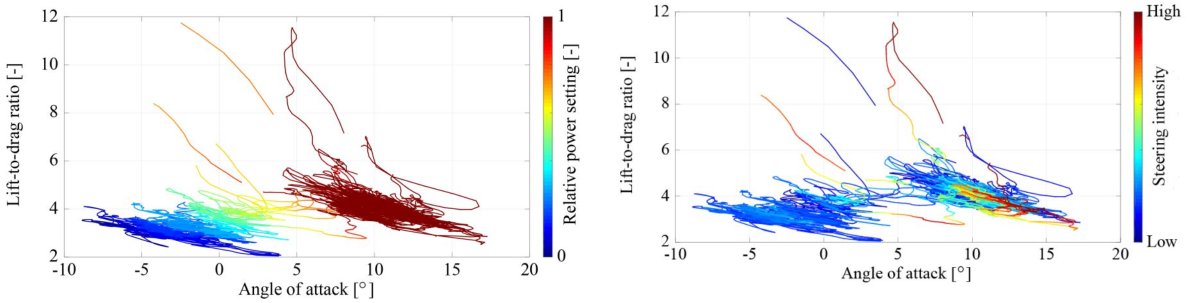

(a) Measured lift-to-drag ratio of the kite plotted over the angle of attack and colored by the relative power setting.

(b) Measured lift-to-drag ratio of the kite plotted over the angle of attack of the wing and colored by the steering intensity ranging from blue for no steering up to yellow and red for strong steering and turning maneuvers.

Figure 2.14: Plots relating to the angle of attack of the LEI V3 kite. Obtained from Oehler & Schmehl [25].

Next to the positions and movement of the kite, the velocity of the kite is an important factor for the characteristics of the airflow over the kite. The velocity of the kite has been analyzed for two different cases: moderate wind (5.9 m/s) and strong wind (9.9 m/s). These cases were measured on June 23, 2012 and August 23, 2012 and analyzed by Van der Vlugt et al. [28]. Figure 2.15 illustrates the flight velocity of the kite as measured during the experiment in 2012. It can be seen that for the moderate wind condition the kite velocity ranges between 10 m/s and 33 m/s, while for the strong wind condition the range becomes 18 m/s to 44 m/s.

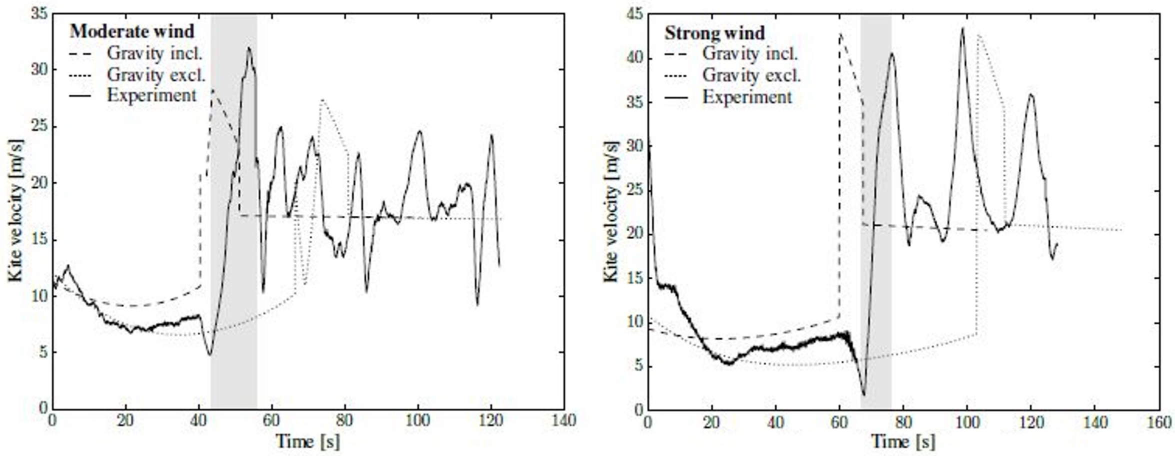

Figure 2.15: Flight velocity of kite over a full pumping cycle. Retrieved from Van der Vlugt et al. [28].

2.2. LEI KITE DEFORMATION MODES

Due to the geometry of the LEI kite and the flexible nature of the material, the kite membrane can mainly only resist tensile forces. As a consequence of this flexible characteristics of the kite, the kite deforms during operation. Deformation modes refer to the various ways in which a LEI kite can change its shape or exhibit structural deformations during operation. These deformation modes arise due to the flexible nature of the kite's material and the forces acting upon it. The kite's ability to resist primarily tensile forces means that it undergoes specific types of deformations under different conditions. In standard operation, a LEI kite experiences several deformation modes. The deformation modes can be classified from local to global and slow to fast. The global deformations, ordered from fast to slow are: canopy billowing, jellyfishing, bunny-ear flapping and leading edge indention, which can lead to the collapse of the kite. Likewise, the local deformations, ordered from generally fast to slow are: trailing edge flutter and seam-rippling. Note that the local deformations are usually faster than the global deformations.

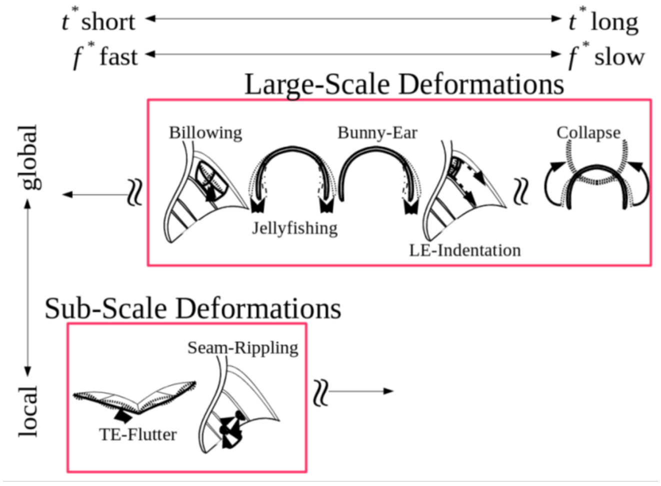

Figure 2.16: Typical kite deformation modes in normal pumping-cycle kite operation. Obtained from Leuthold [29].

Leuthold [29] has performed an analysis based on video footage of a flight test with the TU Delft KitePlane, geometrical data and flight path data to determine the relevant frequencies. A summary of this analysis is shown in Figure 2.17. Note that the grey-scale colors corresponds to flight-path frequencies, while the other colors correspond to deformation mode frequencies.

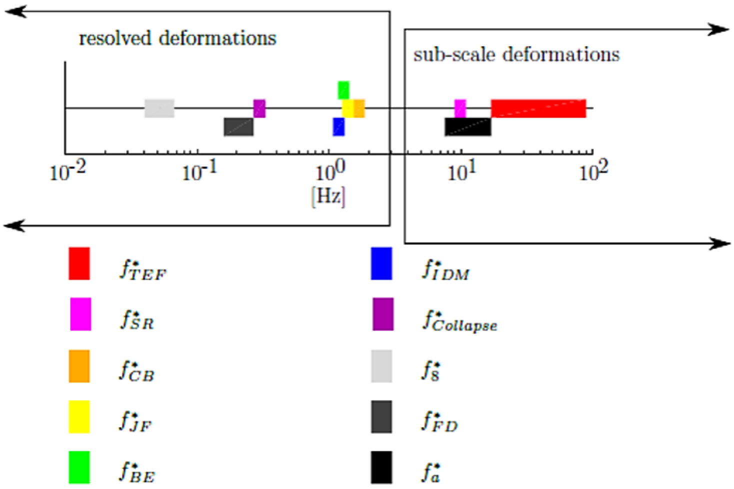

Figure 2.17: Summary of frequencies of typical kite deformation modes in normal pumping-cycle operation. Obtained from Leuthold [29].

As the audible frequencies range from 20 Hz to 20 kHz, the trailing edge flutter deformation mode is expected to be the main cause of noise of the kite due to deformation. Trailing edge flutter can be described as the deformation of the free trailing edge of the canopy of the kite, caused by the aerodynamic force oscillation due to vortex shedding. Seam-rippling, on the other hand, can be described as the occurrences of small waves or ripples near the struts of the structure, close to the trailing edge. Seam-rippling occurs, due to the tension along the wing's span being greater than the tension across the chord of the wing.

It is important to note that the kite is still in the research and development phase, which means it is anticipated to address and eliminate these deformations in the final product, ensuring their absence in the commercialized version.

2.3. AWES NOISE

Just as any technology that involves moving parts and fluid flows, noise is an inherent issue that must be addressed. Airborne wind energy systems are no exception to this. Noise emissions from AWES can have a significant impact on the environment and surrounding communities, affecting both wildlife and human health. Therefore, understanding the noise sources and characteristics of each component in an AWES is crucial.

This section focuses on providing a literature basis for AWES noise, discussing the pioneering study in which initial recordings were carried out, as well as the noise sources and characteristics of each component separately for which also the flow characteristics are taken into account.

2.3.1. PIONEERING STUDY

In 2017, Szücs [30] carried out the first research done into the environmental impact of the airborne wind energy system of *Kitepower*. Additionally, the dominant noise sources of the system were evaluated. In order to identify the dominant noise sources, Szücs performed noise measurements during a flight test at six different locations, which are displayed in Figure 2.18. An important remark is that the wind has not been excluded from the taken measurements, which is something that would be desirable in future measurements.

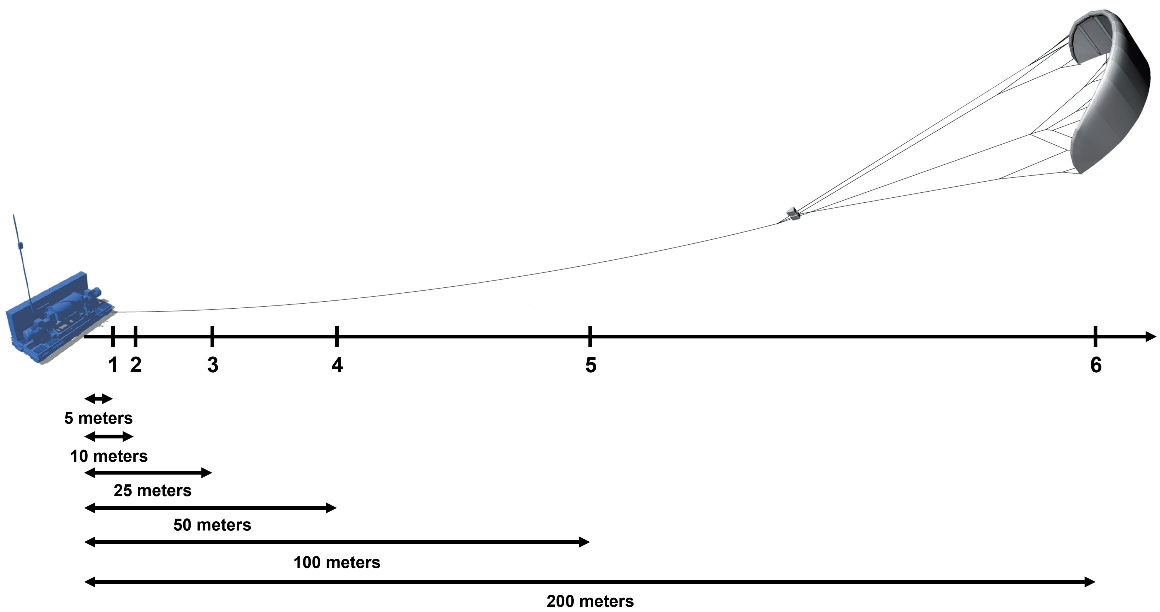

Figure 2.18: Illustration of setup of measurement by Szücs. Reproduced from Szücs [30].

At the measurement taken at location 2, high frequency noise was indicated due to the reel-in phase. This noise was labelled as the tether noise for a range between 500 Hz - 1000 Hz. Moreover, during the measurements the noise of the generator appeared to be dominant up to a distance of 25 meters (location 3). At 100 meters distance, some high frequency noise appeared again, which Szücs identified as noise from the kite itself. The periodical changes have been related to the movement of the kite, which can be seen in Figure 2.19.

From all measurements, Szücs was able to identify three zones with the different main sources of noise. Between 0 m to 38 m the generator and the tether are the main noise sources of the system. Between 38 m and 88 m the main noise source is solely the tether. Beyond 88 m up to 200 m, which was the furthest distance measured, the kite is the main noise source.

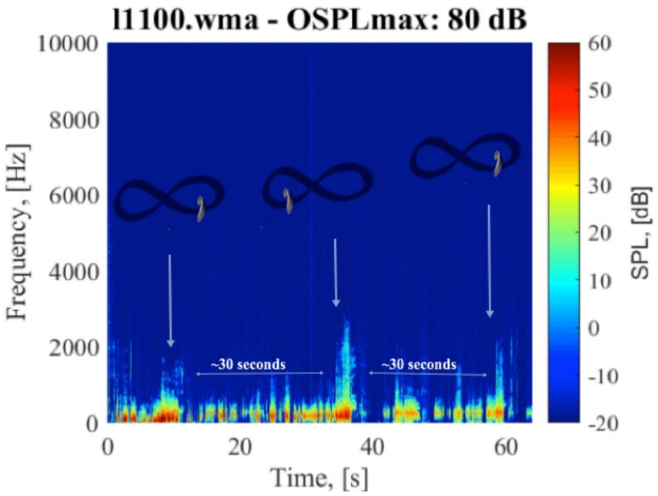

Figure 2.19: Measured noise at a distance of 100 meters from the generator, including the kite position and periodicity. Obtained from Szücs [30].

2.3.2. SYSTEM NOISE SOURCES

The research of Szücs, as discussed in Subsection 2.3.1, provides a basis for the noise emissions of the *Kitepower* system. Although the research showed some distances at which different components of the kite appeared to be dominant, it is not further looked at what specific characteristics of the kite and the airflow are responsible for this noise. Obtaining this knowledge results in the ability to predict the noise emissions of the components of the kite power system, as well as applying possible noise reduction methods.

When looking at the full system of *Kitepower* (as shown in Figure 2.20), four different types of noise sources can be distinguished: ground station/generator, tether and bridle, Kite Control Unit (KCU) including ram air generator/turbine and the kite. As this thesis will only focus on the airborne components of the kite power system, the ground station will be disregarded.

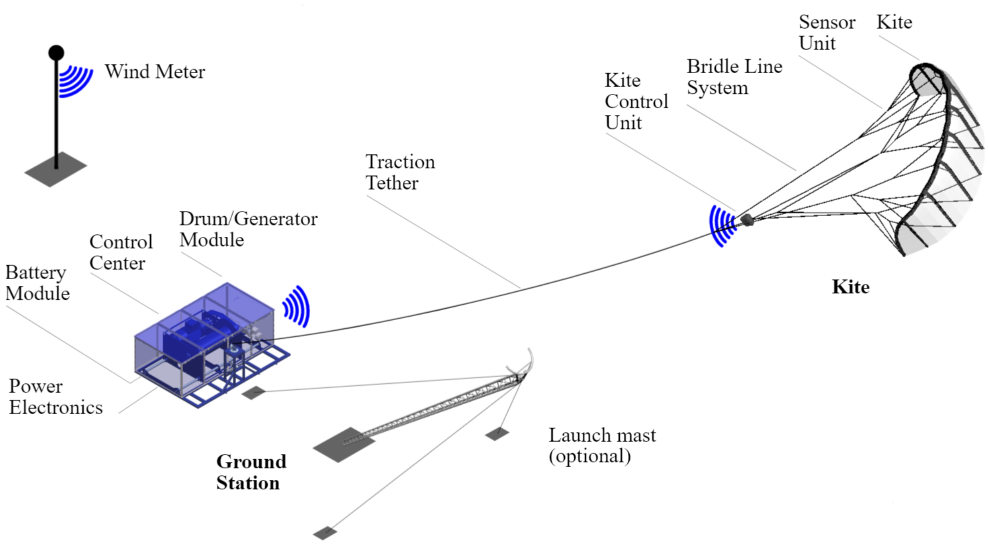

Figure 2.20: Illustration of the components of the kite power system of *Kitepower*. Retrieved from Van der Vlugt et al. [28].

The same can be done for the system of *Kitemill*, which is shown in Figure 2.21. From this system, three different types of noise sources can be distinguished: ground station, tether and kite. An important note here is that the kite contains four propellers, which are also a source of noise. However, these propellers are only required for take off and landing and can be mainly disregarded during most of the operation cycles. Once again, the focus will be on the airborne components of the system and therefore the ground station will be disregarded.

The next sections will discuss each of the mentioned components, which are analyzed regarding their flow characteristics to obtain an understanding of the present phenomena and thus the possible resulting noise generated. The first component that is analyzed is the tether (and bridle).

The second component analyzed is the KCU. The KCU is split into two parts: the KCU bullet and the turbine attached to the KCU. The third component that is analyzed is the kite. The noise sources of the kite are traced back to two sources: trailing edge scattering including flutter and tip noise. Additionally, the noise induced due to the recirculation zone has been analyzed to a limited extent due to a lack of available research.

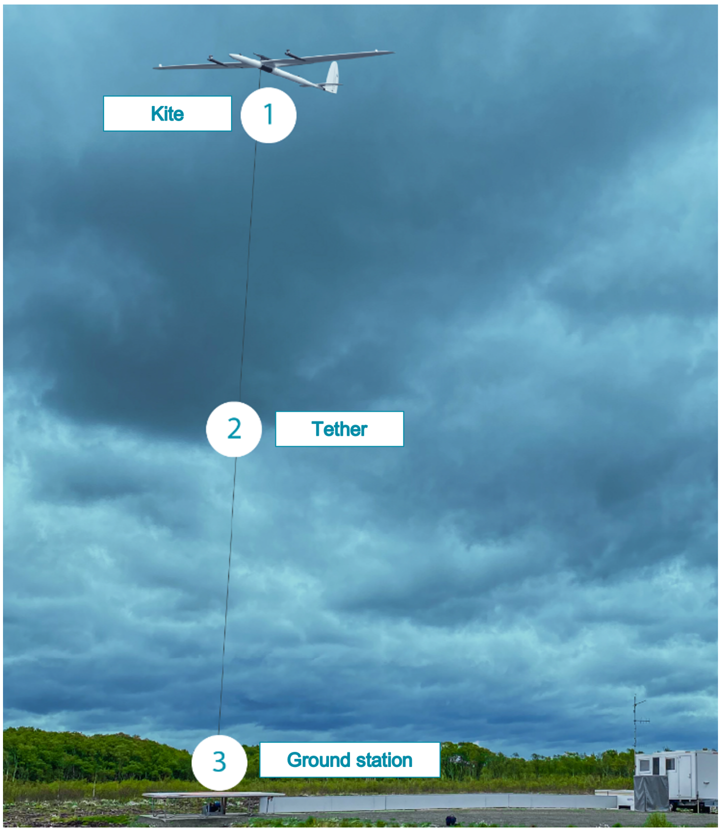

Figure 2.21: Photo of the components of the system of *Kitemill*. Obtained from *Kitemill* [31].

2.3.3. TETHER (AND BRIDLE LINES)

FLOW CHARACTERISTICS

Cylindrical bodies, such as a tether, that encounter a uniform flow, induce the development of coherent vortical structures in their downstream wake. The vortical structures are a result of the complex interactions between the airflow and the geometric features of the cylinder, leading to the generation of swirling patterns and turbulent eddies in the flow field. These vortical structures form a Von Kármán vortex street that consists of equally spaced vortices that are convected downstream at a constant speed. Visualization of this process is shown in Figure 2.22. At Reynolds numbers within the range $40 < \mathrm{Re}_d < 5 \cdot 10^4$, which is defined as $\mathrm{Re}_d = \frac{U_\infty d}{\nu}$, the vortical structures are found to shed periodically. For Airborne Wind Energy applications the relevant phenomenon is that of a fully turbulent vortex street, which occurs in the range from $300 < \mathrm{Re}_d < 2.9 \cdot 10^5$. The frequency of this vortex shedding is given by the Strouhal number, which is found by making use of the equation $\mathrm{St} = \frac{fd}{U_\infty}$. The Strouhal number can be approximated by $\mathrm{St} = 0.198(1 - \frac{19.7}{\mathrm{Re}_d})$, following the theory of Goldstein [32].

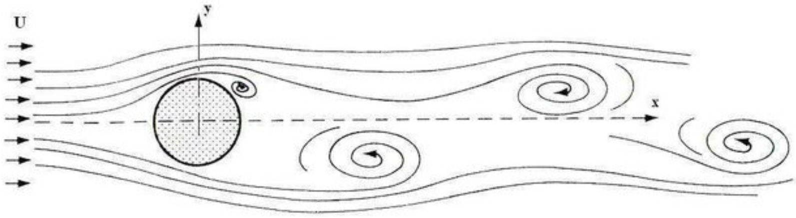

Figure 2.22: The vortex street that occurs behind a cylinder in a steady flow. Obtained from Cunha et al. [33].

NOISE CHARACTERISTICS

Vortex-Induced Vibrations are caused by unsteady flow separation from an elastic structure and the resulting cyclic variation of fluid forces. For Airborne Wind Energy systems the main implication is the case when the flow shedding frequency is in harmonic resonance with a natural frequency of the tether and bridle line system. This phenomenon is referred to as lock-in, which is the alignment of vortex shedding frequencies (f_s) with the natural frequency (f_n) of the vibrating structure. A common range as prone to lock-in is when $0.7 f_s > f_n > 1.3 f_s$, as mentioned by Dunker [34]. Across this range, the tether or bridle line experiences a near constant vibration at the nearest natural frequency.

The natural frequencies f_n of an elastic string are the integer multiples of the fundamental frequency, which can be formulated as follows:

$$f_n = \frac{n}{2l_t}\sqrt{\frac{F_t}{\lambda}}, \tag{2.4}$$

with $n = 1,2,3,...$ being the vibration node number, l_t the length of the string, F_t the tensile force and λ the mass per unit length.

For a vibrating string, a common assumption is that both ends of the string are fixed. However, for the kite power system, this is not the case as the upper end of the tether is attached to a flying kite moving in space and exerting a traction force on the tether. However, for the vibration dynamics, due to the mass of the kite compared to the tether, the kite is considered to be an end point with prescribed motion.

The tether of the *Kitepower* V3 kite is made of Dyneema® SK75, which has a diameter of 4 mm. Dyneema® SK75 has an approximate mass per unit length of $\lambda = 6.5 \cdot 10^{-6}$ kg/m per unit strength $F_t = 9.81$N. The general form to obtain the mass per unit length is thus: $\lambda = F_t \cdot \frac{6.5}{9.81} \cdot 10^{-6}$ kg/(Nm). This results in the following mass per unit length values for the different line tensions: $\lambda_{500N} = 0.00075$ kg/m, $\lambda_{5000N} = 0.01193$ kg/m, $\lambda_{50000N} = 0.09542$ kg/m according to Dunker [34]. By making use of these values and the equation given in Equation 2.4, the natural frequencies are obtained and presented in Table 2.1.

Line tension (N)	Length of tether or bridle line (m)		
	50	400	>400
500	8.2 Hz	1.0 Hz	<1.0 Hz
5000	6.5 Hz	0.8 Hz	<0.8 Hz
50000	7.2 Hz	0.9 Hz	<0.9 Hz

Table 2.1: Natural frequencies occurring for an Airborne Wind Energy System. Reproduced from Dunker [34].

However, according to King [35] the shedding frequency varies with inclination for angles of attack within 30 degrees of perpendicular with respect to the flow as follows:

$$f_{S,inclined} = f_{S,(\theta=0°)} \cdot \cos(\theta), \tag{2.5}$$

with θ being the angle from perpendicular to the flow.

An experiment has been conducted by Dunker [36], which investigates the impact of vortex induced vibration on kite lines. This experiment focused on the vibration correlated to the vortex shedding frequency dependent on the Strouhal number. Other sources of vortex induced vibration, such as galloping, Aeolian, or strumming vibration were not taken into account, as they were not reproducible during the testing. The test results confirmed that kite lines are susceptible to Strouhal vibration frequencies. Furthermore, it was observed that the vibration of the line was dependent on more than just the Strouhal number. A frequency increment existed between achieved Strouhal frequencies, which was equal to a couple of times more than the natural frequency of the lines. Additionally, the lock-in of a vibration frequency was observed at small ranges of airspeeds, where a single vibration frequency was maintained.

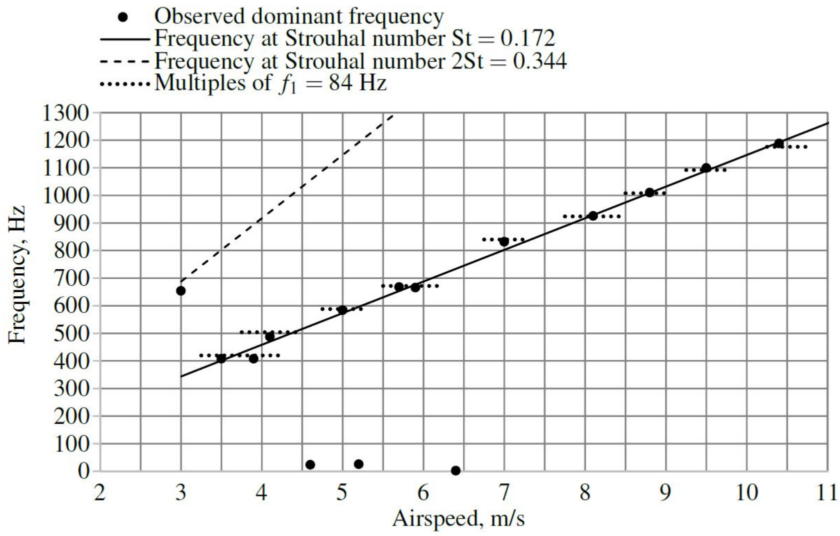

Figure 2.23: Dominant vibration frequencies and lock-in for Dyneema® line with d = 1.5 mm and α = 76.5° at Re = 300 to 1000. Obtained from Dunker [36].

Figure 2.23 shows that for a line with a diameter of 1.5 mm, the dominant vibration frequency matches a Strouhal number of St = 0.172. Also, the lock-in phenomenon is visible across certain velocity ranges of which 408 Hz and 665 Hz are examples. Moreover, a major secondary vibration frequency was observed at twice the shedding frequency, although they were not always the dominant frequencies. Both vibration modes are clearly visible in Figure 2.24, which represents the vibration spectrum map. The magnitude of the peaks in the vibration spectrum map represents the relative dominance of the vibration frequency.

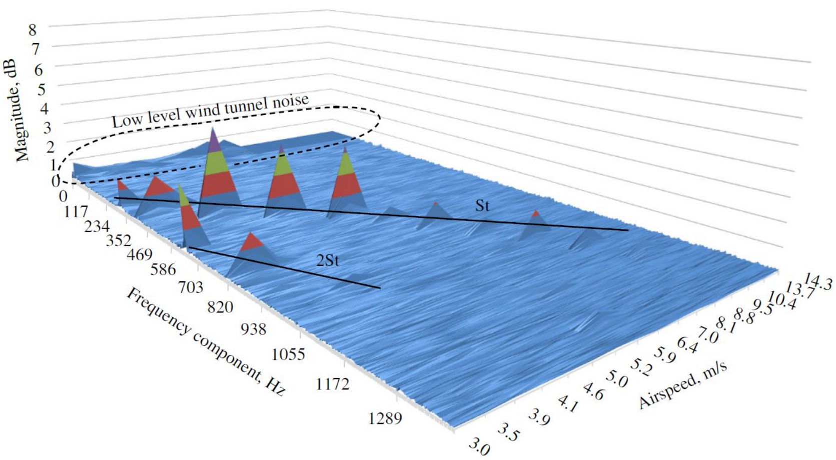

Figure 2.24: Vibration spectrum map for a Dyneema® line with d = 1.5 mm and α = 76.5°. Obtained from Dunker [36].

2.3.4. FIXED-WING KITE

There are different types of airfoil self-noise sources that can be identified, namely: turbulent boundary layer and laminar boundary layer trailing edge noise, separation/stall noise, trailing edge bluntness noise and tip vortex noise [37]. These different types of airfoil self-noise are also shown in Figure 2.25.

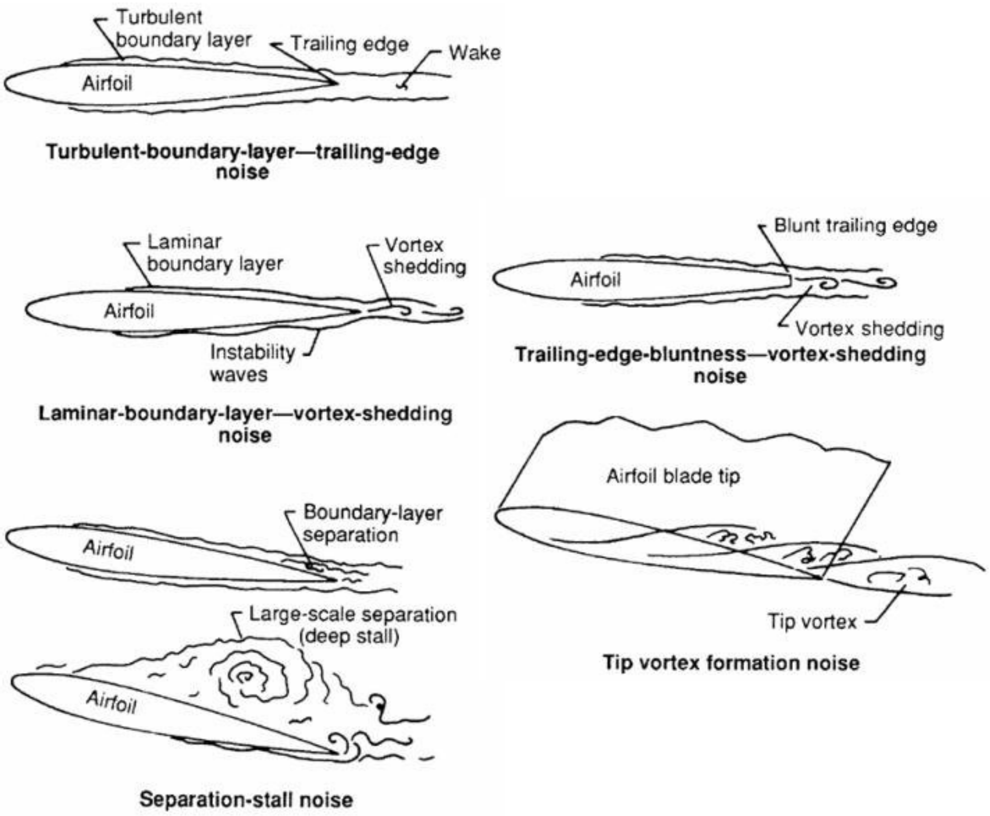

Figure 2.25: Airfoil self noise. Obtained from Brooks et al. [37].

Any arbitrary-shaped body placed in a turbulent flow will generate surface pressure fluctuations. These pressure fluctuations, when encountering a sharp trailing edge, will be scattered. The scattering results in the generation of acoustic energy and is propagated to the far field [38]. As mentioned by Lee et al. [39], certain types of trailing edge noise dominate at high frequencies, making them potential key elements that cause annoyance to human hearing. Trailing edge noise resulting from vortex shedding, such as laminar boundary layer noise and trailing edge bluntness noise, is known to generate tonal noise and is commonly associated with high-frequency emissions. These noise sources are also relevant for kites, emphasizing the importance of analyzing them in noise simulations. The diffraction of turbulent boundary layer trailing edge noise, on the other hand, generates broadband noise that extends to higher frequencies. In the lower frequency range, the suction side of the airfoil predominantly contributes to the noise emission, while the pressure side becomes dominant in the higher frequency range [40]. The intensity of the emitted sound is lower for the pressure side, which results in a decreasing pattern in the acoustic spectrum. An example of the spectrum of a turbulent boundary layer scattered by the trailing edge is shown in Figure 2.26. Over the years, several semi-analytical models for trailing-edge noise have been developed, which will be discussed in Section 3.1.

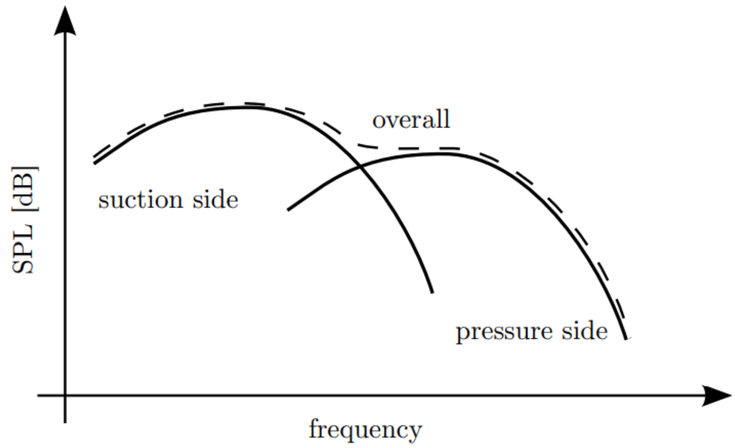

Figure 2.26: Illustration of the contribution of the pressure and suction side boundary layers to the overall acoustic spectrum. Obtained from Pröbsting [40].

Moreau and Doolan [41] performed an experimental study of airfoil tip vortex formation noise. The experiment consisted of taking aeroacoustic measurements of a finite airfoil with a flat ended tip in an anechoic wind tunnel. The results of this experiments show that compared to the total airfoil noise spectrum, the tip noise is dominant at high frequencies and shows a peak, which becomes steeper for increasing angles of attack. The broadband component of the tip noise indicates that the tip noise in the low and high frequency range is due to trailing edge scattering of vorticity in the tip region. Moreover, the frequency of the dominant tip noise contribution is observed to reduce, as the flow speed is decreased. Figure 2.38 shows the noise spectra of the total airfoil noise, as well as that of the tip, for a range of flow velocities and angles of attack.

2.3.5. SOFT LEI KITE

FLOW CHARACTERISTICS

Increasing the angle of attack of a membrane wing, results in an increase of the aerodynamic loading. This results in a deformation of the trailing edge of the membrane in the upward direction. The membrane wing therefore experiences an effective reduction in the angle of attack, due to the chord line being tilted tail-up and effectively nose-down, which is referred to as "adaptive washout". Lian et al. [42] confirmed this phenomenon of a decrease in effective angle of attack due to deformation of the membrane wing. A decrease in the effective angle of attack results in a delay of flow separation. However, the trailing edge of the kite is supported by a wire to provide tension and the inflated tubular structure, which causes a minimization of the experience of adaptive washout. The kite is therefore less prone to adaptive washout, although "adaptive camber", due to canopy flexibility, might still occur.

Nielsen [43] performed an experiment on flexible wings, which suggests that separation occurs when a membrane reaches an adaptive camber above 15%. However, Nielsen did not account for the leading edge cylinder that is included for the LEI kite. Mendenhall et al. [44] does include a prominent leading edge cylinder to a flexible membrane and showed that it results in a delay of leading edge separation to higher angles of attack. Important to note is that this delay is more noticeable for supercritical Reynolds numbers than for subcritical Reynolds numbers.

As the LEI kite flies at high angles of attack during the power generation phase, which results in a large wind-shadow behind the LEI tube, there will be flow separation. Newman and Low performed a study on separation and reattachment of flow on 2D, impermeable and flexible sails. From this study, three main separation types are found:

1. Pressure-side leading edge separation bubble (S_1)
2. Suction-side trailing edge separation region (S_2)
3. Suction-side leading edge separation bubble (S_3)

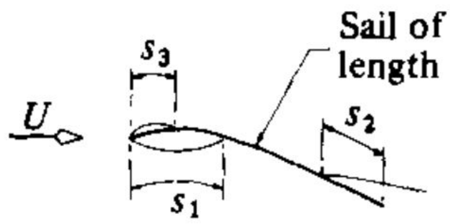

Figure 2.27: The dimensions of the three different types of separation. Retrieved from Newman & Low [45].

The results found by Newman and Low are shown in Figure A.1. The trends of these findings can be generalized into the following statements:

- Increasing the angle of attack results in a decrease of the separation bubble along the leading edge of the pressure-side.
- Increasing the angle of attack moves the separation bubble along the trailing edge suction-side forward.
- The leading edge separation bubble shows slightly different characteristics for the different excess-length ratios (ϵ). Primarily at moderate (5°) to large (25°) angles of attack the suction-side leading edge separation bubble occurs. Generally, at angles of attack smaller than 5°, no leading edge separation occurs, while at angles of attack around 20° to 25° the separation bubble merges to join the suction-side trailing edge separation region.

Moreover, Folkersma et al. [46] performed a computational fluid dynamic analysis of boundary layer transition on leading edge inflatable kite airfoils used for airborne wind generation. The study makes a distinction between two main phases, which are the retraction and traction phase. For the retraction phase, the Reynolds numbers are estimated to be around $10^5 \leq \mathrm{Re} \leq 7.5 \cdot 10^5$, while the Reynolds number for the traction phase is in the order from 10^6 to 10^8. Figure 2.28 shows the flow topology for some of the main characteristics of the flow of a LEI kite airfoil.

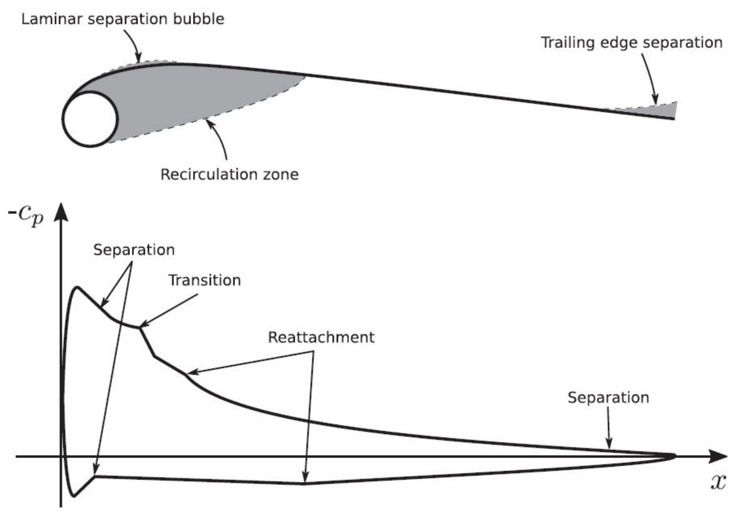

Figure 2.28: Flow topology around the leading edge inflatable (LEI) kite airfoil. Obtained from Folkersma et al. [46].

As can be seen from Figure 2.28, the suction side of the airfoil shows similar characteristics as that of a conventional airfoil. However, on the pressure side, a recirculation zone appears behind the leading edge tube. The size of the recirculation zone is dependent on the angle of attack and the Reynolds number.

The streamlines and normalized flow velocity around the LEI kite airfoil, generated by the CFD simulation of Folkersma et al. are shown in Figure 2.29 for different angles of attack and Reynolds numbers. It can be seen that for an increased angle of attack, the size of the recirculation zone decreases. For lower Reynolds numbers there appears to be a smaller secondary recirculation zone on the pressure side, which can be seen in Figure 2.29b (top). As the Reynolds number increases, this secondary recirculation zone disappears.

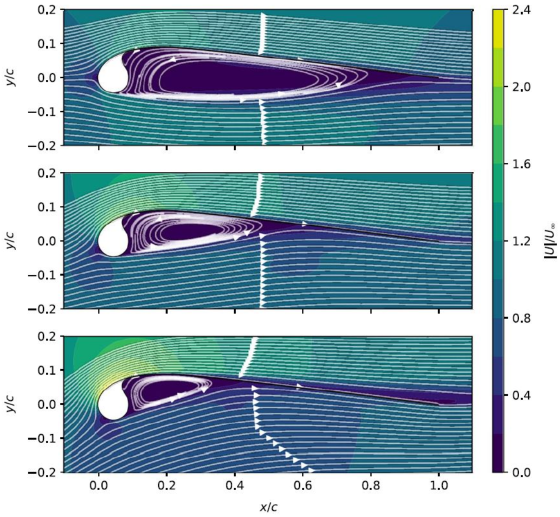

(a) Computed without transition modeling at Re = 10^6 for $\alpha = 0°$ (top), $\alpha = 6°$ (center), and $\alpha = 12°$ (bottom).

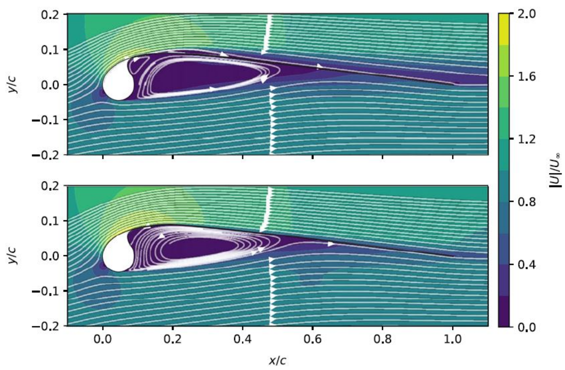

(b) Computed with transition modeling at $\alpha = 6°$ for Re = 10^5 (top) and Re = $5 \cdot 10^5$ (bottom).

Figure 2.29: Streamlines and normalized flow velocity around the leading edge inflatable (LEI) kite airfoil. Obtained from Folkersma et al. [46].

Furthermore, Folkersma et al. took a closer look into the location of the different flow regions. Based on the skin friction coefficient c_f, the transition, separation and reattachment regions are identified. Flow separation typically leads to a more significant increase in the skin friction coefficient compared to flow transition. This is because flow separation involves a complete detachment of the flow from the surface, resulting in a recirculation zone and a strong resistance in flow. In contrast, flow transition involves the development of turbulent fluctuations, which do increase the skin friction coefficient but to a lesser extent. Even more, flow separation often leads to a localized increase in the skin friction coefficient in the region where the flow separates from the surface. This is then observed as a distinct spike or peak in the coefficient at that specific location. On the other hand, flow transition effects a larger region on the surface, resulting in a more distributed increase in the coefficient along the surface. Additionally, also a negative friction coefficient can indicate a separation of the flow, as the separated flow can have a reverse flow direction or a flow with adverse pressure gradients, leading to a negative value of the skin friction coefficient in that particular region. Although, it should be noted that additional analysis is required to confirm the presence of a separation bubble, such as flow visualization.

The skin friction coefficient around a LEI wing at an angle of attack of 10° is given in Figure 2.30. It is observed that at Re = $5 \cdot 10^6$ no laminar separation bubble exists for the suction side. For the lower Reynolds numbers, the laminar separation bubble on the suction side starts around $x/c = 0.08$ with reattachment of the flow varying between $0.12 \leq x/c \leq 0.19$, which can be recognized from the negative skin friction coefficient in the plot for where the laminar separation bubble exists.

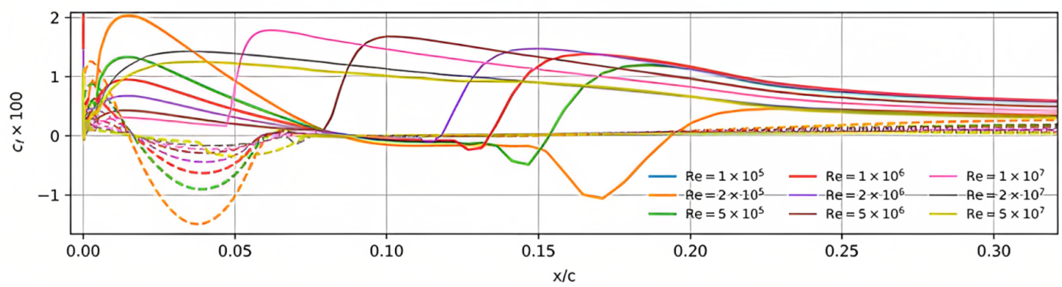

Figure 2.30: Friction coefficient around LEI wing at $\alpha = 10°$, computed with transition modeling. Solid line represents the suction side and dashed line the pressure side. Obtained from Folkersma et al. [46].

It should be noted however, that the analysis of Folkersma et al. assumes free boundary layer transition from laminar to turbulent. In practice, the flow will be tripped at the leading edge, due to the seams (see Figure 2.31). Therefore, the flow is always turbulent.

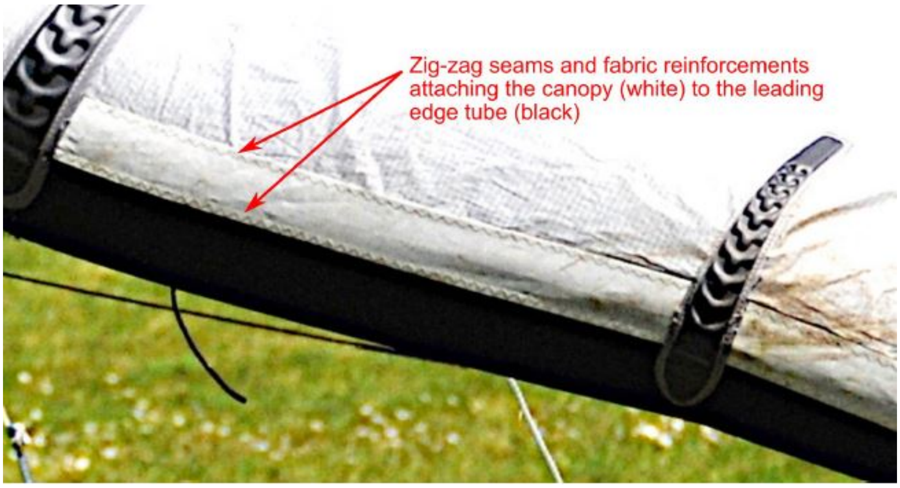

Figure 2.31: Zig-zag seams at the leading edge tube of the TU Delft V3 kite. Obtained from TU Delft [47].

NOISE CHARACTERISTICS

Trailing Edge Scattering

The fluttering trailing edge phenomenon of the kite already indicates that the trailing edge of the kite is not rigid, as would be the case for a conventional airfoil. The kite trailing edge is capable of producing trailing edge noise. Trailing edge noise is generated by the interaction of a sharp trailing edge with pressure fluctuations caused by aerodynamic turbulence. Due to a sharp discontinuity between two regions that exist at the trailing edge, pressure fluctuations are scattered form the trailing edge in the form of acoustic pressure waves.

Howe [48] analytically addressed the noise scattering phenomenon of a semi-infinite elastic plate in the presence of a turbulent boundary later, by making use of theoretical methods. Howe found in his work that besides the noise produced by the trailing edge scattering, additional noise was produced due to structural bending waves. The sound power levels generated by these bending waves are found to be quite large and can exceed the total sound power level from a rigid edge by 10-20 dB at low frequencies. Note that the precise amount depends on the frequency and the characteristics of the edge and flow.

Nardini et al. [49] followed up on Howe's paper and researched the effect of the structural compliance on the noise scattered from an elastic trailing edge by making use of high-fidelity direct numerical simulation (DNS). Nardini models aerodynamic fluctuations by placing a vortex generator in the form of a cylinder above the surface of a semi-infinite plate, within the boundary layer and upstream of the trailing edge. This vortex generator is chosen to mimic the vortex shedding produced by the laminar separation bubble of a NACA0012 airfoil at an angle of attack. However, unlike the airfoil under an angle of attack, the considered flat plate is kept at zero angle of attack. A schematic representation of the modeled pressure fluctuations is given in Figure 2.32.

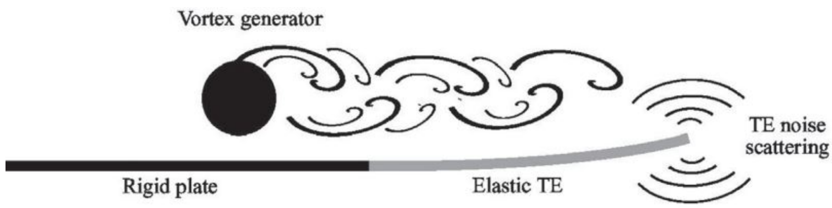

Figure 2.32: Schematic representation of the pressure fluctuations on the surface of an elastic trailing edge produced by boundary layer instabilities by the wake of a vortex generator. Obtained from Nardini et al. [49].

For a rigid trailing edge, the pressure field incident to the trailing edge represents the main input to the trailing edge scattered noise. However, for an elastic trailing edge, the contribution of the motion-induced pressure field cannot be neglected, as shown by Nardini et al. The total scattered acoustic pressure fluctuations (p'_s) for the elastic trailing edge is found to be decomposed into the contribution of a motion-induced acoustic scattered pressure field (p'_{s_f}) and an additional scattered pressure field (p_{s_i}), which is generated by the incident surface pressure only. As for a rigid trailing edge, there is no structural motion, the total scattered acoustic pressure fluctuations is equal to the scattered pressure field generated by the incident surface pressure.

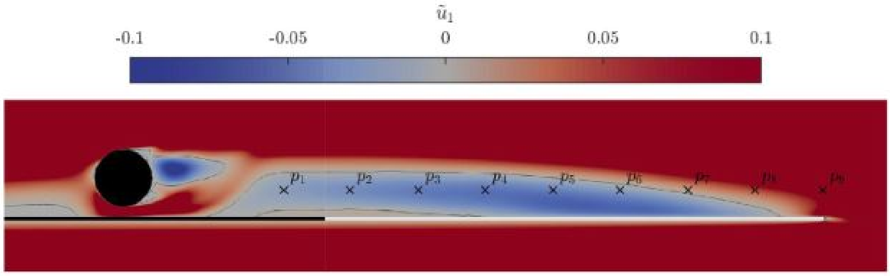

Figure 2.33: Recirculation region on the upper surface of the plate. The plate portion that is considered flexible is colored in white. Obtained from Nardini et al. [49].

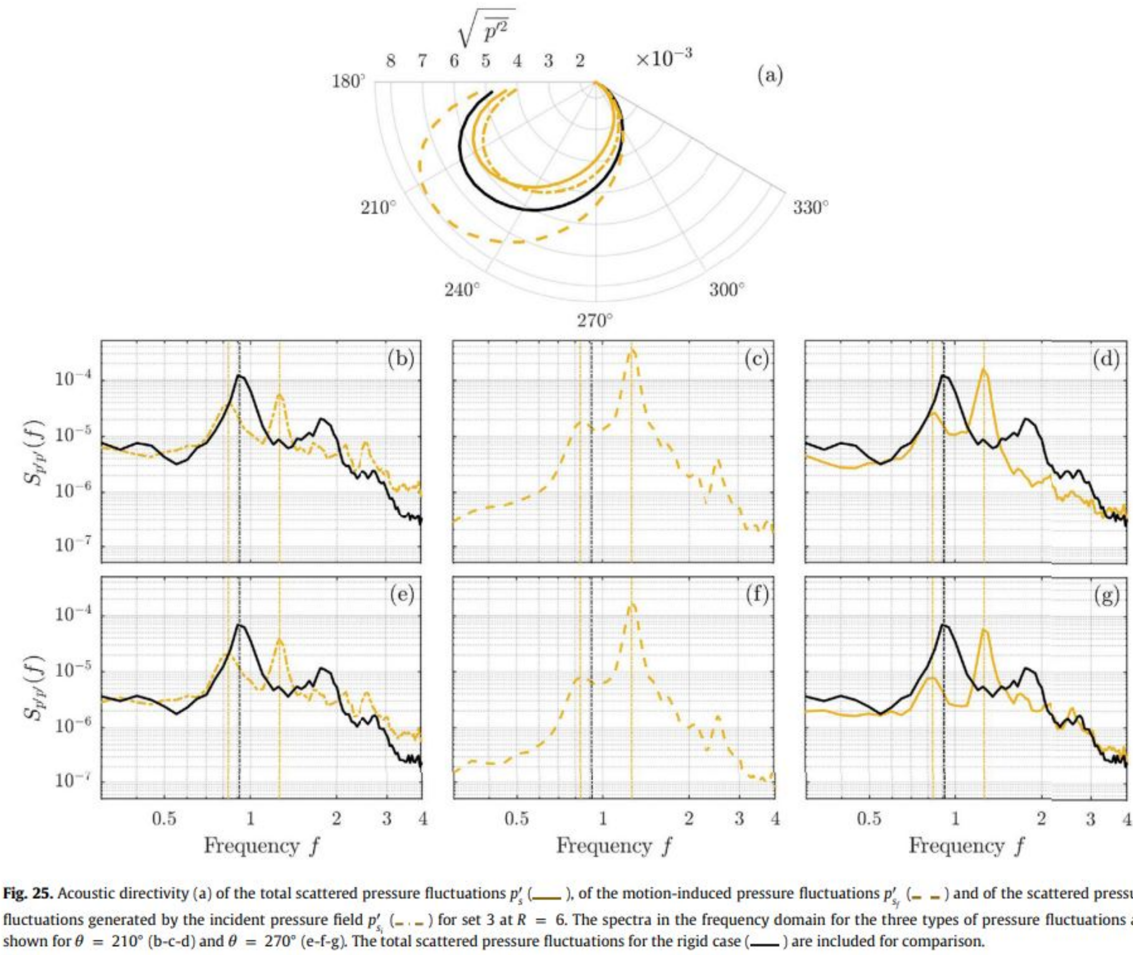

Figure 2.34: Acoustic directivity and frequency spectra of the total scattered pressure fluctuations, motion-induced pressure fluctuations and the scattered pressure fluctuations generated by the incident pressure field. Obtained from Nardini et al. [49].

The acoustic directivity and frequency spectra of the total scattered pressure fluctuations and its separate components of the test case used by Nardini et al. are shown in Figure 2.34. Comparing the acoustic directivity plot of the total scattered pressure fluctuations of the rigid and elastic trailing edge, which is given in Figure 2.34(a), it can be found that the structural motion of the elastic trailing edge produces an attenuation of the acoustic field due to the incident fluctuations with respect to the rigid case. The structural motion shows a large peak at the first structural frequency ($f_s = 1.42$) and a secondary peak at the recirculation frequency ($f_b = 0.91$), shown in Figure 2.34(c and f). Note that the recirculation region is considered to be the recirculation at the trailing edge as illustrated in Figure 2.33. In Figure 2.34, it can be observed that there appears to be a significant noise reduction with respect to the rigid trailing edge at the recirculation frequency, as for this frequency the elastic trailing edge appears to benefit from a cancellation effect. Simultaneously, at the first structural frequency an increase of the amplitude of fluctuations is present.

From Nardini et al. it is concluded that the aeroacoustic response of an elastic trailing edge depends on the complex fluid-dynamic interactions between the turbulent vortical structures of the incident wake and the unsteady deflection of the structure. The structural motion appeared to be responsible for an alteration of the incident surface pressure field as well as for excess noise at structural frequencies.

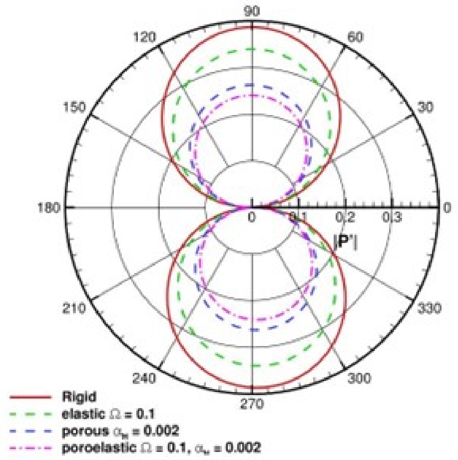

(a) $k_0 = 1$

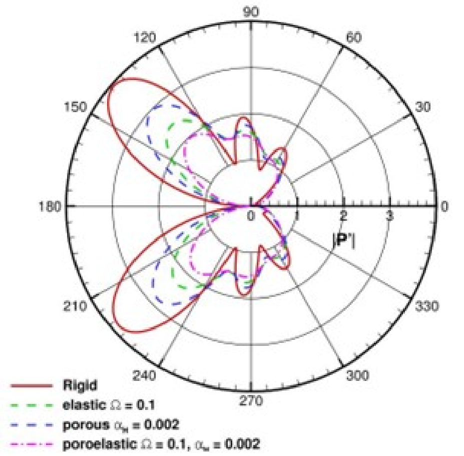

(b) $k_0 = 10$

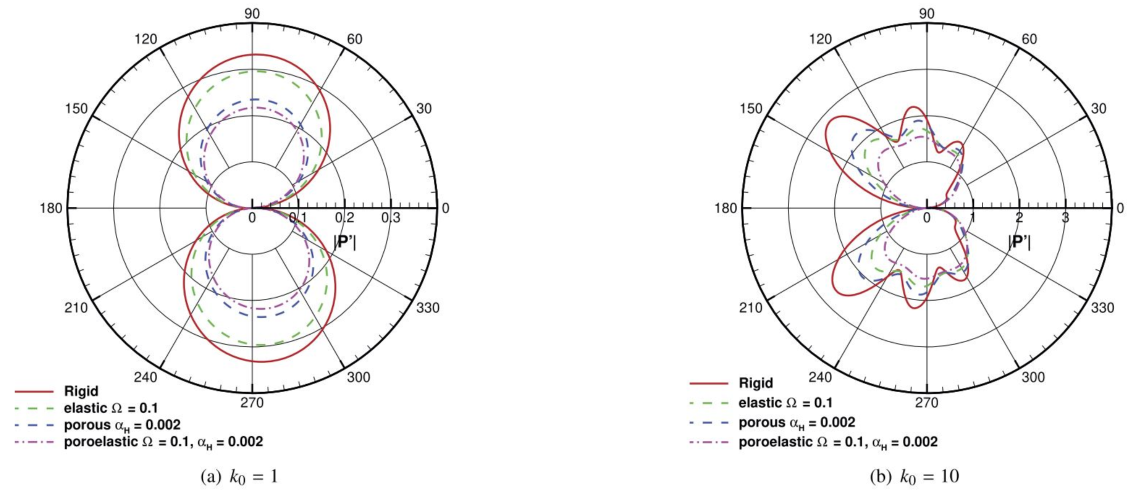

(c) Line quadrupole source.

Figure 2.35: Directivities for different plate configurations due to a point quadrupole source (a) & (b) and a line quadrupole source (c) placed at the trailing edge with a sweep angle of 0 degrees. Retrieved from Pimenta et al. [50].

Pimenta et al. [50] also looked at acoustic scattering of elastic plates by means of a computation. Pimenta et al. expended the analysis as well by including a poroelastic plate. However, as the kite should not be able to let air (or water) pass through its surface, as this would reduce the efficiency of the kite power system, the kite is considered to be non-porous. For the elastic plate, the vacuum bending wave Mach number (Ω) is set to be equal to $\Omega = 0.1$. The vacuum bending wave Mach number is given by $\Omega = \tilde{k}_0/\tilde{k}_B$, which is the acoustic wavenumber divided by the bending wavenumber. $\Omega = 0.1$ therefore means that the bending wavenumber of the plate is 10 times larger than the acoustic wavenumber. Pimenta et al. analyzed the noise scattering by a quadrupole source for low and high frequencies. A quadrupole source is representing turbulent flow behaviour, which is also expected to be the case for the soft kite.

In Figure 2.35 it can be seen that the directivity plots are of similar shape for both the rigid as the elastic plate. The elastic plate clearly shows a reduction in the noise compared to the rigid plate. For higher frequencies, the reduction of the noise for the elastic plate only holds for certain angles, mainly between 120° and 240°.

The total sound power level for the different plate configurations are shown for different wavenumbers for the case with the point quadrupole source in Figure 2.36. It can be seen that applying elasticity (as well as porosity) results in a reduction of the total sound power level compared to the rigid-impermeable square plate. For elasticity, this effect becomes more pronounced at higher wavenumbers.

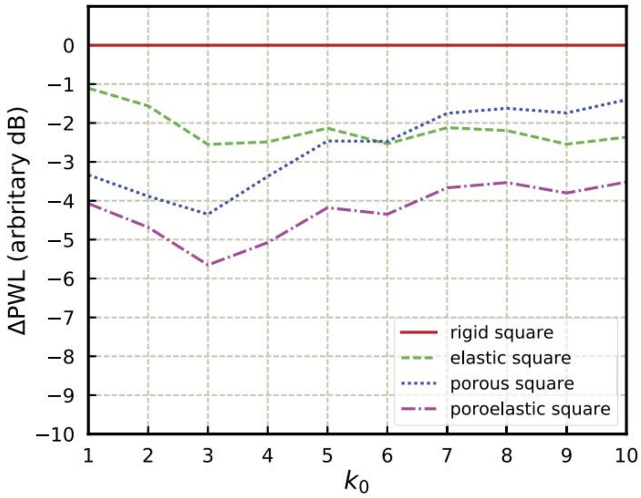

Figure 2.36: Sound power level differences for different plates. Obtained from Pimenta et al. [50].

As mentioned before, the elastic trailing edge results in an enhancement of the noise compared to the rigid trailing edge at the structural frequency and a reduction of the noise at the recirculation frequency. This statement is supported by Nilton et al. [51]. Nilton et al. investigated the effects of structural damping interaction of a turbulent eddy with flexible plates with respect to the aerodynamic noise generation. It was found that structural damping of the flexible structure results in a reduction of the scattered sound at the structural frequencies. In Figure 2.37, it can be seen that for the non-damped elastic plate, sharp peaks exist, which correspond to the structural frequency. At other frequencies, a reduction of the sound power can be seen.

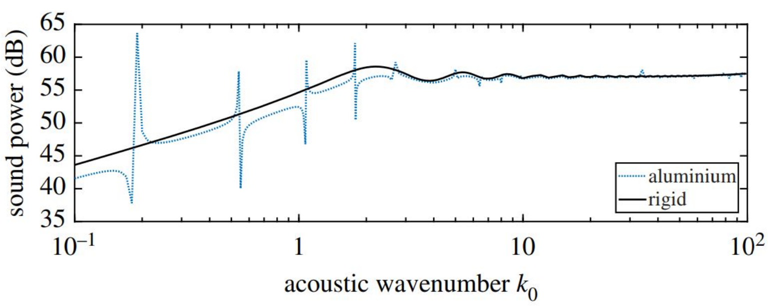

Figure 2.37: Sound power radiated by a rigid and non-damped elastic plates as a function of k_0. Obtained from Nilton et al. [51].

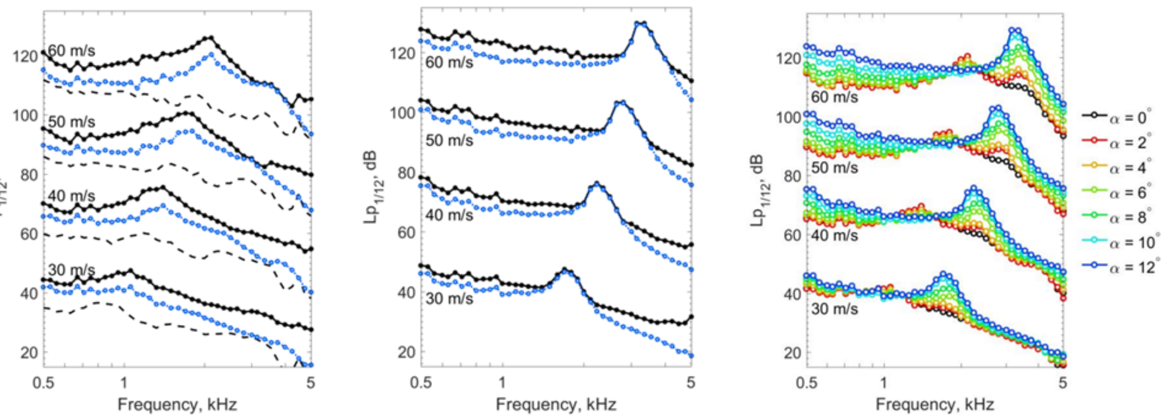

(a) $\alpha = 0°$ (b) $\alpha = 12°$ (c) $\alpha = 0° - 12°$

Figure 2.38: Integrated 1/12th octave band airfoil and tip noise spectra at $U_\infty = 30 - 60$m/s. For (a) and (b): The solid black line with filled circular markers is the airfoil spectrum, while the dotted blue line with open circular markers is the tip noise spectrum. The dashed black line is the background noise spectrum of the empty wind tunnel. Note that with each increase in flow speed, the spectra have been offset by 20 dB for clarity. Retrieved from Moreau and Doolan [41].

Recirculation Zone Induced Noise

Unlike conventional airfoils, the LEI kite has a recirculation zone on the pressure side of the airfoil. However, a recirculation zone is not completely unknown for a conventional wing, as this also appears for the case that a slat is implemented. The shear layer of the recirculation zone of the slat reattaches near the tip of the slat. The resulting vortices are then shed at the tip of the slat, which generates noise. Nevertheless, looking at the recirculation zone of the kite, the reattachment point is at a relatively large distance to the trailing edge, which means that the trailing edge scattering is unlikely to be directly influenced by the recirculation zone, although this depends on the velocity and angle of attack. However, what is influenced by the recirculation zone is the boundary layer on the pressure side of the kite.

Noise generated due to a recirculation zone is a phenomena that is not as extensively studied as for example noise due to vortex shedding. Moreover, no studies have yet been conducted on the recirculation zone of an LEI kite. Therefore, this literature review takes a closer look into the noise generated at the recirculation zone of a leading edge slat, also known as a high-lift device, as its geometry and airflow shows similar characteristics as that of the LEI kite airfoil. Just as the LEI kite airfoil, the slat has a cylindrical leading edge, sharp trailing edge and a recirculation zone.

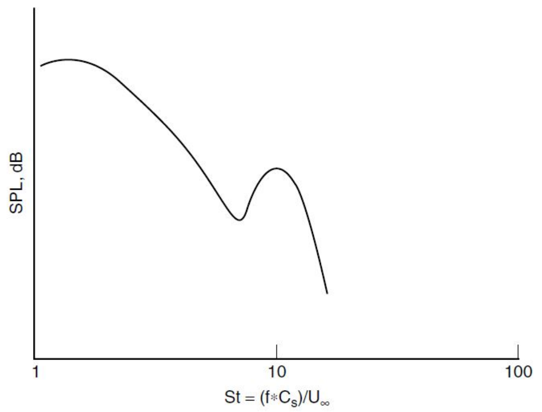

Figure 2.39: A generic slat acoustic spectrum based on Strouhal frequency. Obtained from Khorrami and Lockard [52].

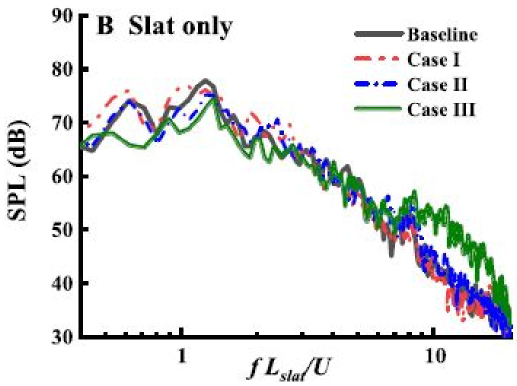

Figure 2.40: Sound pressure level at r=10C, θ=270 deg based on 1C chord length. Obtained from Chen et al. [53].

In the paper of Khorrami and Lockard [52], which takes a closer look into the aeroacoustics of a slat, the generic spectrum for landing conditions is visualized. The spectrum, as shown in Figure 2.39, is comprised of a low- to mid-frequency broadband component, followed by a high-frequency tonal component. This spectrum is based on Strouhal frequency, which in this case is defined as: $\mathrm{St} = \frac{f \cdot C_s}{U_\infty}$, with C_s being the slat chord, U_∞ the freestream velocity and f the frequency.

Another example of the acoustic spectrum of a slat is shown in Figure 2.40, which is obtained from the paper of Chen et al. [53]. The paper of Chen et al. researches a novel wall treatment method to improve the aeroacoustic and aerodynamic performance of high-lift devices. The baseline case is the case in which no wall treatment is applied, which is thus the case looked at for this literature review. From Figure 2.40, it can be seen that the maximum sound pressure level (SPL) is around 80 dB for a Strouhal number of 1, which is in agreement with the spectrum obtained from Khorrami and Lockard. The second peak is found at a Strouhal number of about 8 and has a SPL value of about 55 dB. Note that these SPL values are recorded at a distance of 10 times the chord length of the slat and at an angle of 270 degrees.

Translating this to the case of the LEI kite, it is expected to find the first peak around a frequency around 2.5 to 10.3 Hz and the second peak around a frequency of 20.5 to 82.1 Hz. Important to note is that the actual values can differ also due to the more slender configuration of the LEI kite compared to the slat.

2.3.6. KCU (*Kitepower*)

When in operation, the KCU is covered by a so-called "bullet". The interaction between the KCU bullet and the airflow, is considered comparable to the phenomenon of flow over a bluff body. When in flight, the bullet will face the direction of the airflow from two main positions and every angle in between, where the two main positions are facing "forward" and facing "sideways". A photo of the KCU within the bullet during flight is shown in Figure 2.41.

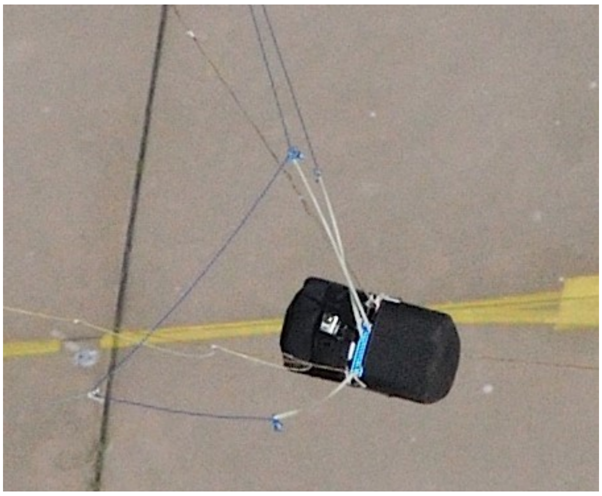

Figure 2.41: Kite control unit during flight. Photo by M. Dereta [54].

The bluff body interaction with the airflow will result in vortex shedding. Matsumoto [55] describes the various types of vortex generation and the related response characteristics of the bluff bodies. The considered 2D rectangular cylinder with a 0.5 side-ratio is taken as a simplified, yet comparable shape as the KCU bullet.

Matsumoto found that different types of vortices were found at different angles of the rectangular cylinder, which is displayed in Figure 2.42. For the range of angles $67° < \beta < 90°$, both Kármán vortex shedding as well as one-shear-layer-instability vortex generation could appear. For $7° < \beta < 67°$ only the Kármán vortex shedding exists, while for $0° < \beta < 7°$ again both Kármán vortex shedding as well as one-shear-layer-instability vortex generation could exist apparently or latently for some vortices. The obtained Strouhal numbers at the different angles of β are shown in Figure 2.43. From Figure 2.43, it can be seen that the largest Strouhal number appears around $\beta = 25°$, while the lowest Strouhal number occurs at $\beta = 90°$.

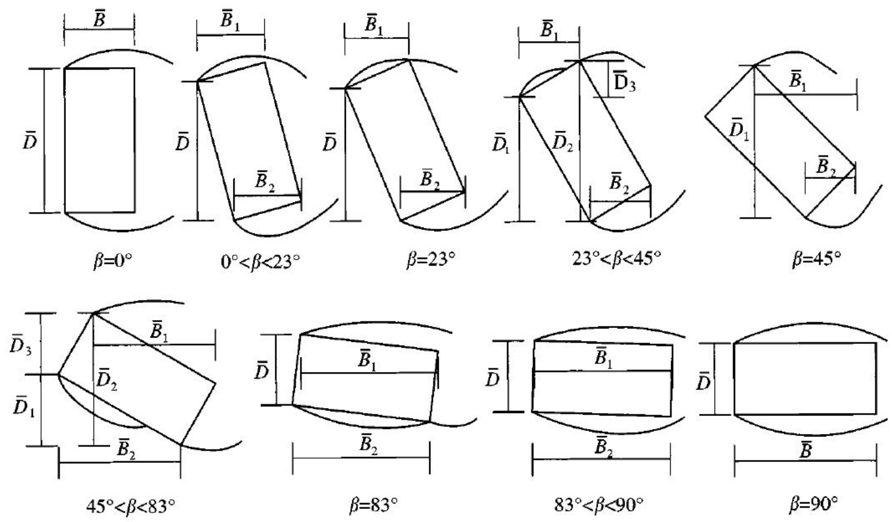

Figure 2.42: Illustration of flow separation depending on β for a 2-D rectangular cylinder with $B/D = 0.5$. Retrieved from Matsumoto [55].

Sarioglu [56] conducted a study on vortex shedding of rectangular cross-sections as well. Sarioglu conducted a wind tunnel experiment and made use of hot-film measurements in the wake of the models at Reynolds numbers in the range $1 \cdot 10^4 - 2 \cdot 10^5$. The obtained results for the rectangular shapes with $w/h = 0.5$ and $w/h = 2.0$ are shown in Figure 2.44.

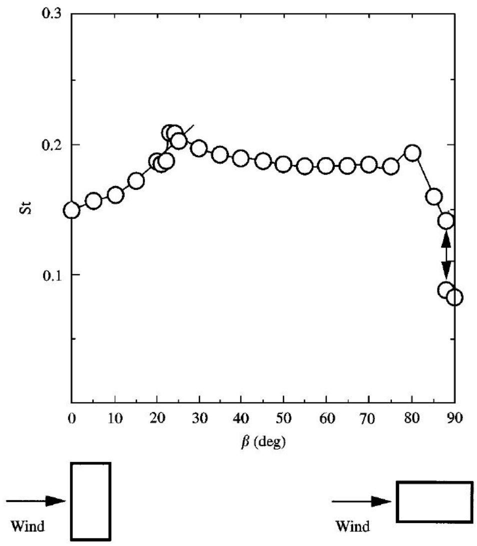

Figure 2.43: Stouhal number, St, versus the angle of attack β for a 2-D rectangular cylinder with $B/D = 0.5$. Retrieved from Matsumoto [55].

The dimensionless Strouhal number is obtained by making use of the equation $\mathrm{St} = \frac{f_s h}{U_\infty}$. The shedding frequency parameter is a non-dimensional frequency, which is given by $F = \frac{f_s h^2}{\nu}$. Sarioglu found that the Strouhal numbers decreased with increasing width-to-height ratios. Furthermore, it was observed that the angle of incidence only had very little to no effect on the Strouhal numbers for the rectangular shape with $w/h = 0.5$, while a more pronounced effect is seen for $w/h = 2.0$.

For the KCU bullet, with kite velocities ranging from 10 m/s to approximately 45 m/s in operation, the Reynolds number can be approximated. The kinematic viscosity is found by making use of the International Standard Atmosphere properties for an altitude of 250 m, which results in $\nu = 1.4897 \cdot 10^{-5}$ m^2/s [57]. The

Reynolds number is expected within a range of $3.98 \cdot 10^5 \leq \mathrm{Re} \leq 2.98 \cdot 10^6$. This then results in a Strouhal number around St = 0.198. Thus, the expected shedding frequency range is $3.3\ \mathrm{Hz} \leq f_s \leq 8.91\ \mathrm{Hz}$.

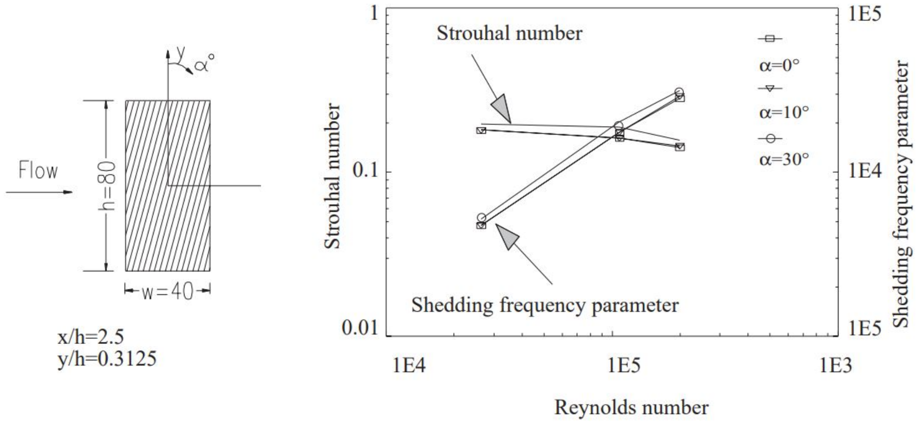

(a) Measured at $x/h = 2.5$, $y/h = 0.3125$ for $w/h = 0.5$.

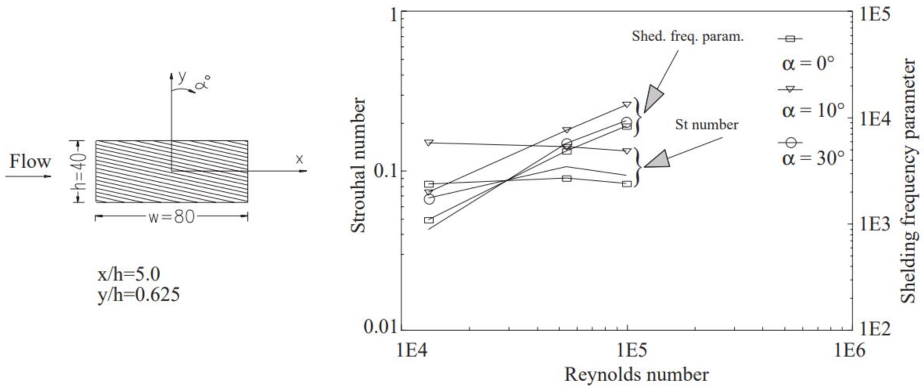

(b) Measured at $x/h = 5.0$, $y/h = 0.625$ for $w/h = 2.0$.

Figure 2.44: Strouhal number and shedding frequency parameter versus Reynolds number for a rectangular cylinder. Obtained from Sarioglu [56].

2.3.7. PROPELLERS

On the KCU of *Kitepower* a Ram Air Turbine (RAT) is attached. The RAT is required to provide power to the KCU, as the battery of the KCU itself cannot last for longer duration flights. The RAT has similar noise characteristics as that of a propeller, although the loading of the RAT remains limited. Due to the rapid rotation of the blades and the interaction with the airflow, the noise generated by these propellers outweigh the trailing edge noise in terms of dominance and audibility. Logically, this also applies to the propellers of the kite of the system of *Kitemill*, which are used for the VTOL. When considering propellers, two types of noise can be distinguished: tonal and broadband noise [58]. In the report of Marinus [59] both noise types and their characteristics are discussed as well, which will be summarized below.

TONAL NOISE

Due to the rotation of the propeller, periodic noise is generated. Two noise components can be found that occur periodically, namely the thickness noise and the loading noise. The thickness noise is caused by the displacement of the air flow by the volume of the propeller blades. The loading noise on the other hand is caused by the fact that the pressure field of the propeller blades, which generates lift and drag, is moving in a medium, in this case: air. The moving pressure field causes pressure fluctuations, which then generate loading noise [60]. Loading noise is significant at low and moderate speeds [61], which is why for the case of the RAT the thickness noise is expected to be dominant. As can be seen in Figure 2.45, the tonal peaks of a typical envelope of a propeller noise spectrum are located at the Blade Passing Frequency (BPF). The BPF is defined by $BPF = \frac{n \cdot rpm}{60}$, in which n equals the amount of propeller blades and rpm the rotations per minute of the propeller.

BROADBAND NOISE

Typically, broadband noise is induced by turbulence. When considering propeller noise, the contribution of broadband noise is often much smaller than the tonal noise components [60]. Broadband noise of the propeller is induced by an unsteady pressure field around the blades. This occurs when for instance, vortices are being shed from the tips and trailing edges of the propeller blades. [58]

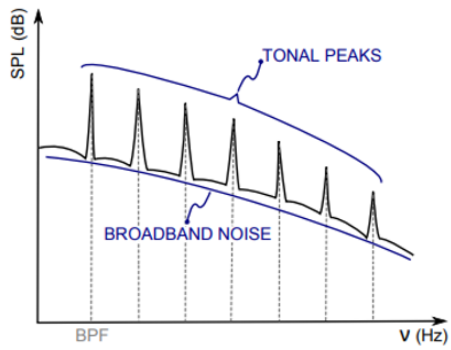

Figure 2.45: Typical envelope of a propeller noise spectrum. Obtained from Marinus [59].

2.4. SOUND PROPAGATION

When looking at AWES the ground effect is something one should be taking into account when assessing the noise from the system. The ground effect for sound refers to the influence of the ground on the propagation of sound waves. When sound waves propagate through air, they encounter different types of soils, including grass, gravel, sand, and concrete, which can affect the speed and direction of the waves.

One of the most significant factors that influences the ground effect for sound is the physical properties of the soil. For example, soft and loose soils like sand or loam tend to absorb more sound energy than hard surfaces like concrete or asphalt, which can cause a decrease in sound level as the sound waves propagate through the soil. Grass on the other hand, can have a mixed effect on sound propagation, depending on the height, density, and moisture content of the vegetation. [62]

3
METHODOLOGY

3.1. ANALYTICAL METHODS

In this section, two common analytical methods for acoustic simulations will be discussed: the Amiet model and the Brooks-Pope-Marcolini (BPM) model. The Amiet model is a semi-empirical model that is used for the prediction of the sound radiation from turbulent flows. The BPM model, on the other hand, is a computational aeroacoustic model that is used to predict sound propagation for different airfoil self-noise mechanisms. Both the BPM model and the Amiet model require boundary layer parameters as inputs. Therefore, also the boundary layer parameters that are required for the models are discussed in this section. To better visualize the analytical model, a scheme is set up in Figure 3.1. The scheme illustrates the relationship between the boundary layer parameters, the Amiet model, the BPM model, and the resulting directivity plot and SPL spectrum.

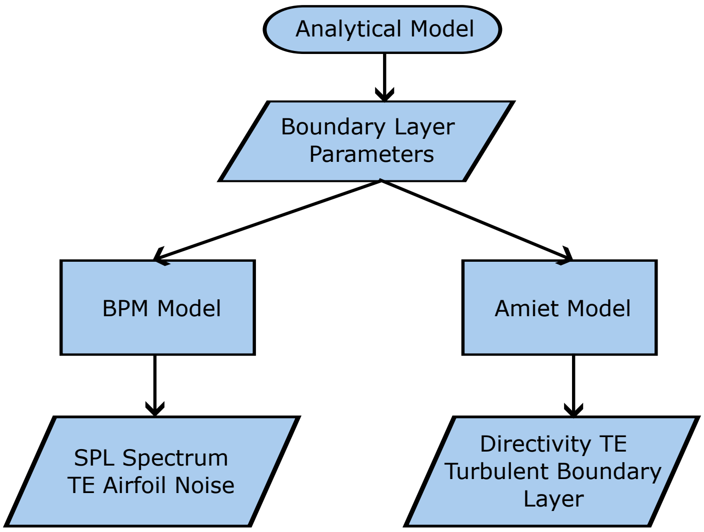

Figure 3.1: Scheme of the analytical model.

In addition to these analytical models, an estimation of the peak sound pressure level (SPL) of the tether vortex shedding noise is also used. This is an important noise source that can occur due to the flow around the tether of the airborne wind energy system. The calculation of this noise source is based on an equation that takes into account the velocity and the diameter of the tether among other parameters. This formula will be discussed towards the end of this section.

3.1.1. AMIET MODEL

Amiet [63] has its formulation for trailing edge noise based on the diffraction theory applied to a flat plate and thereby ignores the shape of the airfoil. The model consists of a turbulent flow that is convecting past a trailing edge. Additionally, Amiet [64] was the first to consider the finite-chord effects for the leading-edge noise mechanism. In order to do so, Amiet made use of two semi-infinite Scharzschild solutions, which were based on the velocity potential for this noise mechanism. Now, for the trailing edge noise, Roger and Moreau [65] made use of this same principle, which is shown in Figure 3.2. This correction made to the Amiet model by Roger and Moreau [65] is known as the first backscattering correction.

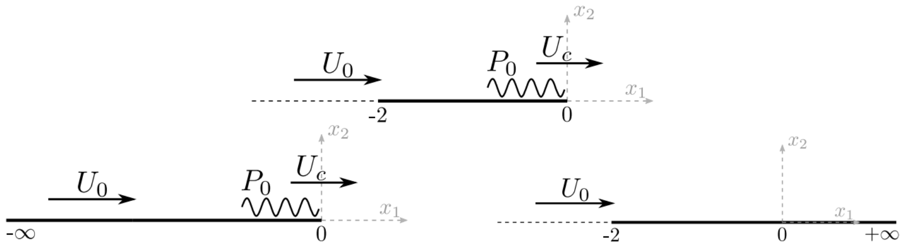

Figure 3.2: Roger and Moreau trailing-edge noise model. The top figure represents an incident gust on a finite-chord airfoil, the bottom left figure represents the main scattering half-plane problem with the bottom right representing the leading-edge correction. Note that all coordinates are made non-dimensional by the half chord with the reference being at the trailing edge. Obtained from Lee et al. [39].

The formulation of the noise power spectral density is given in the report of Casalino and Barbarino [66]. This equation includes the wall pressure frequency spectrum. For the wall pressure frequency spectrum different definitions exist, which are essentially all improvements of the previous definition. The latest improvement is done by Lee [67], who presents a new empirical model, which has been validated against measurement data. The formulation of this new model of the wall pressure frequency spectrum is given by:

$$\frac{\Phi_{pp}(\omega)U_e}{\tau_w^2\delta^*} = \frac{\max(a,(0.25\beta_c-0.52)a)(\omega\delta^*/U_e)^2}{[4.76(\omega\delta^*/U_e)^{0.75}+d^*]^e+[8.8R_T^{-0.57}(\omega\delta^*/U_e)]^{h^*}}, \tag{3.1}$$

with $\beta_c = (\theta/\tau_w)(dp/dx)$, $a = 2.82\Delta^2(6.13\Delta^{-0.75}+d)^e[4.2(\Pi/\Delta)+1]$, $\Delta = \delta/\delta^*$, $\Pi = 0.8(\beta_c+0.5)^{0.75}$, $R_T = (\delta/U_e)(\nu/u_\tau^2)$, $d = 4.76(1.4/\Delta)^{0.75}[0.375e-1]$, $e = 3.7+1.5\beta_c$ and $h^* = \min(3,(0.139+3.1043\beta_c))$.

Furthermore, the noise spectral density formulation includes a non-dimensional constant ($\mathscr{C}$), which is related to the spanwise correlation length. This constant is defined as a calibration constant and often referred to as Corcos' constant. In literature Corcos' constant often varies between 0.2 and 0.9, as also shown in Table 3.1. An appropriate value of Corcos' constant is obtained through comparing the Reynolds number and airfoil shape to the values stated in Table 3.1, which can thus differ per type of AWE system and operation.

#	Airfoil/Reference	U_0 [m/s]	Chord Length [cm]	$\mathscr{C}$
1	Flat Plate/Corcos [68]	69	any	0.714
2	Flate Plate/Amiet [69]	102	any	0.476
3	NACA0012/Brooks and Hodgson [70]	38.6	61	0.62
4	NACA0012/Brooks and Hodgson [70]	69.5	61	0.58
5	NACA0012/Garcia and Gérard [71]	60	50	0.9
6	Airbus A320/Pérennès and Roger [72]	80	30	0.28
7	Valeo CD/Moreau and Roger [73]	16	13.6	0.83
8	Valeo CD/Moreau and Roger [73]	30	13.6	0.83
9	NACA5510/Rozenberg and Moreau [74]	70	20	0.68
10	NACA0012/Stalnov et al. [75]	20	20	0.71
11	NACA0012/Stalnov et al. [75]	40	20	0.71
12	NACA0012/Stalnov et al. [75]	60	20	0.71

Table 3.1: Comparison of different airfoils for different conditions and their respective Corcos' constant.

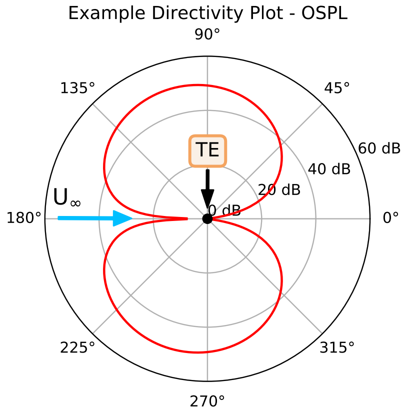

Figure 3.3: Example of a dipole Amiet directivity plot.

The Amiet directivity plot provides valuable information about the sound radiation pattern of an airfoil. Understanding how to interpret the plot correctly is crucial for analyzing the directivity characteristics. In the plot, the center of the polar plot represents the trailing edge of the airfoil, which is also indicated in Figure 3.3. The direction of the freestream velocity, or the incident airfoil, is indicated by an arrow in that same plot, which is coming from the left-hand side of the plot. The polar plot represents the sound radiation pattern in different angular directions relative to this reference point. The radial distance from the center of the plot indicates the sound pressure level in decibels emitted in each direction for a certain distance from the reference point. It's important to note that the directivity plot provides information about the relative contributions of different angles to the overall sound radiation, rather than absolute sound levels or frequencies.

3.1.2. BPM MODEL

Brooks, Pope and Marcolini have written a report [37] describing a method of a model for trailing edge noise, also referred to as the BPM model. The BPM model can not only predict turbulent boundary layer trailing edge noise, but vortex shedding noise from laminar boundary layer instability and from a blunt trailing edge, separation-stall noise and tip noise as well. The spectral scalings of these airfoil self-noise mechanisms are the foundation for the BPM model. Furthermore, by making use of an anechoic wind tunnel, exhaustive experimental data has been acquired and used to tune the model.

In this subsection, each of the noise sources related to AWE systems and their BPM prediction are discussed. Combining all noise sources will lead to a full prediction of the trailing edge noise based on the BPM model.

TURBULENT BOUNDARY LAYER TRAILING EDGE NOISE

The model distinguishes three contributions for the overall model for turbulent boundary layer trailing edge noise: the suction side boundary layer (SPL_s), the pressure side boundary layer (SPL_p) and the effect of the angle of attack (SPL_α). The spectral power of the three contributions are formulated as:

$$SPL_s = 10\log\left(\frac{\delta_s^* M^5 L \overline{D}_h}{r^2}\right) + A\left(\frac{\mathrm{St}_s}{\mathrm{St}_1}\right) + (K_1 - 3) + \Delta K_1 \tag{3.2}$$

$$SPL_p = 10\log\left(\frac{\delta_p^* M^5 L \overline{D}_h}{r^2}\right) + A\left(\frac{\mathrm{St}_p}{\mathrm{St}_1}\right) + (K_1 - 3) \tag{3.3}$$

$$SPL_\alpha = 10\log\left(\frac{\delta_s^* M^5 L \overline{D}_l}{r^2}\right) + B\left(\frac{\mathrm{St}_p}{\mathrm{St}_2}\right) + K_2 \tag{3.4}$$

$$\tag{3.5}$$

with δ^* being the boundary layer displacement thickness on both sides of the airfoil, St the Strouhal number based on δ^* and A, B, K_1, K_2 and ΔK_1 empirical functions based on the Strouhal number.

Combining these three contributions then leads to the total spectral power of the TBL-TE noise to be defined as:

$$SPL_{TBL-TE} = 10\log\left(10^{\frac{SPL_p}{10}} + 10^{\frac{SPL_s}{10}} + 10^{\frac{SPL_\alpha}{10}}\right). \tag{3.6}$$

LAMINAR BOUNDARY LAYER VORTEX SHEDDING NOISE

Besides turbulent boundary layers, also laminar boundary layers can be a source of airfoil self-noise. For laminar boundary layers, the noise is generated by a feedback loop between shed vortices at the trailing edge and instability waves in the boundary layer. The shedding of these vortices creates fluctuations in the pressure and velocity of the air, which propagate as sound waves, which leads to noise. This noise is typically distributed on a narrow band of frequencies. The equation given by the BPM model to estimate this noise spectrum is:

$$SPL_{LBL-VS} = 10\log\left(\frac{\delta_p M^5 d\overline{D}_h}{r_e^2}\right) + G_1\left(\frac{\mathrm{St}'}{\mathrm{St}'_{peak}}\right) + G_2\left[\frac{\mathrm{Re}_c}{(\mathrm{Re}_c)_0}\right] + G_3(\alpha_*), \tag{3.7}$$

with G_1, G_2 and G_3 representing empirical functions.

BLUNTNESS TRAILING EDGE VORTEX SHEDDING NOISE

Bluntness trailing edge vortex shedding noise is characterized by the height of the trailing edge, which can, when large enough in relation to the boundary layer thickness, result in vortex shedding. This noise is typically of tonal nature and the frequency and amplitude of this noise source depends on the geometry of the trailing edge. By making use of the average displacement thickness of both sides of the airfoil (δ^*_{avg}), the height of the trailing edge (h) and the angle between the suction and pressure sides of the airfoil (Ψ), the bluntness trailing edge vortex shedding noise is estimated:

$$SPL_{BLT-VS} = 10\log\left(\frac{\delta_p^* M^{5.5} h\overline{D}_h}{r_e^2}\right) + G_4\left(\frac{h}{\delta^*_{avg}}, \Psi\right) + G_5\left(\frac{h}{\delta^*_{avg}}, \Psi, \frac{\mathrm{St}''}{\mathrm{St}''_{peak}}\right). \tag{3.8}$$

Again, this equation makes use of empirical functions given by G_4 and G_5.

TIP VORTEX FORMATION NOISE

Tip vortex formation noise is a phenomenon that occurs when air flows over a sharp edge, such as the tip of a wing. As the air flows over the sharp edge, it creates a swirling vortex of fluid at the tip, which is known as the tip vortex. The formation of these vortices can create significant noise, particularly at higher velocities. Tip vortex formation noise is predicted as follows:

$$SPL_{TIP} = 10\log\left(\frac{M^2 M_{\max}^3 l^2 \overline{D}_h}{r_e^2}\right) - 30.5(\log(\mathrm{St}'') + 0.3)^2 + 126. \tag{3.9}$$

In this case, the Strouhal number is found by making use of the spanwise extent at the trailing edge of the viscous core of the tip vortex, which is given by l in Figure 3.4.

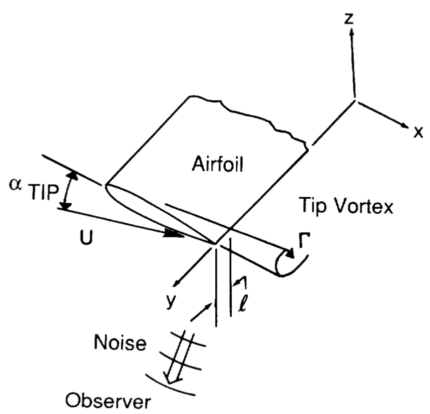

Figure 3.4: Formation of tip vortex. Obtain from Brooks et al. [37]

3.1.3. Boundary Layer Parameters

As described in the previous subsections, airfoil self-noise caused by the trailing edge of the airfoil can be predicted by making use of boundary layer parameters as an input. These parameters can be obtained through XFOIL [76] or a CFD simulation, but also by making use of the flat-plate boundary layer theory is an option. Appendix B discusses these parameters and gives a formulation of these parameters for both laminar and turbulent flow, as given by the flat-plate boundary layer theory.

The flat-plate boundary layer theory provides a well-established framework for estimating the boundary layer parameters. However, it is important to note that the theory is limited to flow over a flat surface, and thus may not accurately describe the behavior of flow over complex geometries such as airfoils with varying thickness and camber. Nonetheless, the flat-plate boundary layer theory remains a useful tool in predicting the behavior of the boundary layer in a variety of scenarios, including those found in airborne wind energy applications. The ease of use and computational efficiency make these formulations a valuable tool to analyze the effects of different boundary layer parameters and could provide rough, but reasonable estimates. [77]

3.1.4. Validation

Amiet Model

In order to validate the Amiet model used in this report, the paper of Teruna et al. [78] is used. This paper discusses the far-field noise spectra and far-field noise directivity patterns for a NACA0018 airfoil with a solid trailing edge and a porous trailing edge. For this report, the focus is solely on the results of the airfoil with the solid trailing edge. The paper analyzes two freestream velocities, 20 m/s and 40 m/s, which are installed at an AoA of 0° and 7.8°, where the case of 40 m/s is only analyzed at an AoA of 7.8°. On both sides of the airfoil, the boundary layer is forced to transition by spanwise zigzag strips that were installed at 20% of the chord length from the leading edge. For each of these cases, the boundary layer parameters are obtained through XFOIL [76] and given in Table C.1. Moreover, the NACA0018 airfoil has a chord length of 20 cm and a span of 8 cm.

The boundary layer parameters as presented in Table C.1 are used in the analytical noise model. The obtained values are then compared to the results from the paper of Teruna et al. [78] that contains only the trailing edge noise of the airfoil observed from location $x/c = -0.68, y/c = 4.95$. Looking at the sound pressure level spectra that are obtained from the analytical model and presented in Figure C.1, it can be seen that the analytical model and the results of the paper generally align relatively well. For the first case, shown in Figure C.1a, the difference between the model and the paper is around 3 dB with a maximum of 6 dB. The second case, shown in Figure C.1b, shows a difference around 2 dB with a maximum of 6 dB. And the third case, shown in Figure C.1c, has a difference of approximately 3 dB with a maximum of 5 dB. Moreover, it can be found that the model differs more from the paper data at lower Strouhal numbers than at higher Strouhal numbers.

Besides validating the Amiet model for a single observer point, the model is also compared against the data obtained from the paper for the full directivity, which is shown in Figure C.2. Again, the same three cases are used as given in Table C.1. The directivity plots are shown for three ranges of Strouhal numbers, St=[4,8], St=[8,16] and St=[16,32]. The directions for which the model and paper differ most is from 300° to 360°, while the directivity ranging from 0° to 300° shows minimal differences. It can thus be stated, that the model predicts the directivity with relatively minor error.

BPM Model

The validation of the BPM model is divided into its four different contributors: turbulent boundary layer trailing edge noise, laminar boundary layer vortex shedding noise, bluntness trailing edge vortex shedding noise and tip vortex formation noise. In order to validate these parts, the model is compared to the data obtained from the original report of Brooks, Pope and Marcolini [37]. The obtained data applies to a NACA0012 airfoil with a span of 45.72 cm, which is equal throughout this whole section. Other parameters, however, are varying and are therefore mentioned in the corresponding part. The report [37] also includes equations on how to obtain the boundary layer parameters for the different conditions, such as the tripped and untripped boundary layer. These formulations will be used for the validation of the components of the model.

The retarded source to observer distance is equal to 1.22 m with the retarded source to observer angle measured from downstream being 90 degrees, as well as the lateral directivity angle.

Turbulent Boundary Layer Trailing Edge Noise

From Figure C.3e and Figure C.3f it can be seen that the model slightly underestimates the spectrum at the lower frequencies and slightly overestimates the spectrum at the higher frequencies for the cases with large angles of attack. Nonetheless, besides these slight deviations, the model shows great agreement with the experimental data.

Besides the comparison of the model to the results produced in the BPM report, the model is checked for its response to an increase of the distance from the source to the observer. This is done by using different distances as an input for the conditions where the NACA0012 airfoil is exposed to a velocity of 31.7 m/s at an angle of attack of 0 degrees. The input distances increase from 1.22 m to 200 m. The results can be observed in Figure C.4, which shows that the model behaves as expected for increasing distances.

Laminar Boundary Layer Vortex Shedding Noise

The comparison between the data from the BPM report [37] and the prediction model can be found in Figure C.5. From Figure C.5a, Figure C.5b, Figure C.5c and Figure C.5d, it can be seen that the prediction model slightly overestimates the values at the left-hand side of the peak. However, for all cases, lower and higher angles of attack, applies that the peaks are accurately estimated.

Bluntness Trailing Edge Vortex Shedding Noise

Now, looking at the results of the comparison between the model and the experimental values in Figure C.6, it can be seen that the model shows some overestimation for the lower frequency range for the smallest trailing edge height, but besides that closely matches the experimental values.

Tip Vortex Formation Noise

The comparison in Figure C.7 shows consistency with the prediction made in the report. In the report [37], a comparison is made between the prediction that includes the tip noise and the noise data obtained in another report written by Brooks and Marcolini [79]. This comparison shows that the prediction creates a slight overprediction at higher frequencies, for the particular case that is used in this example. Nonetheless, the comparison shows consistency and compatibility with the data.

3.1.5. SENSITIVITY ANALYSIS

In order to investigate the sensitivity of the analytical models to boundary layer inputs, a sensitivity analysis was performed. The analysis aimed to identify the influence of different boundary parameters on the performance of the models. The focus is on the impact of the boundary layer thickness for the suction and pressure side and mean wind speed on the sound pressure level and directivity for both turbulent and laminar cases. The results of this sensitivity analysis will provide insight into the relative importance of these parameters.

The results of this sensitivity analysis are presented in section D.3. When examining the cases for the laminar boundary layer, it becomes apparent that the laminar boundary layer vortex shedding produces a peak in the total SPL output. This peak shifts to higher frequencies as the freestream velocity increases. Additionally, as the velocity increases, it can be observed that the turbulent boundary layer noise becomes more dominant. Simultaneously, the tip noise and blunt trailing edge vortex shedding have increased SPL values for an increase in velocity, although the turbulent trailing edge noise remains to be the main source for the broadband noise. For the turbulent cases, one of the key findings is that the tonal laminar vortex shedding contribution remains at much lower frequencies as compared to the laminar cases. Finally, comparing the results for the turbulent boundary layer cases with one side of the airfoil having an increased boundary layer thickness, it can be seen that increasing the boundary layer thickness on the pressure side results in a "flattening" of the tonal contribution of the laminar boundary layer vortex shedding. Another relevant observation, is that the contribution of the turbulent boundary layer in the model is especially sensitive to changes in velocity rather than boundary layer thickness.

The results of the Amiet model sensitivity analysis are shown in section D.2. For the first part of this analysis, the influence of the Reynolds number is looked at. It can be seen that for all frequencies an increase in

Reynolds number results in an increase in the overall sound pressure level (OSPL) values as well, while the shape of the directivity remains equal. The difference between the cases increases for higher frequencies, where the frequency peak for the lowest Reynolds number appears to be at much lower frequencies than for the higher Reynolds numbers. For the varying angles of attack, the results show the opposite occurring, namely larger angles of attack have a lower frequency peak than the lower angles of attack. Again, the directivity plots for the different frequency ranges remain broadly the same with the difference being in the value of the OSPL. Finally, the tripped boundary layer shows clear increased OSPL values for all frequency ranges, except for the highest frequency range (2500 Hz - 5000 Hz), where both cases show nearly equal values. All cases show dipole directivity patterns that are near perfect dipoles for the lower frequencies and show some more deviations towards the higher frequency ranges.

3.1.6. TETHER VORTEX SHEDDING PREDICTION MODEL

Obtaining the Strouhal number of the vortex shedding of a tether has already been described in Subsection 2.3.3 by the equation $\mathrm{St} = 0.198(1 - \frac{19.7}{\mathrm{Re}_d})$. However, this does not include an estimation of the sound pressure level generated by this vortex shedding. Obtaining an estimation of this value can be done by making use of the equation for the mean-square pressure due to vortex shedding by Fujita [80]:

$$\overline{p^2(r)} = \frac{\rho_0^2 U_\infty^6 \mathrm{St}^2 C_{L,\mathrm{rms}}^2 L l_c}{16 c_0^2 r^2}, \tag{3.10}$$

with L the span length of the cylinder, in this case the tether, l_c the spanwise correlation length, $C_{L,\mathrm{rms}}$ the root mean square (rms) of the lift coefficient and r the distance from the source to the observer.

In order to obtain the values for the rms lift coefficient and the spanwise correlation length, the suggestions of the empirical functions for the Reynolds number dependence of the report on fluctuating lift on a circular cylinder by Norberg [81]. This report provides the values for different Reynolds number ranges of which the total range is from $\mathrm{Re} = 47$ to $\mathrm{Re} = 3.0 \times 10^5$.

It should be noted the the Fujita equation assumes that the cylinder is rigid, and that the sound generated by the vortex shedding is not affected by any reflective surfaces in the environment. Additionally, by making use of this equation, it is assumed that the flow velocity is constant along the length of the tether, which is likely to not be the case, as the tether moves faster closer to the kite than at the winch.

After obtaining the peak sound pressure level from the vortex shedding by making use of the Fujita equation, an estimate of the rest of the spectrum is needed. For this, a Gaussian distribution is used. This distribution is described by its mean, which determines the location of the peak, and its standard deviation, which determines the width of the distribution. In this study, the standard deviation of the Gaussian distribution was empirically determined by fitting the distribution to the measured noise data from the report of Iglesias et al. [82], which describes an experimental study of the aerodynamic noise radiated by cylinders in different conditions. The formulation then looks as follows:

$$L_p(f) = A \cdot \exp\left(\frac{-(f - f_{vs})^2}{2 \cdot \sigma^2}\right) + B, \tag{3.11}$$

where A is the amplitude of the vortex shedding peak, f_{vs} the peak frequency of the vortex shedding, σ the standard deviation and B an additional constant that can be used to adjust the graph to the proper peak shape.

The validation of the estimation, which is fitted by making use of the experimental data of Iglesias et al. [82], can be found in Figure 3.5. The validation is carried out for two cases, for which one has a freestream velocity of 31.5 m/s and the other 50 m/s.

It's important to note that the estimation of the vortex shedding noise using the Fujita equation and the Gaussian distribution only provides an estimation of the peak of the vortex shedding. However, the actual noise spectrum measured in the experimental data may include additional sources of noise, such as background noise or other turbulence-induced noise. Therefore, while the peak sound pressure level as presented by the estimation may match well with the peak observed in the experimental data, as also shown in Figure 3.5, the overall noise spectrum may not match as closely or at all.

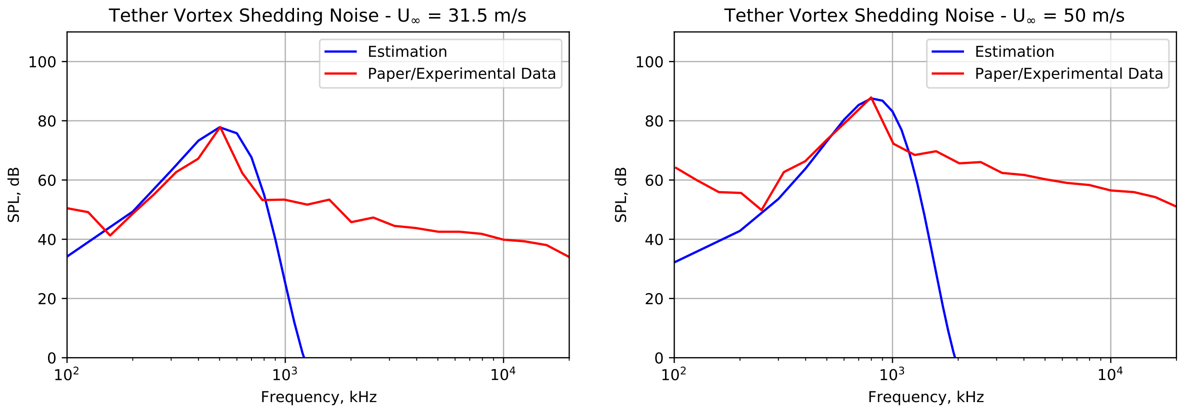

(a) U_∞=31.5 m/s

(b) U_∞=50 m/s

Figure 3.5: Validation of the estimation of the vortex shedding versus the experimental data obtained by Latorre Iglesias et al. [82].

3.2. EXPERIMENTAL METHODS

The experimental methods used to investigate the acoustic properties of the airborne wind energy system involve measurements in the field and processing and analyzing the obtained audio recordings. Due to the nature of the systems being studied, all measurements were conducted in the field. This section is divided into two parts: the test setup and the acoustic measurement system. The test setup describes the locations of the measurements and the distances between the microphone and the systems. The acoustic measurement system details the equipment used to collect the data, as well as the signal processing techniques.

3.2.1. TEST SETUP

The test setup consisted of two outdoor locations at which the airborne wind energy systems were operating to perform test flights. One of the locations being an airport (*Kitemill*) and the other being farmland in (*Kitepower*). The soil at the airport at the flight zone of the kite consists of organic soil in combination with water, plants, grasses and sediments, such as clay and some soil containing solely grass. The farmland, on the other hand, consists of a loam soil with grass. Although not directly included in the analysis, it is important to keep in mind that the propagation of sound waves does have a potential impact on the perceived sound. To measure the sound generated by the kite, a microphone was placed at a distance of approximately 600 to 700 meters downwind from the winch. This resulted in a radius of 300 to 600 meters from the kite's location in operation. The test setup is illustrated in Figure 3.6, showing the downwind location of the microphone and the simplified visualization of the airborne wind energy system. Details about the microphone that is used for this test setup are discussed in Subsection 3.2.2.

The location of the microphone was obtained via a GPS device to mark both the location of the microphone as the location of the winch. Additionally, the microphone was placed on a tripod, having the microphone at a height of about 1 meter above the ground.

The kite was flying several loops during the test flight, and the microphone was positioned towards the kite to capture sound data during the flight. The test was conducted during a single day, due to limits in the equipment and wind conditions. This limits the test to a single range of wind conditions and flight scenarios at each test site.

As one test was performed with *Kitemill* and one with *Kitepower*, two types of kites are used for these test: a fixed-wing kite (*Kitemill* KM1) and a soft, leading edge inflatable kite (*Kitepower* V9.60). Additionally, the flight pattern of both systems are different, as *Kitemill* flies a circular pattern and *Kitepower* flies figures of eight. Both systems, however, do work with a fixed ground station.

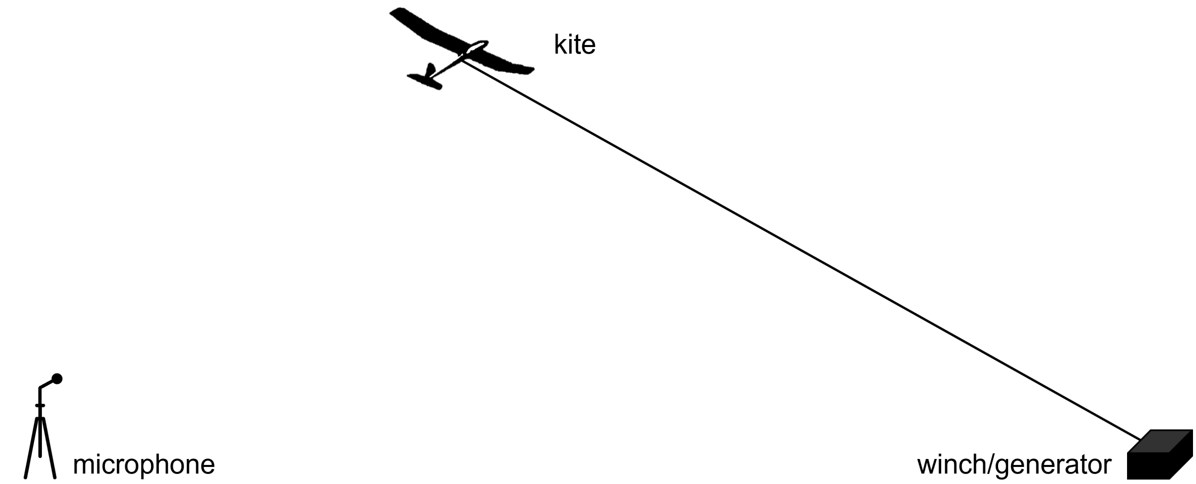

Figure 3.6: Test setup of the acoustic measurements of an airborne wind energy system.

KITEMILL

The test site of *Kitemill* is located at Lista, Norway. The audio recording is obtained during the flight test on March 27 2023. On March 27 2023, the wind was coming from the North West (↘), 308° to be more specific, which means the flight direction was South East. The microphone was placed downwind at a distance of 679 meters away from the winch of the kite. The flight zone of the kite, the winch and the location of the microphone are shown in Figure 3.7.

Figure 3.7: Overview of the measurement setup at *Kitemill* with the flight zone indicated in the yellow area. The GPS location of the winch was 58.099656°, 6.641725°.

The total flight time for this test was 11 minutes and 45 seconds, during which the kite completed 41 loops. The flight, as well as the recording, can be divided into three phases: takeoff, production and return. Although it should be noted that the last phase was not completed properly and shall therefore be referred to as return rather than landing.

(a) Takeoff of the KM1 kite.

(b) Positioning of the microphone.

Figure 3.8: Photos captured during the flight test of *Kitemill*.

The wind speed is obtained from a weather station located at Lista Fyr and was measured to be 9.1 m/s at the time of the flight. During the production phase of the flight, which starts 2 minutes and 24 seconds after the takeoff, the airspeed varied between around 30 m/s to 45 m/s. While flying its loops, the kite flew at heights between 130 m and 230 m. The tether, to which the kite was attached during the flight, had a decreasing length during the flight. The tether length started around 335 m for the start of the production phase and goes down to around 315 m. More detailed information on this data can be retrieved from Figure 3.9.

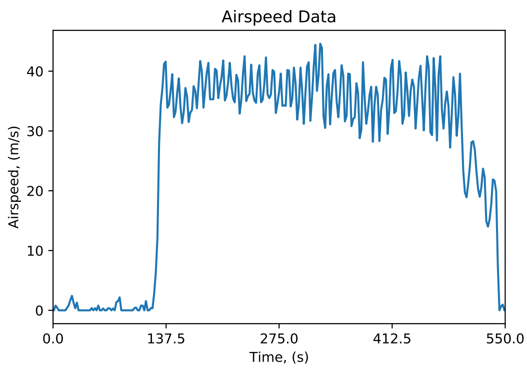

(a) Airspeed of kite

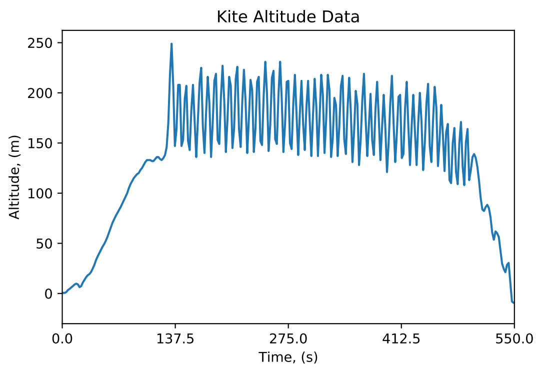

(b) Altitude of kite

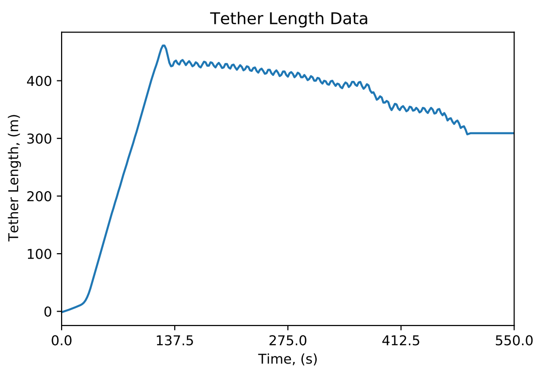

(c) Tether length

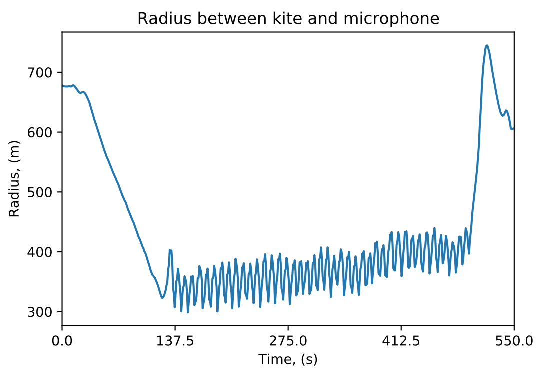

(d) Radius between the kite and the microphone

Figure 3.9: Data of the test flight of *Kitemill* on March 27, 2023.

KITEPOWER

The audio recording for this study for the system of *Kitepower* was obtained at the test site located in Dirksland, The Netherlands on May 12 2023. On this day, the wind direction was North East (↙), resulting in the flight direction of the kite being South West. The microphone was placed downwind at a distance of 650 meters from the winch of the system. The flight zone of the kite, the winch and the location of the microphone are shown Figure 3.10.

Figure 3.10: Overview of the measurement setup at *Kitepower* with the flight zone indicated in the yellow area. The GPS location of the winch was 51.76862°, 4.1189°.

An important note is that during the flight test, the propeller of the KCU was tied down, such that it was unable to move during the flight. This prevented the propeller from making excessive noise from (free)spinning. For the actual operating conditions of the propeller, *Kitepower* is able to set the propeller to be spinning at a chosen rpm. Additionally, two cameras were attached to the kite to record the kite from up close during the flight. One camera was facing the trailing edge of the kite, while the other showed the kite from the position of the KCU.

Figure 3.11: Photo captured during the flight test of *Kitepower*. The microphone is in the bottom left and the kite is at the upper right of the photo.

The total flight time for this test was 17 minutes and 44 seconds. During this period the kite flew a total of 17 full figure-eight patterns. For the analysis, only the production phase, meaning the traction phase is looked at. At the moment of flight, the wind was rather gusty, but the mean wind, as recorded by the weather station of Rotterdam The Hague Airport, was about 6 m/s at the moment of the flight. The measured wind velocity by *Kitepower* during the flight was between 4 m/s and 10 m/s.

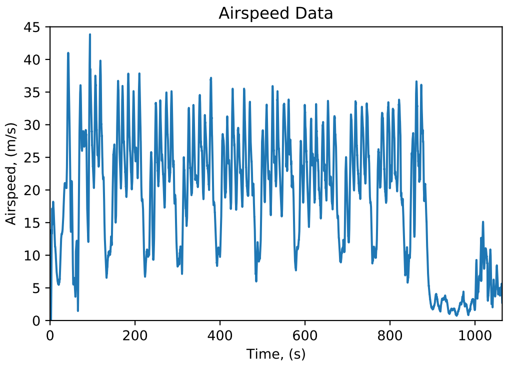

(a) Airspeed of kite

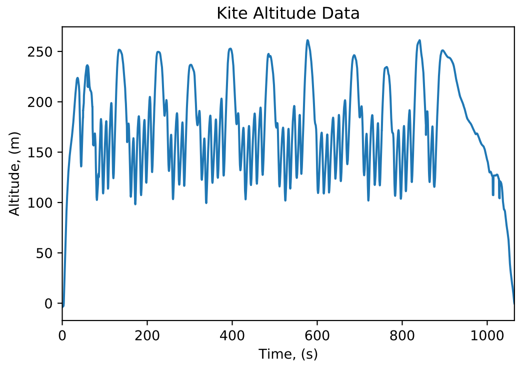

(b) Altitude of kite

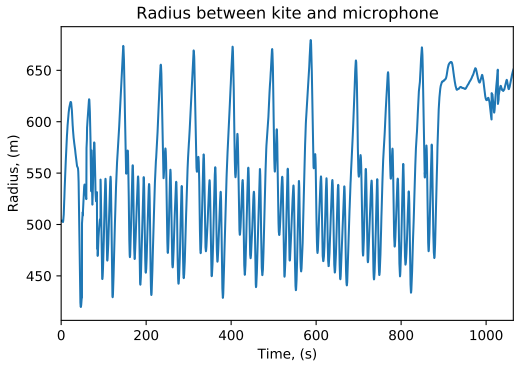

(c) Radius between the kite and the microphone

Figure 3.12: Data of the test flight of *Kitepower* on May 12, 2023.

While flying the figure-of-eight pattern, the altitude of the kite varied between 100 m and 250 m with an airspeed between 20 m/s and 40 m/s. The kite velocity, kite altitude and the radius between the kite and microphone during the test flight on May 12 2023 are given in Figure 3.12.

3.2.2. ACOUSTIC MEASUREMENT SYSTEM

The acoustic measurement system is a key component of this study, as it provides the means to measure and analyze the acoustic signals generated by the airborne wind energy system. This section describes the instrumentation and techniques used to measure and analyze the acoustic signals in this study.

The sound pressure level (SPL), denoted by L_p, is a commonly used measure of acoustic noise that provides information on the acoustic wave strength at a particular location in space [83]. SPL measurements are often used to asses the impact of noise, as also done for wind turbines [84], and are useful for comparing the noise levels of different airborne wind energy systems. Moreover, the SPL correlates well with human perception of loudness, as the reference sound pressure is set to the threshold of human hearing, which is equal to $p_{ref} = 2 \cdot 10^{-5}$ Pa [83].

To measure the SPL of an airborne wind energy system, a microphone is used to record the sound pressure at a certain location in the acoustic environment. The measurement is taken at a fixed point. It is important to take into account that SPL measurements can be affected by various factors, such as the wind speed, atmospheric conditions, and the location of the microphone [85]. Although this study did not incorporate explicit corrections for these factors, it is important to recognize their potential impact on the accuracy and reliability of the obtained SPL data. Therefore, the findings should be interpreted with caution and the limitations of the measurement setup should be taken into account.

Besides the acoustic wave strength, it is of interest to take a closer look into the frequency context of those waves. The frequency analysis provides a way to decompose the sound wave into its constituent frequency components and is used to identify specific features of the sound signal. By making use of the Fourier transform, the different frequency components present in a sound wave can be analyzed [86].

INSTRUMENTATION

The audio is recorded by making use of a single microphone, the Brüel&Kjær 4189 microphone connected to a sound calibrator and a microphone preamplifier, which is connected to the Brüel&Kjær 2250 sound level meter, with a windscreen placed over the microphone of type UA-1650 from Brüel&Kjær as well. As specified by Brüel&Kjær [87], the microphone is designed for free-field measurements with high sensitivity over a frequency range of 6.3 Hz to 20 kHz. When making use of the windscreen, the sound level meter has the ability to apply a correction. The specific values of this correction are given in the instruction manual of the sound level meter [87]. The setup of the measurement device is shown in Figure 3.13.

The sound level meter is a single-channel, single-range sound level meter, which means that it only makes use of a single microphone to measure sound pressure levels and is designed to measure within a single range of sound pressure levels (14 dB to 143 dB). Therefore, the sound level meter can only measure the sound pressure levels at a single point in space, and cannot provide information about the directionality or spatial distribution of the acoustic sources.

Data Parameters

The sampling rate and data parameters are important considerations in the acoustic measurement system. The sampling rate refers to the rate at which the sound pressure levels are measured and recorded by the system. This rate determines the frequency range that can be captured by the measurement system. In general, higher sampling rates can capture a wider range of frequencies and provide more accurate measurements of sound power levels. However, higher sampling rates do require more memory and processing power, which results in larger data files that can be more difficult to manage and analyze. The sampling rate of the Brüel&Kjær 2250 is equal to $f_s = 48$ kHz.

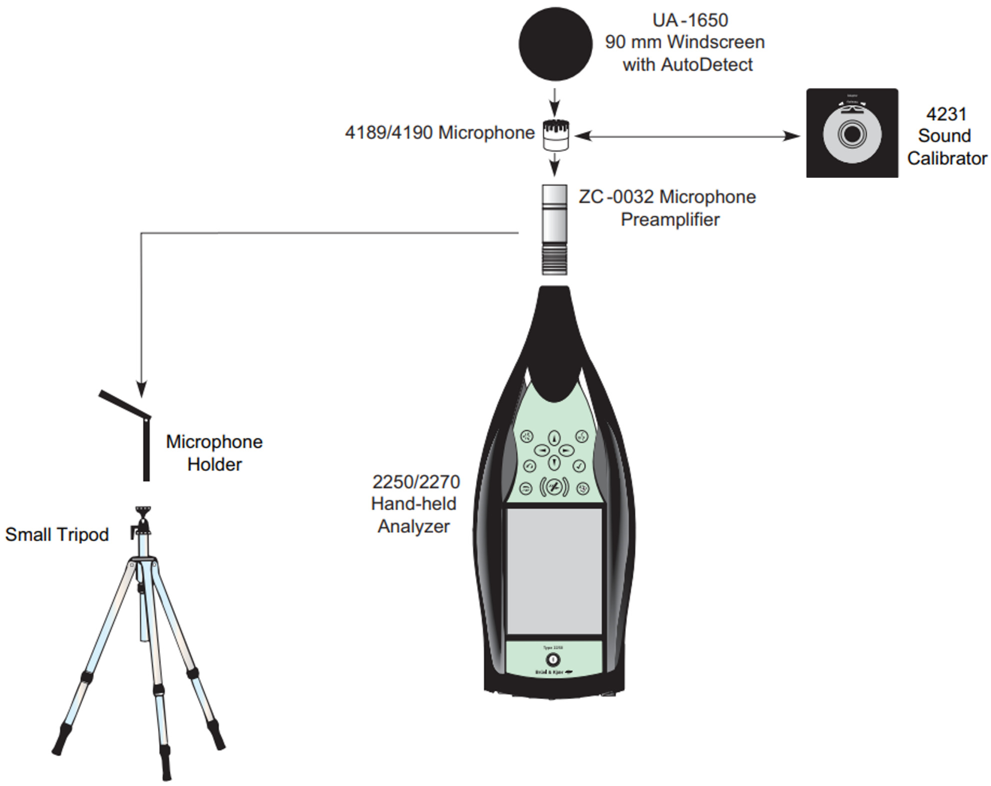

Figure 3.13: Measurement device setup. Obtained from Brüel&Kjær [87].

In addition to the sampling rate, other data parameters, such as the bit depth and file format can impact the accuracy and usability of the acoustic measurements. The bit depth refers to the number of bits used to represent each sample of the sound pressure signal. The bit depth can impact the dynamic range and resolution of the measurements. The Brüel&Kjær 2250 measures sound pressure levels using an analog-to-digital converter (ADC), which converts the analog sound signal into a digital signal that can be analyzed and processed by the device. The Brüel&Kjær 2250 makes use of a 16-bit ADC, which provides a high level of accuracy and resolution for sound level measurements.

The recorded data is stored as a WAV file. WAV files store uncompressed audio and therefore retain all of the original audio data, which ensures high audio quality and fidelity. Note, prior to the analysis, it is necessary, for this particular measurement device, to amplify the data by a factor of 416.8984.

BACKGROUND NOISE

Background noise can have a significant impact on the accuracy and reliability of the measured results and refers to any unwanted sound that is present in the measurement environment. It can introduce additional sound energy that interferes with the desired signal, leading to possible measurement errors. Background noise can come from a variety of sources, such as ambient noise in the surrounding area, electrical or mechanical equipment, or wind and weather conditions.

In order to limit the background noise of the ground components of the airborne wind energy system, the measurement device is placed at a large distance from these components. Additionally, due to the remote locations of the test sites, the ambient noise is limited. However, a primary factor in the background noise for the flight tests is the wind. To limit the influence of the wind, a windscreen is placed over the microphone, as also mentioned in Subsection 3.2.2.

Although the use of a windcap or windscreen on the measurement device (sound pressure level meter) helps to reduce wind noise, it is no guarantee that wind noise will be completely eliminated. Wind noise is caused by the turbulence of air flow around the microphone, which can create variations in pressure and result in unwanted noise. A windscreen helps to reduce this noise by diffusing the incoming wind and preventing it from directly hitting the microphone. This is especially effective for low to moderate wind conditions. However, in very high wind conditions the windscreen may not completely eliminate wind noise. In this study, although the windcap provided some noise reduction, the challenging wind conditions encountered exceeded its capacity to completely eliminate wind noise. The influence of the wind on the measured results should therefore be taken into account when analyzing the data and interpreting the findings.

Background noise can be accounted for in different ways, such as spectral subtraction or by applying a filter. The post-processing of background noise will discussed further in the next part of this subsection.

SIGNAL PROCESSING TECHNIQUES

The WAV files are read in Python by making use of the SoundFile library, which returns an array with the data that was stored in the WAV files, as well as the sample rate of the audio. After obtaining the data array, it can be used for the application of signal processing techniques.

Background Noise

When post-processing the audio recordings of the flight tests, one must also take into account background noise, wind noise in particular for these flight tests. Removing background noise from the audio files can be one of the steps in the audio signal processing. One common approach to removing background noise is spectral subtraction, which works by subtracting the noise spectrum from the signal spectrum [88]. The resulting spectrum contains only the signal components, with the noise components removed. In order to be able to apply spectral subtraction, one must obtain the background noise profile. This can be done by recording an audio file that only contains the background noise.

For the spectral subtraction, both the signal and background noise have to be transformed to the frequency domain by making use of the Fourier transform. The noise spectrum is then estimated by taking the median of the power magnitude of the signal across all time frames. The median filter is then used to smooth the noise spectrum and reduce the effect of spectral outliers. The actual spectral subtraction is carried out by subtracting the estimated noise spectrum from the magnitude of the signal spectrum and makes use of the obtained spectral subtraction factor [88]. This spectral subtraction factor can be adjusted if needed to either remove more or less noise.

While spectral subtraction can be effective in removing some types of noise, it may not be effective in all cases. Some sources of noise are not stationary and may change over time. In such cases, applying a filter may be a more effective approach. For example, a high-pass filter (HPF) can be used to remove low-frequency noise, while a band-pass filter can be used to remove noise within a specific frequency band. The choice of the filter type and parameters depends on the characteristics of the noise and the desired signal. [89]

A HPF is a filter that allows high-frequency signals to pass through, while attenuating or blocking low-frequency signals and is also referred to as a low-cut filter, as it cuts or attenuates frequencies below a certain cutoff frequency. In order to apply a high pass filter, one can make use of the Butterworth filter. This filter is designed to use a set of normalized coefficients that define the filter response, which are the desired filter order and the cutoff frequency. The cutoff frequency is thus required to be normalized to the Nyquist frequency, as this makes the filter parameter independent of the sampling rate of the audio signal, making it easier to apply the filter to audio data sampled at different rates. The Nyquist frequency is defined as half of the sampling rate of the audio signal, $f_N = f_s/2$. The Nyquist frequency is based on the Nyquist-Shannon sampling theorem, which states that in order to accurately represent a continuous signal using discrete samples, the sampling rate must be at least twice the highest frequency contained in the signal. [90]

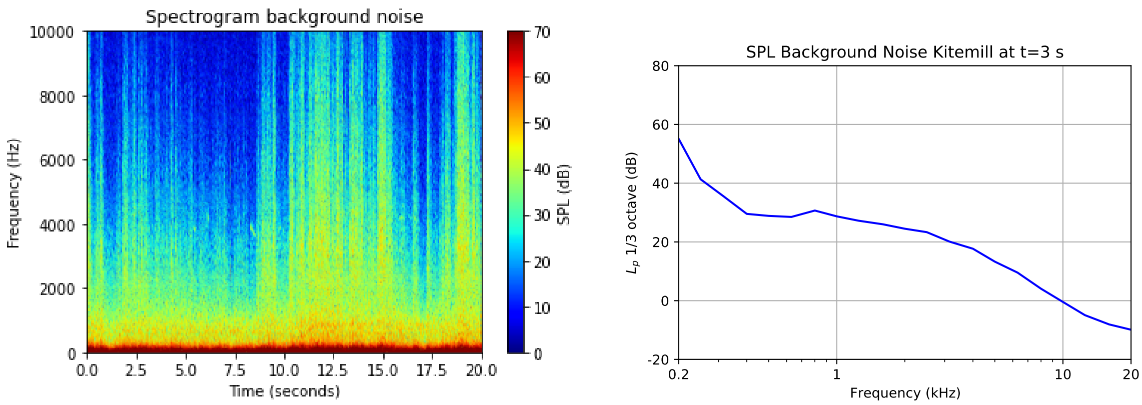

(a) Spectrogram

(b) Sound pressure level at t=3 seconds

Figure 3.14: Signal processing of the audio recorded of the background noise of the flight test of *Kitemill* on March 27, 2023.

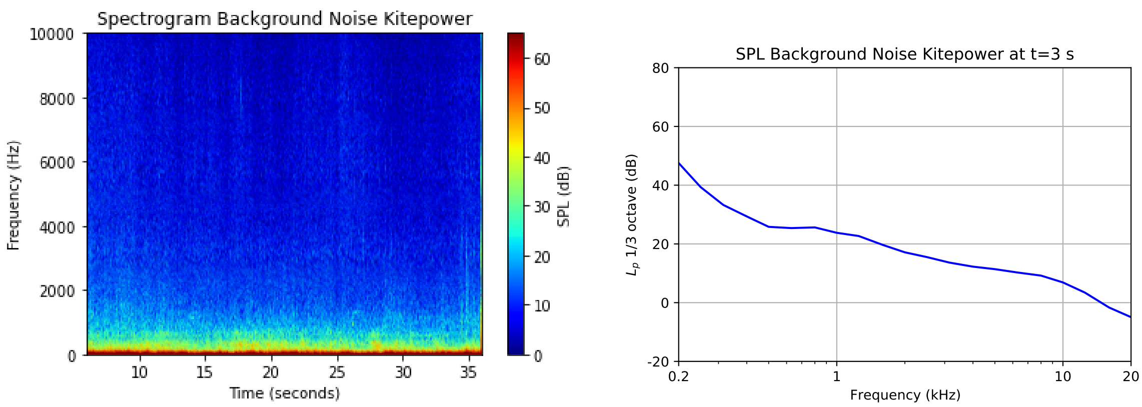

(a) Spectrogram

(b) Sound pressure level at t=3 seconds

Figure 3.15: Signal processing of the audio recorded of the background noise of the flight test of *Kitepower* on May 12, 2023.

Figure 3.14 shows the spectrogram and sound pressure levels for the background noise during the flight test of *Kitemill* on March 27, 2023. It can be seen that the sound pressure levels are the highest for the lowest frequencies, but also appear at the higher frequencies, for which it slowly lowers the sound pressure level. Figure 3.16 presents the audio of a random moment during the production phase of the flight test of *Kitemill*. Also for these plots, it can be seen that the background noise has a significant effect on especially the lower frequencies. A similar pattern can be found for the background noise during the flight test of *Kitepower* on May 12, 2023, although the higher frequency noise is a bit less compared to *Kitemill*.

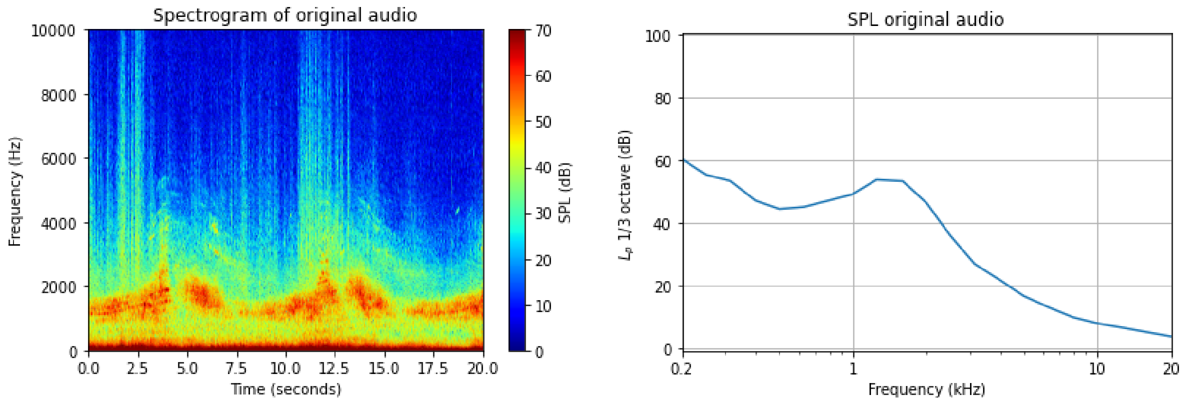

(a) Spectrogram

(b) Sound pressure level at t=3 seconds

Figure 3.16: Example audio of the recording of the flight test of *Kitemill* on March 27, 2023.

In order to observe the effect of the different methods to remove the background noise, Figure 3.17 and Figure 3.18 have been created. Although, removing the background noise by either spectral subtraction, applying a high-pass filter or a combination of both, clearly highlights the peak frequency of the system, it does remove more than desired from the spectrum, as can be seen in Figure 3.18. For this reason, the signal processing for the analysis in Chapter 4 does not have the background noise removed from the audio recordings.

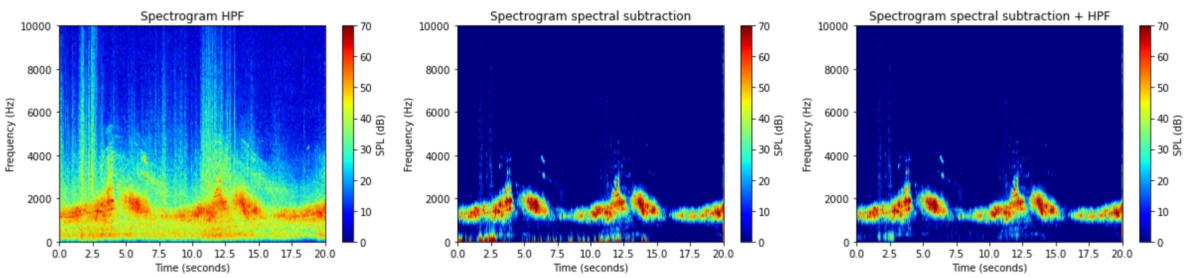

(a) High-pass filter

(b) Spectral subtraction

(c) Spectral subtraction plus a high-pass filter

Figure 3.17: Spectrograms for different methods of background noise removal.

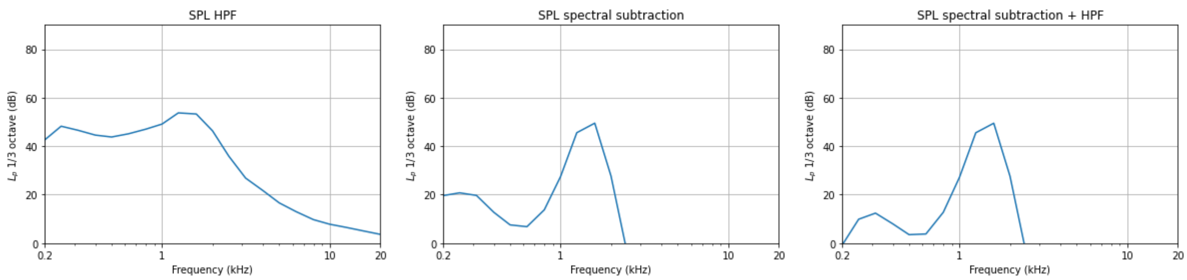

(a) High-pass filter

(b) Spectral subtraction

(c) Spectral subtraction plus a high-pass filter

Figure 3.18: Sound pressure levels for different methods of background noise removal.

Windowing
The analysis is based on a finite set of data, while the actual Fourier transform assumes a finite data set where the endpoints are interpreted as though they were connected. The finiteness of the data set may result in a truncated waveform with different characteristics that could result in sharp transition changes in the measured signals, which equals discontinuities. To minimize this effect, a technique is used called windowing. Windowing consists of multiplying the recorded data set by a finite-length window with an amplitude that varies smoothly and gradually towards zero at the edges. This ensures that the endpoints of the waveform meet, which therefore results in a continuous waveform without the sharp transitions. [91]

Windowing is a common signal processing technique used in acoustic measurements to thus reduce the effect of spectral leakage and improve the accuracy of the frequency analysis. Spectral leakage is the phenomenon that occurs when a signal is analyzed using Fourier analysis with a finite duration window, resulting in spectral "smearing" and a reduced frequency resolution. In other words, spectral leakage occurs due to the spectrum of a signal leaking into adjacent frequency bins due to the truncation of the signal in the time domain during the Fourier transform of a non-periodic signal. Spectral leakage can cause errors in frequency analysis and is therefore desired to be kept to a minimum. [91]

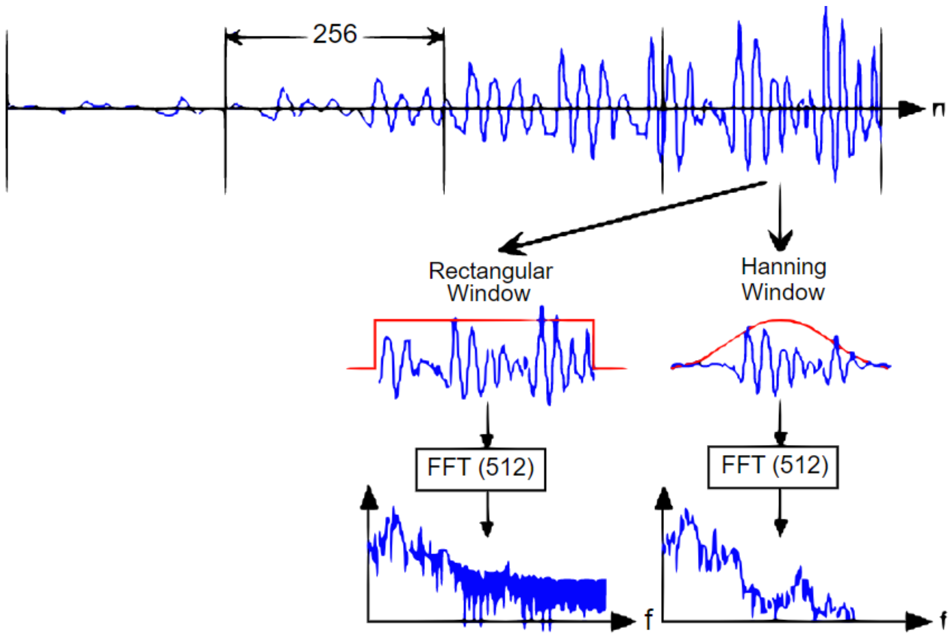

Figure 3.19: Application of a rectangular window versus a Hanning window. Obtained from Johnson [92].

As mentioned before, windowing involves multiplying the measured data by a window function, which reduces the amplitude of the signal at the edges of the window and improves the frequency resolution of the Fourier analysis. However, there are many different types of window functions that can be used, each with their own characteristics and advantages. Common window functions are the Hanning window, the Hamming window, and the Blackman-Harris window, among others. The Hanning window is a common used window for acoustic measurements, as it provides a good balance between frequency resolution and spectral leakage. The Hamming window has a slightly sharper roll-off than the Hanning window and is usually preferred when the signal contains sharp features, such as sudden transitions or impulse-like events. [91] However, the Hamming window does have more spectral leakage than the Blackman-Harris window. The Blackman-Harris window on the other hand has a more complex shape than the Hanning window and provides better frequency resolution and lower levels of spectral leakage. However, this also comes with a higher required processing power and can introduce additional noise into the measurement [93]. A visualization of the effect of the Hanning window versus a rectangular window is shown in Figure 3.19. The rectangular window is not yet mentioned, as although it is easy to apply, it does induce spectral leakage, which affects the accuracy of the frequency analysis.

As mentioned, the Hanning window provides a good balance between frequency resolution and spectral leakage, without the need of high processing power, as would be the case for the Blackman-Harris window. Therefore, the Hanning window is applied for the signal processing of the obtained audio recording of the airborne wind energy system.

Frequency-domain Analysis

The frequency-domain analysis involves transforming the time-domain signal into the frequency domain using the Fourier transform. For this analysis the Short Time Fourier Transform (STFT) is applied. The STFT is a sequence of Fourier transforms of a windowed signal. This makes the STFT capable of providing frequency information that is localized in time, meaning the analysis of the signal's frequency content is performed over short intervals of time rather than over the entire duration of the signal, which is useful in cases where the frequency components of a signal vary over time. In contrast, the standard Fourier transform provides the frequency information averaged over the entire signal time interval. As the STFT has smaller time frames, consequently, the frequency spectrum moves smoother over time than for example for the Fast Fourier Transform (FFT), and is therefore more accurate.

An important parameter to take into account when performing the frequency-domain analysis is the bin size. The bin size determines the frequency resolution of the spectrum and is directly related to the sampling rate and the length of the recorded data. A smaller bin size results in a higher frequency resolution, but also requires a longer data record to obtain a reliable estimate of the spectrum. Conversely, a larger bin size results in a lower frequency resolution, but requires a shorter data record and can be more computationally efficient. Moreover, the bin size also influences the magnitude of the SPL, as the bin size affects the frequency resolution of the Fourier transform, which in turn affects the accuracy of the SPL measurement. Although a smaller bin size provides a better frequency resolution, it may cause less accurate SPL results [93]. The bin size is thus a trade-off between frequency resolution, computational time and data accuracy.

The bin size is determined by making use of the following equation:

$$N = 2^M. \tag{3.12}$$

As it is a power of two, the efficiency of the Fourier algorithm is optimized [94].

Like mentioned before, selecting the appropriate bin size requires a balance between frequency resolution, computational time and data accuracy. In order to investigate the effect of the bin size on computational time, Fourier transforms have been performed on a audio recording of 20 seconds using bin sizes raging from 256 to 2048. The results of this investigation are shown in Table 3.2. This suggest that for this case, the choice of bin size may have little impact on the computational time required for the Fourier transform.

Bin size	256	512	1024	2048
Computational time, s	2.843	2.770	2.711	2.604

Table 3.2: Comparison of the bin size versus the computational time. The hardware makes use of an Intel Core i7-9750H processor.

To further evaluate the effect of the bin size on the frequency resolution and the SPL calculation, spectrograms (Figure 3.20) and SPL plots (Figure 3.21) have been obtained for the same 20 second audio recording as mentioned before. The SPL values are obtained at a specific time point for each bin size, which is equal to 3 seconds in the spectrograms.

The spectrograms clearly demonstrate the trade-off between frequency resolution and spectral details. Using a larger bin size (e.g., 2048 (Figure 3.20d)) improves frequency resolution and produces smoother spectrograms with less frequency leakage. However, for the SPL values, a larger bin size averages the values over a wider frequency range, potentially obscuring important spectral details. Conversely, a smaller bin size (e.g., 256 (Figure 3.21a)) increases the sensitivity of the SPL calculation to small variations in the spectrum.

After careful consideration of these trade-offs, a bin size of 1024 is selected as a reasonable compromise. This choice strikes a balance between capturing essential spectral details and avoiding excessive sensitivity to minor variations in the spectrum.

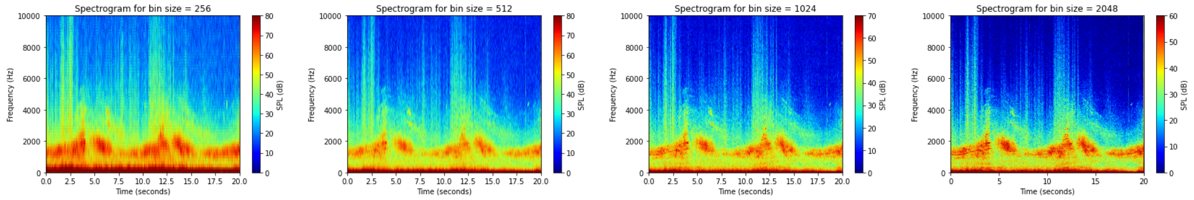

(a) Bin size = 256 (b) Bin size = 512 (c) Bin size = 1024 (d) Bin size = 2048

Figure 3.20: Spectrograms of the audio recording obtained at the *Kitemill* flight test in March 2023 for different bin sizes.

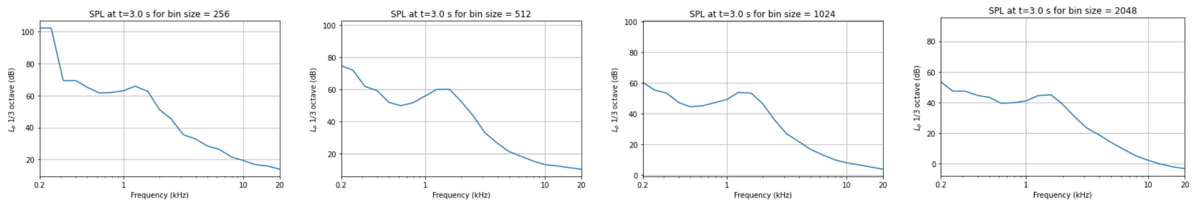

(a) Bin size = 256 (b) Bin size = 512 (c) Bin size = 1024 (d) Bin size = 2048

Figure 3.21: SPL plots of the audio recording obtained at the *Kitemill* flight test in March 2023 for different bin sizes.

Sound Pressure Level

One of the things that can be obtained from the frequency domain analysis is the sound pressure level (SPL). Once the signal has been converted to the frequency domain, the power spectral density (PSD) can be calculated. The PSD is found by squaring the absolute value of the Fourier transform output. The PSD is then used to obtain the SPL, as shown in the following equation:

$$\mathrm{SPL} = 10 \cdot \log\left(\frac{\mathrm{PSD} \cdot df}{p_{ref}^2}\right), \tag{3.13}$$

with again the reference pressure being the threshold of human hearing, thus $p_{ref} = 2 \cdot 10^{-5}$ Pa.

The SPL can be analyzed and presented in different frequency bands, such as 1/1 octave and 1/3 octave bands. 1/1 octave and 1/3 octave refer to the division of the frequency spectrum into different frequency bands. In 1/3 octave analysis, the frequency range is divided into logarithmic spaced band where each band has a approximately a width of one-third of an octave. A 1/3 octave representation can result in a cleaner plot than the original measured data.

Even more, the sound pressure level can be scaled to examine the relationship between the sound pressure level and other variables, such as distance and kite velocity. By scaling the sound pressure level, the research aims to normalize the noise. In order to scale the sound pressure level with respect to distance, the inverse square law principle is used, which states that sound intensity decreases proportionally to the square of the distance from the source [95]. By applying this principle, the measured sound pressure level is scaled to account for the varying distances between the microphone and the kite during the data collection.

$$\mathrm{SPL}(r_{ref} = 1m) = \mathrm{SPL}(r_m) - 20 \cdot \log_{10}\left(\frac{r_{ref}}{r_m}\right). \tag{3.14}$$

Similarly, to account for the influence of the kite velocity on noise emissions, a scaling factor can be applied. A common scaling approach for airfoil trailing edge noise is given in Equation 3.15 [96]. The experiments of Brooks et al. [37] showed that for trailing edge noise the exponent n is in the range of 4.5 to 5. However, the exact value of the exponent for this research has yet to be determined based on the results of the measurements.

$$\mathrm{SPL}(U_{ref} = 1m/s) = \mathrm{SPL}(U_m) - 10 \cdot \log\left(\frac{U_m}{U_{ref}}\right)^n. \tag{3.15}$$

Spectrogram
The spectrogram is a visual representation of how the spectral content of a signal changes over time. It is obtained by dividing the signal into small segments and taking the frequency content for each segment. The results are then stacked to create a two-dimensional image in which the x-axis represents time, the y-axis represents frequency, with the intensity of the color indicating the magnitude of the SPL at that time and frequency.

Time-domain Analysis
One of the fundamental measurements in the time-domain is the measurement of the overall sound pressure level (OSPL) over time. The OSPL quantifies the total sound energy present in a given sound field. This can be used to characterize the noise level of a particular environment or source. The OSPL is calculated by taking the root-mean-square (RMS) of the sound pressure values over a certain time interval and frequency range, which is also referred to as the effective pressure (p_{eff}). The OSPL is thus given as follows:

$$\mathrm{OSPL} = 10 \cdot \log\left(\frac{p_{eff}^2}{p_{ref}^2}\right), \tag{3.16}$$

the reference pressure has a value of $p_{ref} = 2 \cdot 10^{-5}$ Pa, as also in the previous instances.

The OSPL is an unweighted representation of the total sound pressure level, which is also referred to as the Z-weighting. Another representation is the A-weighted overall sound pressure level. The A-weighted overall sound pressure level, also referred to as OASPL or L_A, represents the human ear's response to sound pressure levels. The A-weighting curve, shown in Figure 3.22, is based on a set of weightings filters that mimic the response of the human ear to sound at different frequencies. The curve attenuates low and high frequencies, while giving more weight to frequencies in the range of human speech and other important sounds. [97]

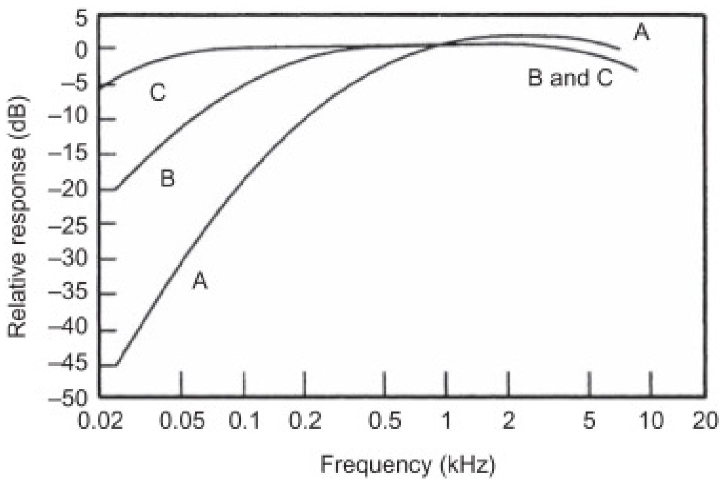

Figure 3.22: SPL frequency weightings. Obtained from Martyr and Rogers [97].

The A-weighting filter is, according to the International Electrotechnical Commision (IEC) 61672-1:2013 [98], represented by the following equation:

$$\Delta L_A = -145.528 + 98.262\log(f) - 19.509\big(\log(f)\big)^2 + 0.975\big(\log(f)\big)^3, \tag{3.17}$$

with f being the frequency. This value has to be added to the sound pressure level found at the respective frequency. The OASPL is then obtained by making use of the following equation:

$$OASPL = 10 \cdot \log\left(\sum_i 10^{\frac{Lp(i)+\Delta L_A(i)}{10}}\right), \tag{3.18}$$

which gives the overall A-weighted sound pressure level in dBA.

4

Results

4.1. Experimental Results and Analysis

This section presents the results of the noise measurement campaigns conducted to assess the aeroacoustic characteristics of the airborne wind energy systems developed by *Kitemill* and *Kitepower*. The data collected from these experiments will be analyzed in this section, which results in the identification of some key findings related to the noise emission of the systems.

4.1.1. Kitemill

The results are divided into two phases: the takeoff phase and the production phase. The takeoff phase takes about 2.5 minutes and the production phases lasts for about 6 minutes. For the takeoff phase, the period near the end of the phase is selected, after which it transitions to the production phase. Also, for the production phase, a single period is selected to be presented, as the characteristics, and therefore the results, are repetitive throughout the production phase.

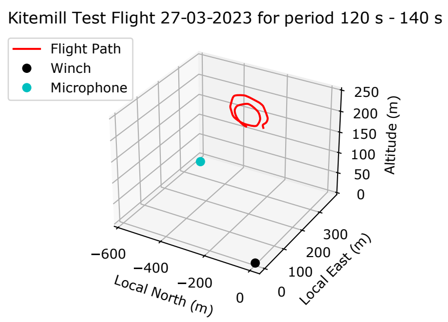

(a) Period 120 s to 140 s

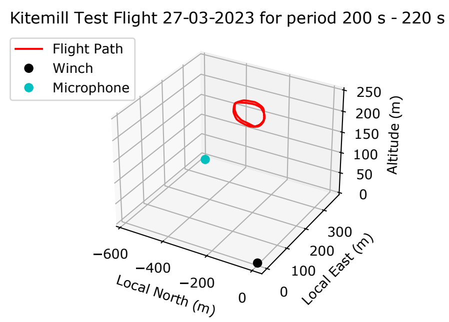

(b) Period 200 s to 220 s

Figure 4.1: Flight path of the KM1 kite for two periods during the flight test of *Kitemill* on March 27, 2023.

Takeoff

The results presented for the takeoff phase are taken for the period 120-140 seconds. The flight path for this period is shown in Figure 4.1a, from which it can be seen that the kite gets into position and starts flying its loops. During this period, the first 8 seconds are within the takeoff phase, from which it transitions to the production phase that starts around 10-11 seconds into this period. This is also seen in the spectrogram in Figure 4.2. For the takeoff phase, the VTOL motors are turned on for which the distinctive tonal components, with decreasing intensity for the higher frequencies can be seen.

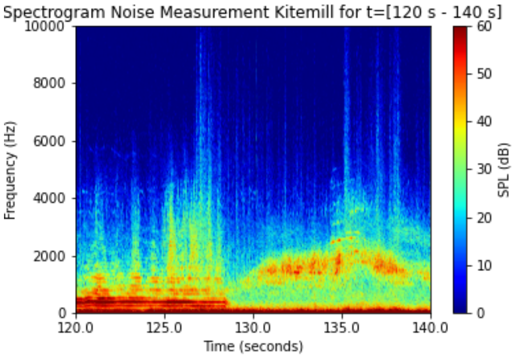

Figure 4.2: Spectrogram for the period 120-140 s of the *Kitemill* flight test on March 27, 2023.

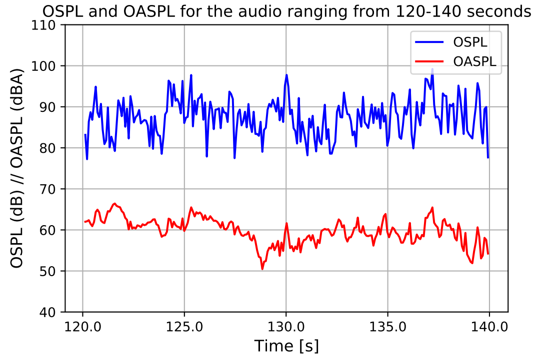

Figure 4.3: OSPL and OASPL for the period 120-140 s of the *Kitemill* flight test on March 27, 2023.

From Figure 4.3, it can be seen that the overall sound pressure levels are higher during the takeoff phase than during the production phase. Also in this graph, the clear transition from one phase to the other can be seen by the dip in the plots. Moreover, the takeoff phase has the higher sound pressure levels located at the lower frequency range, which results in the A-weighted overall sound pressure level to become lower than the Z-weighted sound pressure level, as the human hearing is less sensitive to this frequency range.

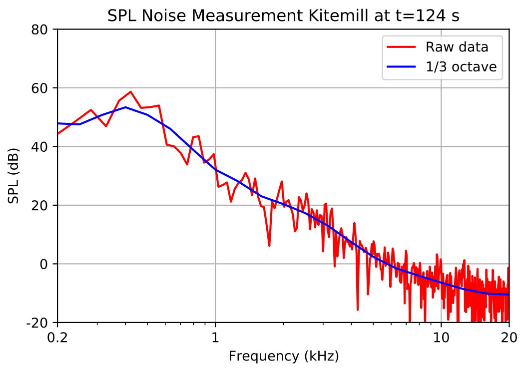

(a) t=124 s

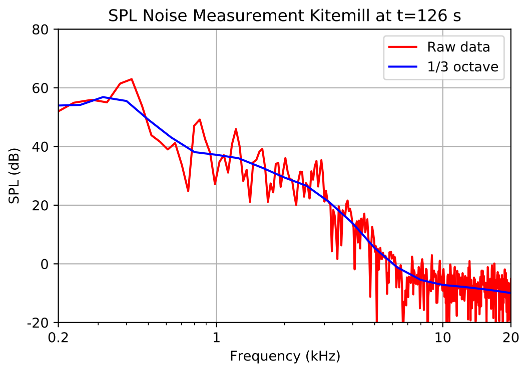

(b) t=126 s

Figure 4.4: Sound pressure levels for different moments during the takeoff phase of the *Kitemill* flight test on March 27, 2023.

To get a better idea of the tonal components during the takeoff phase, the sound pressure levels for two particular moments are presented in Figure 4.4, namely at t=124 s and t=126 s. Looking at the raw data plots of Figure 4.4a and Figure 4.4b present the tonal peaks of the propellers, as well as the broadband component included in that spectrum. The sound pressure levels reach a peak of approximately 60 dB, observed within the frequency range of 300-400 Hz. Even more so, a notable observation is the dominance of sound pressure levels in the low-frequency range, specifically between 200 Hz and 1000 Hz. This behavior aligns with the expected acoustic signature of a propeller. Propeller noise typically exhibits higher sound pressure levels at lower frequencies due to the interaction of the rotating blades with the surrounding air. This is further supported by the presence of tonal components in the noise, which tend to be more pronounced at lower frequencies as well.

It is also important to consider the contribution of background noise, predominantly caused by wind, to the overall sound pressure levels during the take-off phase. This background noise predominantly affects the lower frequencies of the spectrum, adding to the sound levels observed in that range. The combination of propeller noise and wind-induced background noise results in the characteristic frequency distribution observed in the plots.

To summarize, during the take-off phase of the *Kitemill* system, the observed sound pressure levels exhibit characteristics expected for propeller-driven systems. The dominance of sound levels in the lower frequency range, along with the presence of tonal components and wind-induced background noise, contribute to the overall acoustic signature. The A-weighting scale, which takes into account the sensitivity of human hearing to different frequencies, decreases the calculated overall sound pressure level, particularly due to the highest sound pressure levels found on the lower frequency range of the spectrum.

Production

The results for the production phase are taken for the period 200-220 seconds of the production phase, for which the flight path can be seen in Figure 4.1b. During this period two full loops have been flown. To be able to better relate the measured noise to the flight data, the flight data for that same period of time is presented in Figure 4.5. From these plots, it can be seen that the airspeed is at a maximum when the kite altitude is at a minimum and vice versa. Also, the radius from kite to the microphone varies between about 305 meters and 385 meters and is the furthest away from the microphone at the highest altitude, which can be seen in Figure 4.5d. The spectrogram for this period is shown in Figure 4.6, from which the repetitive pattern for the circular flight path can be recognized. Besides the spectrogram, also the overall sound pressure level (A-weighted and Z-weighted) and the sound pressure levels at a particular time are presented in Figure 4.7 and Figure 4.8, respectively.

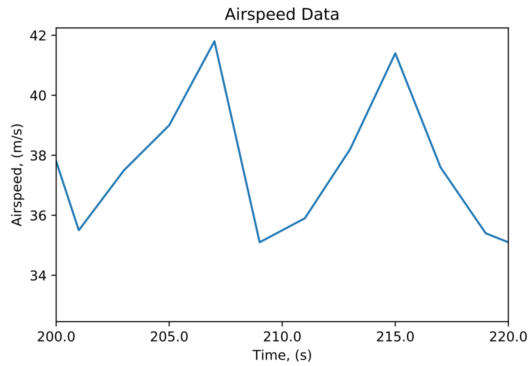

(a) Airspeed

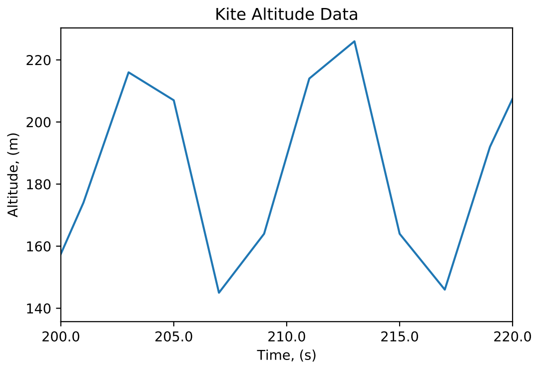

(b) Kite altitude

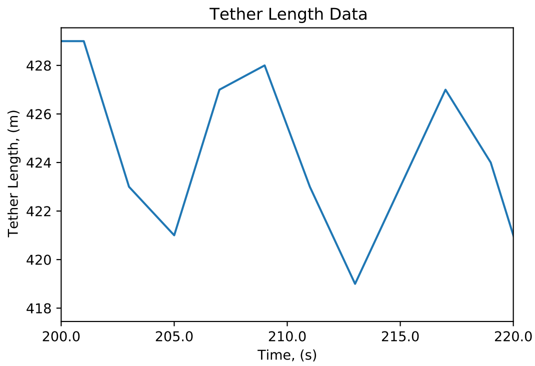

(c) Tether length

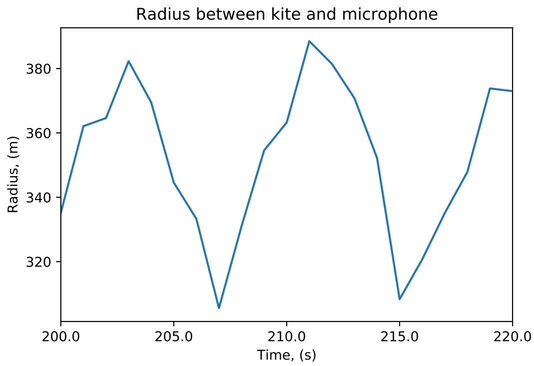

(d) Radius between kite and microphone

Figure 4.5: Data of the test flight of *Kitemill* on March 27, 2023 for the period 200 s to 220s.

Taking a closer look at the spectrogram in Figure 4.6, it can be seen that the same pattern can be recognized as shown by the kite altitude data in Figure 4.5b. Therefore, the higher SPL values are situated at higher frequencies when the kite is flying at higher velocities. Additionally, the spectrogram analysis reveals higher SPL values between the frequency range from 1000 Hz to 2200 Hz. These frequencies are within the mid-frequency range and are known to be particularly sensitive to human hearing. Nonetheless, due to the contribution of the lower range frequency, the A-weighted overall sound pressure levels are still lower than the Z-weighted overall sound pressure levels, as can be observed in Figure 4.7. The OSPL and OASPL values are within the range from 75 dB to 100 dB and from 50 dBA to 65 dBA, respectively.

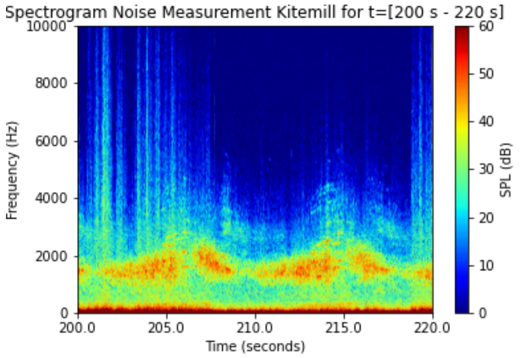

Figure 4.6: Spectrogram for the period 200-220 s of the *Kitemill* flight test on March 27, 2023.

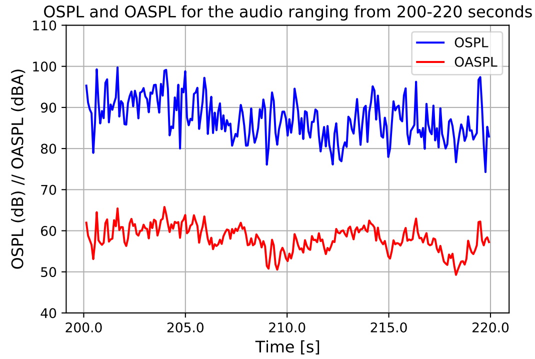

Figure 4.7: OSPL and OASPL for the period 200-220 s of the *Kitemill* flight test on March 27, 2023.

The spectra in Figure 4.8 all show clear tonal peaks around 1000 Hz to 2000 Hz. The spectrum in Figure 4.8a is at the moment the kite is close to reaching its highest point in the cycle, where the kite is just past its lowest velocity. At t=203 s, there appears to be a relatively broad peak, which have its center around 1500 Hz. The next moment for which the sound pressure levels are shown is at t=207 s in Figure 4.8b. At this time, the kite is at its lowest point in the cycle, where the kite reaches the maximum velocity. Again, a peak can be recognized, especially when looking at the 1/3 octave plots. For this case, the peak is centered around 2000 Hz. The characteristics of the plot at t=212 s (Figure 4.8c) is close to those at t=203 s, with a peak situated around 1500 Hz as well. The same goes for the plot at t=214 s (Figure 4.8d), which has similar characteristics as the plot at t=207 s. The tonal peak at t=214 s is located at 1900 Hz.

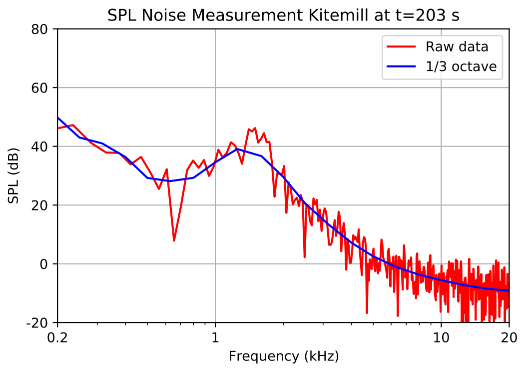

(a) t=203 s

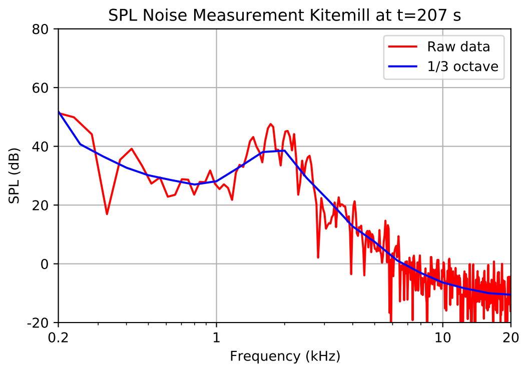

(b) t=207 s

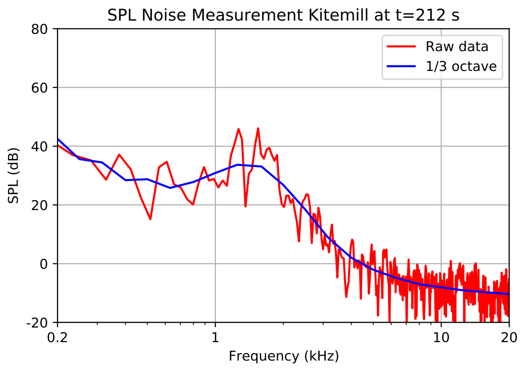

(c) t=212 s

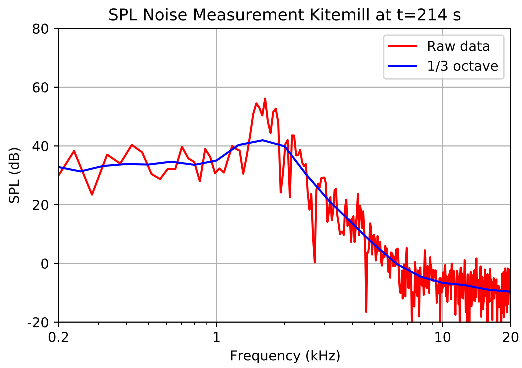

(d) t=214 s

Figure 4.8: Sound pressure levels for different moments during the production phase of the *Kitemill* flight test on March 27, 2023.

An additional analysis has been conducted to gain insights into the relationship between the sound pressure level and relevant parameters, such as airspeed and the distance between the microphone and the kite. To facilitate this analysis, a plot has been generated: the sound pressure level scaled with the distance between the microphone and the kite.

The scaled sound pressure levels are shown in Figure 4.9. In this plot, the sound pressure levels are solely scaled with the distance. This choice is made as the velocities of the cases are very similar, resulting in minimal or negligible differences when scaling the data with velocity. Furthermore, the sound pressure level is plotted versus the Strouhal number, which has been obtained by making use of the mean chord of the kite. By scaling the sound pressure level with the distance, a distinct peak is observed across all data sets, occurring at $St_c = 15$.

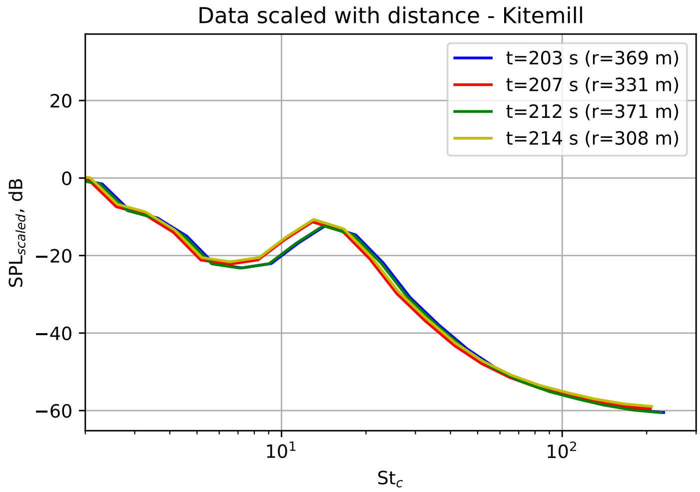

Figure 4.9: Sound pressure levels of the *Kitemill* flight test of March 27, 2023 scaled with distance.

4.1.2. KITEPOWER

For the results of *Kitepower* a period is selected for which the figure-of-eight flight path was completed at least once. The period that has been selected ranges from 180 seconds to 210 seconds with the launch of the kite being the start of the flight. From Figure 4.10, it can be seen that the kite moves upwards towards the right of the plot first, from which it then continues its pattern downwards and to the left. This can be confirmed by taking a look at the flight data that is presented for this period in Figure 4.12.

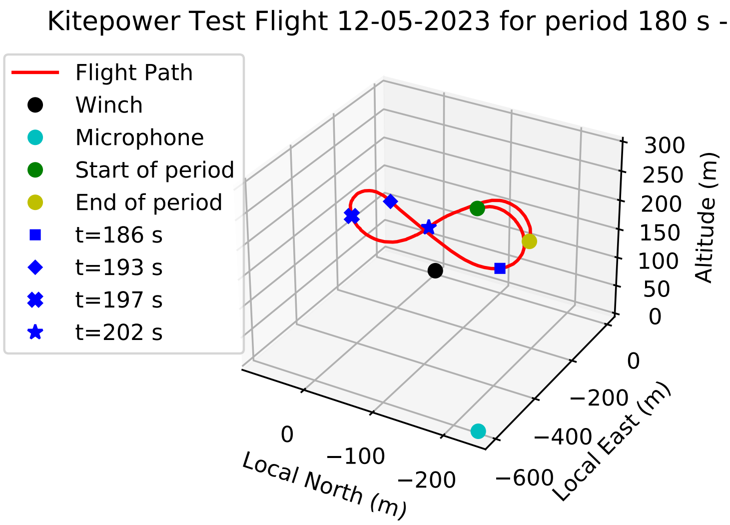

Figure 4.10: Flight path of the V9.60 kite for the period 180 s to 210 s during the flight test of *Kitepower* on May 12, 2023.

In order to visualize the positioning of the kite during the flight of its pattern, a time-lapse photo has been create of the full figure-of-eight loop flown in the selected period, which can be seen in Figure 4.11. These photos have been taken from the position of the microphone. Also in this figure, the kite first moves upwards to the right and continues the loop towards the left from there.

Figure 4.11: Figure-of-eight flight path of the V9.60 *Kitepower* kite during the flight test on May 12, 2023.

During the selected cycle the airspeed varies between 20 m/s and 38 m/s (Figure 4.12c), the altitude remains between 105 m and 205 m (Figure 4.12a) and the direct distance, or radius, between the kite and the microphone is between 440 m and 545 m (Figure 4.12b).

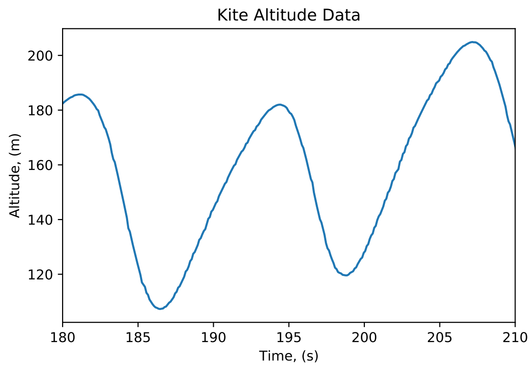

(a) Altitude

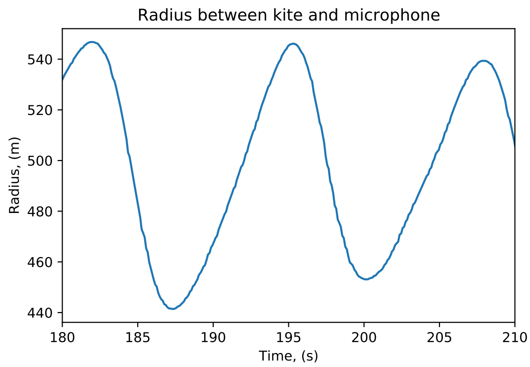

(b) Radius between kite and microphone

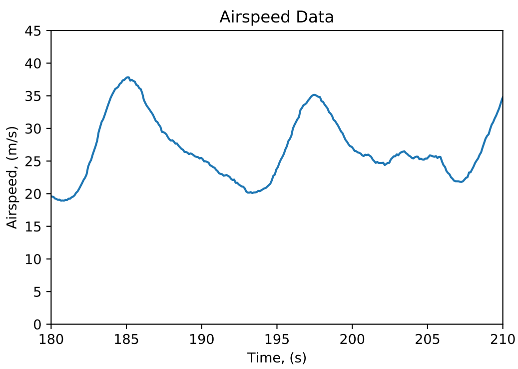

(c) Airspeed

Figure 4.12: Data of the test flight of *Kitepower* on May 12, 2023 for the period 180 s to 210 s.

The spectrogram of this period, presented in Figure 4.13, shows that most of the sound is produced for the lower frequency range with some tonal patterns for the frequency range between approximately 200 Hz and 2000 Hz. It appears that the higher frequency noise is emitted when the kite is experiencing the highest velocities. This moment is when the kite has just flown one loop and is at the bottom of that loop and is thus about to switch from one loop to the other, as also indicated by the location of the kite in Figure 4.13. A closer look can be taken from the plots in Figure 4.14 of the sound pressure levels for the four selected moments in the period: t=186 s, t=193 s, t=197 s and t=202 s. The sound pressure level plots of all selected times show similar patterns, but do show minor difference. The 1/3 octave plots of Figure 4.14a, Figure 4.14b and Figure 4.14d show a bump around 300-400 Hz, while this is less apparent in Figure 4.14c. Especially in Figure 4.14b a bump can be observed around 1000 Hz. Taking a closer look at the raw data of the other plots, peaks can be found here as well for the range 800-2000 Hz, although their sound pressure levels remain lower than that of Figure 4.14b.

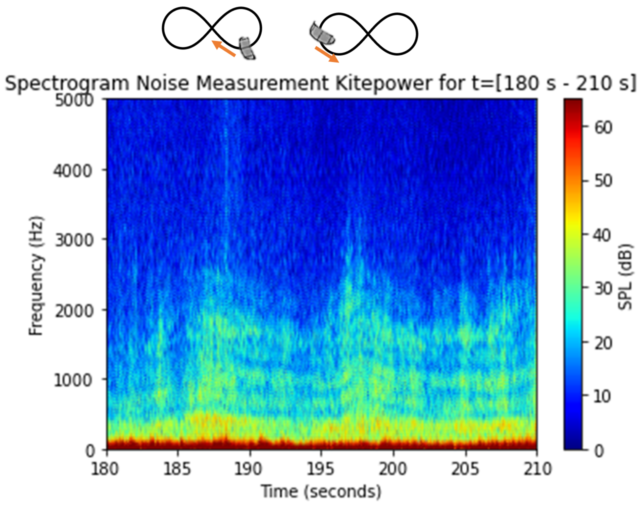

Figure 4.13: Spectrogram for the period 180-210 s of the *Kitepower* flight test on May 12,2023.

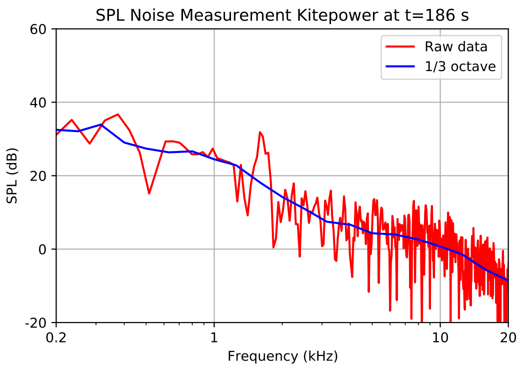

(a) t=186 s

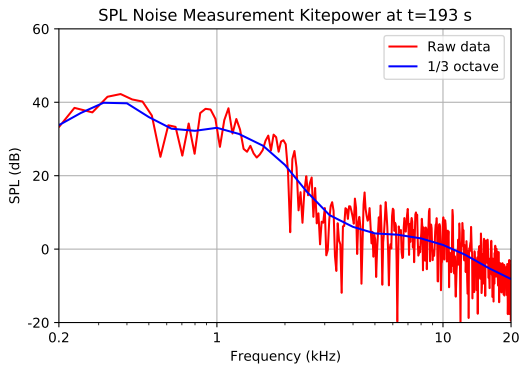

(b) t=193 s

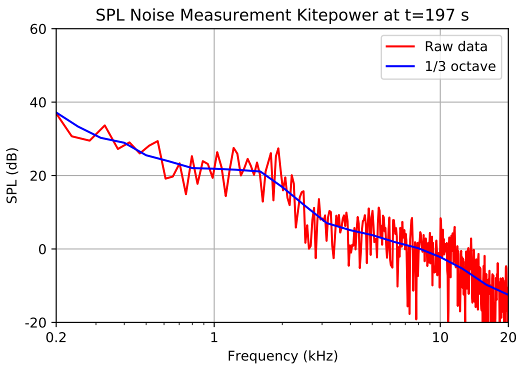

(c) t=197 s

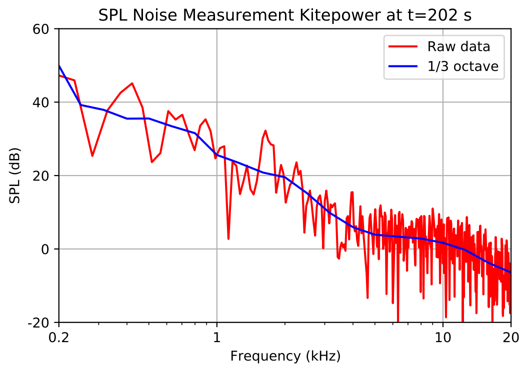

(d) t=202 s

Figure 4.14: Sound pressure levels for different moments during the production phase of the *Kitepower* flight test on May 12, 2023.

Besides the flight data, also the available video footage has been analyzed for the same period. The video recorded from the tip of the kite, gives a good view on the trailing edge flutter and seam-rippling of the kite during the flight. Although it is remains challenging to determine the exact frequency at which these phenomena occur, it does make it possible to determine when a phenomenon occurs and also some differences between the occurrences at different moments in time. The video showed that at t=193 s the kite was under less tension compared to the other times and even experienced quite some seam-rippling. Furthermore, for the full period, the kite experienced trailing edge flutter in varying intensities. Within the period analyzed above, the flutter appeared to be slightly less at t=197 s. In Figure 4.15, trailing edge flutter is visualized with the video footage obtained of the V3 kite from a test flight on March 30, 2017.

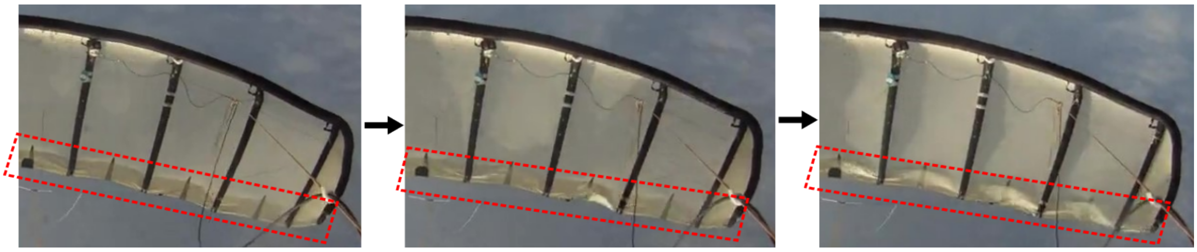

Figure 4.15: Trailing edge flutter occurring on the V3 kite during the test flight on March 30, 2017. Adapted from Schmehl and Oehler [99].

Once again, an additional analysis is conducted to gain insights into the relationship between certain parameters. In contrast to the analysis of *Kitemill*, the plot for *Kitepower* shows a broadband spectrum rather than a distinct peak. For the scaling with velocity, the exponent in Equation 3.15 that results in the best scaling is found to be $n = 4.5$, with the reference velocity being the intermediate velocity of the data set ($U = 24.7$ m/s). As mentioned by Oerlemans[100], broadband trailing edge noise scales with $U^{4.5}$, which aligns with these scaling results. Although, this simple scaling model results in a good first estimation, it is evident that a more sophisticated model is needed to more accurately describe the dependence of the sound emission on the Strouhal number.

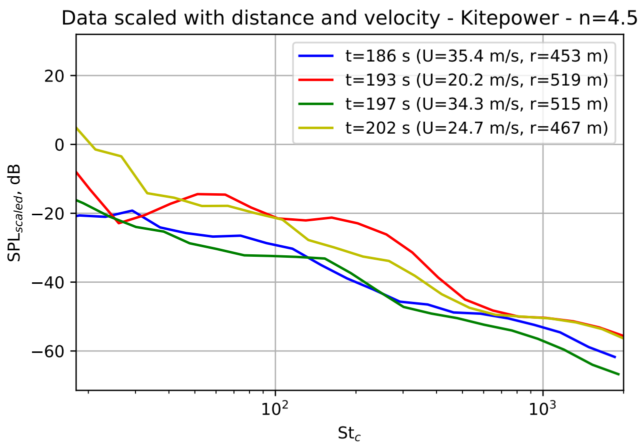

Figure 4.16: Sound pressure levels of the *Kitepower* flight test of May 12, 2023 scaled with the distance and velocity.

4.2. Experimental-Analytical Comparison

In order to gain useful insights into the acoustic behavior of airborne wind energy systems, a comparison between experimental measurements and analytical predictions is valuable. This comparison allows for an assessment of the agreement between the recorded sound levels and the estimated levels calculated using the analytical models. By conducting this analysis, the sources of noise in these systems can be identified, contributing to an enhanced understanding of their acoustic characteristics. In this section, a comparison is presented between the sound pressure level spectra obtained from the experimental measurements of the *Kitemill* and *Kitepower* systems, and the corresponding analytical predictions. The analytical predictions were performed using the computational model as discussed in Section 3.1 , considering two cases for which different conditions apply.

4.2.1. KITEMILL

The input of the boundary layer parameters are obtained from XFOIL. The input for obtaining these parameters, are taken for t=203 s and t=207 s. Additionally, the dimensions of the KM1 kite are used as mentioned in Subsection 2.1.1 and an angle of attack of 8° is used.

The results of the noise prediction for the KM1 kite are shown in Figure 4.17 and Figure 4.18. Also, the overall sound pressure levels have been obtained for these cases, which resulted in the values presented in Table 4.1.

The pressure level spectra obtained from the experiment and the predictions are compared for two different cases of the *Kitemill* airborne wind energy system. As shown in the previous section, Subsection 4.1.1, the experimental results showed a broad peak centered around 1500 Hz for t=203 s, and 2000 Hz for the case at t=207 s. The predicted results showed two peaks, which were caused by the laminar boundary layer vortex shedding and the vortex shedding of the tether. These peaks are found to be around 1400 Hz and 1900 Hz for the lower velocity case, and 2100 Hz and 2600 Hz for the high velocity case.

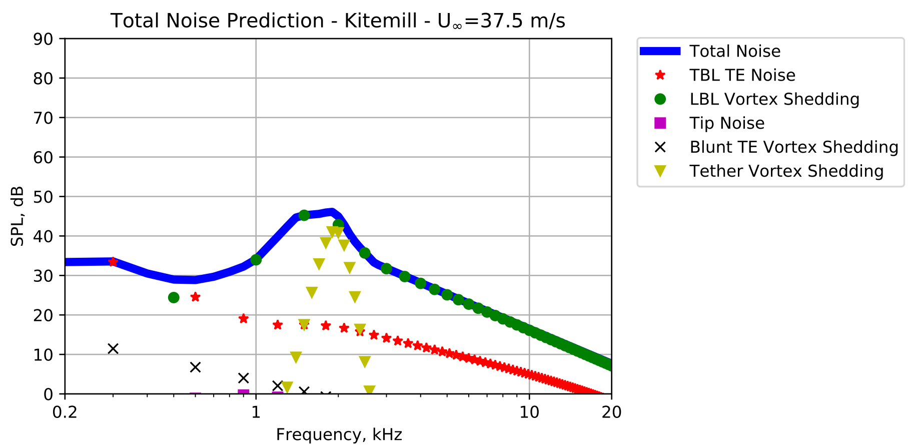

Figure 4.17: Sound pressure level spectrum for $U_\infty = 37.5$ m/s of the KM1.

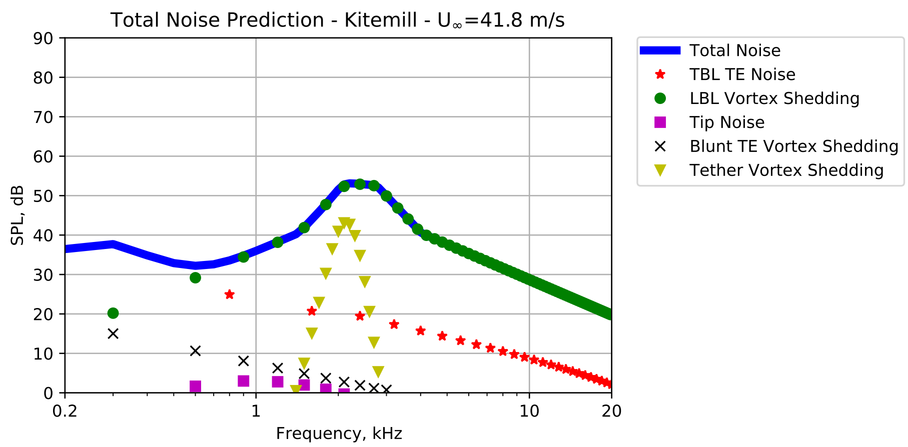

Figure 4.18: Sound pressure level spectrum for $U_\infty = 41.8$ m/s of the KM1.

It should be noted that the Doppler effect was not taken into consideration in the predictions, as the Mach numbers are low, and therefore the Doppler effect remains limited. Additionally, XFOIL is a low-fidelity tool, and therefore could produce less accurate input parameters.

Time, s	OSPL, dB	OASPL, dBA
203	64.38	65.54
207	55.69	56.68

Table 4.1: Overall sound pressure levels for the predicted spectra of the KM1.

To obtain a better view of the measured versus the predicted spectra, both results are plotted in the same figure for both cases in Figure 4.19 and Figure 4.20. The prediction shows to overestimate the sound pressure level for the peak and higher frequencies. Also, the frequency of the peak is slightly overpredicted. The difference at the lower frequencies is most likely to be due to the background noise that has not been excluded from the measured data. The discrepancies that are observed in the comparison suggest a trend of higher predicted values for the mid-frequency and higher frequency ranges. However, it is worth noting that the predicted results do fall within the general frequency range. Even more so, the A-weighted overall sound pressure level that is calculated for the prediction only appears to have a difference around 2-3 dBA compared to the measured data.

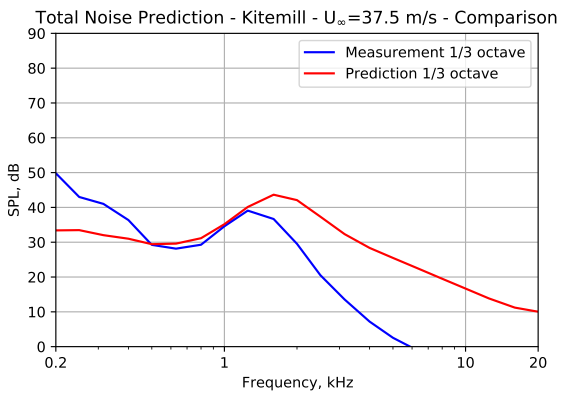

Figure 4.19: Measured data versus predicted data of *Kitemill* for U_∞=37.5 m/s.

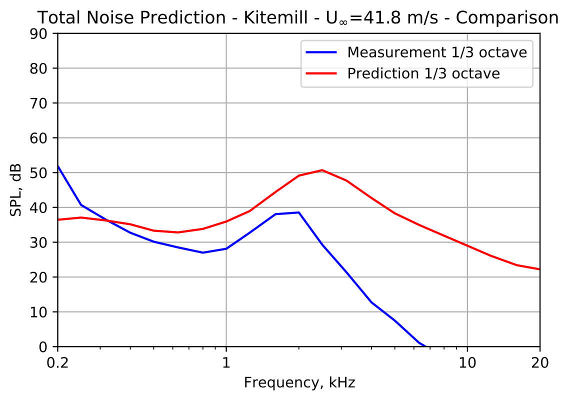

Figure 4.20: Measured data versus predicted data of *Kitemill* for U_∞=41.8 m/s.

Besides the sound pressure level spectra, the directivity plot is predicted for the KM1 of *Kitemill*. It is important to note that the predicted directivity plot only takes the turbulent boundary layer trailing edge noise into account. As one can observe from Figure 4.17 and Figure 4.18, the noise contribution of the turbulent boundary layer trailing edge noise is relatively low. The predicted directivity plots are shown in Figure 4.21. In Figure 4.21 three ranges of frequencies are presented for both the low velocity and high velocity cases as described before for the KM1. From Figure 4.21a dipoles can be seen for both cases. These dipoles deform more towards higher frequency ranges. Figure 4.21b shows that the deformation of the dipole starts sooner for the high velocity case, for which the overall sound pressure levels remain higher for the left-hand side and decrease for the right-hand side. The same phenomena can be observed at the highest frequency range for the low velocity case in Figure 4.21c. In that same plot in Figure 4.21c, the high velocity case shows that the directivity starts leaning even more towards the left-hand side. Overall, from the directivity plots, it can be seen that for the lower frequency ranges and therefore the Strouhal number ranges, dipoles can be expected. With the frequency ranges increasing, the directivity starts to direct more towards the left-hand side, which is towards the leading edge of the airfoil. When the chord is larger compared to the wavelength of the sound, the sound waves interact with the surface in a way that they interact more with the surface. This interaction causes the sound to scatter and results in a cardioid figure for the directivity. This means that the presence of the surface for this case results in the directivity pattern leaning more in the direction of the surface.

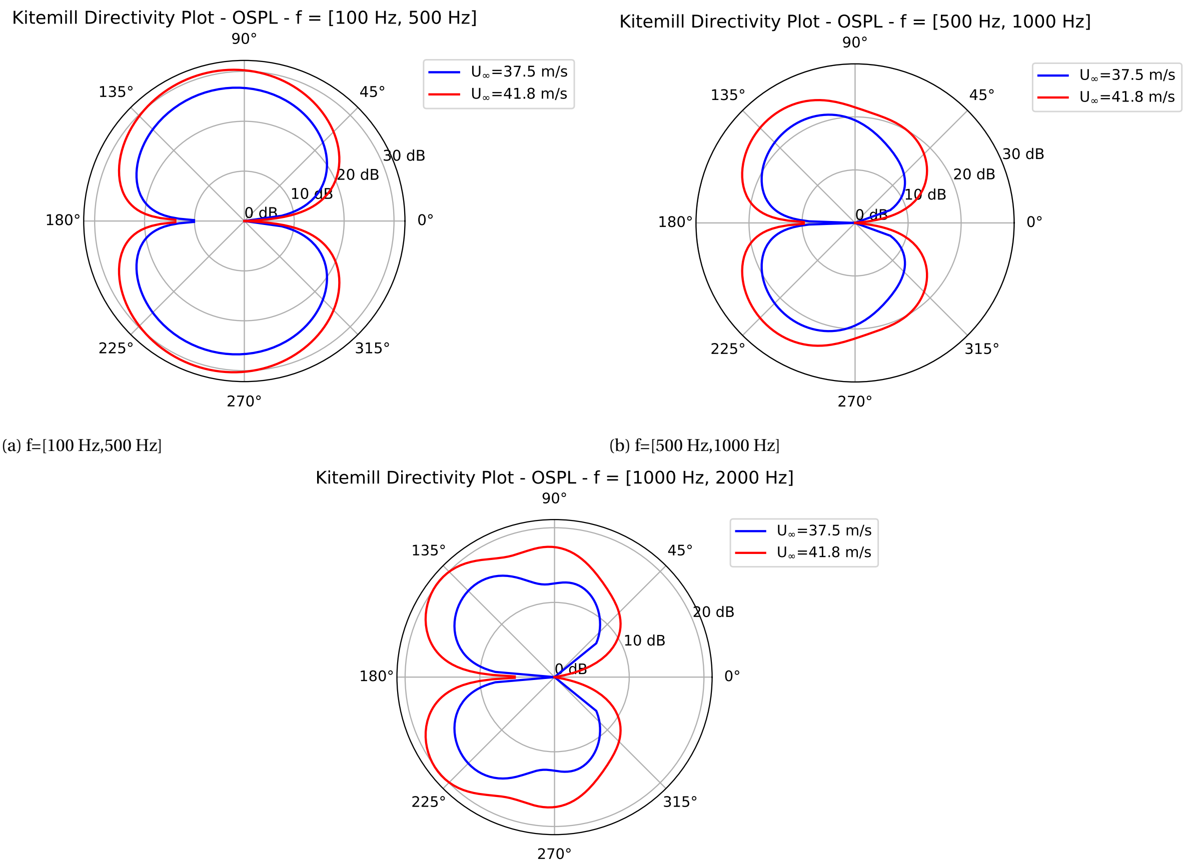

(a) f=[100 Hz,500 Hz]

(b) f=[500 Hz,1000 Hz]

(c) f=[1000 Hz,2000 Hz]

Figure 4.21: Predicted directivity plots for the KM1.

4.2.2. KITEPOWER

Obtaining the data of the boundary layer parameters of *Kitepower* is a little less straight forward, due to the complex shape of the airfoil of the rib of the kite. Even more so, as no CFD analysis will be conducted, some simplifications are required to be able to perform the analysis and obtain the data through XFOIL. The steps that are taken for this simplification are visualized in Figure 4.22. From this figure, it can be seen that the first step taken is to obtain the profile of the top of the airfoil. This is then mirrored, which will then represent the bottom of the airfoil. The simplified airfoil is thus a symmetric airfoil based on the profile of the top of the original airfoil. This will result in appropriate estimations of the boundary layer for the suction side, but not for the pressure side. For this reason, the boundary layers presented in Figure 2.29 in Subsection 2.3.5 are analyzed from which an estimation will follow for a relation between the boundary layers of the pressure and suction side of the airfoil of the kite. It can be observed that for higher angles of attack, as well as for higher Reynolds numbers, the boundary layer on the pressure side gets thinner, as well as a reduction of the size of the recirculation zone, which moves up the location of the reattachment of the boundary layer.

Although, another option to simplify the airfoil could have been to "round off" the pressure side of the airfoil, it would, nonetheless, result in inaccurate boundary layer parameters at the trailing edge, as the recirculation zone would mostly disappear. Therefore, the chosen method aims to get the most accurate boundary layer parameters for the suction side, which are then used to obtain the parameters on the pressure side by applying the relationship between the boundary layer thickness on both sides of the airfoil.

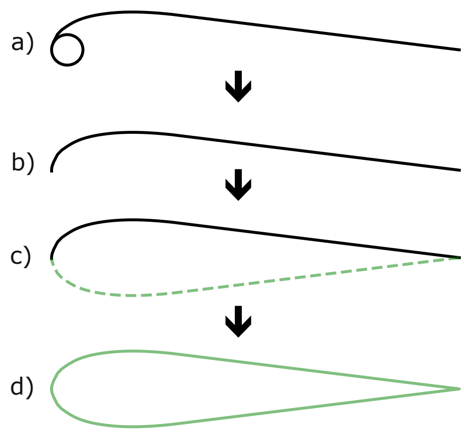

Figure 4.22: Visualization of the simplification of the *Kitepower* airfoil for the boundary layer analysis.

The input parameters that are used for the analysis are obtained from the flight data at t=186 s and t=193 s. The dimensions of the V9.60 kite are used, as well as an angle of attack of 8º for both cases.

The results of the noise prediction for the V9.60 kite are shown in Figure 4.23 and Figure 4.24.

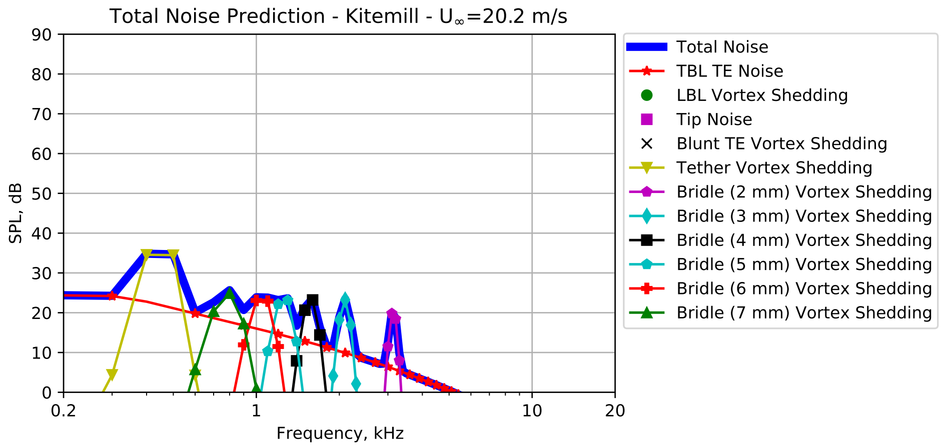

Figure 4.23: Sound pressure level spectrum for $U_\infty = 20.2$ m/s of the V9.60.

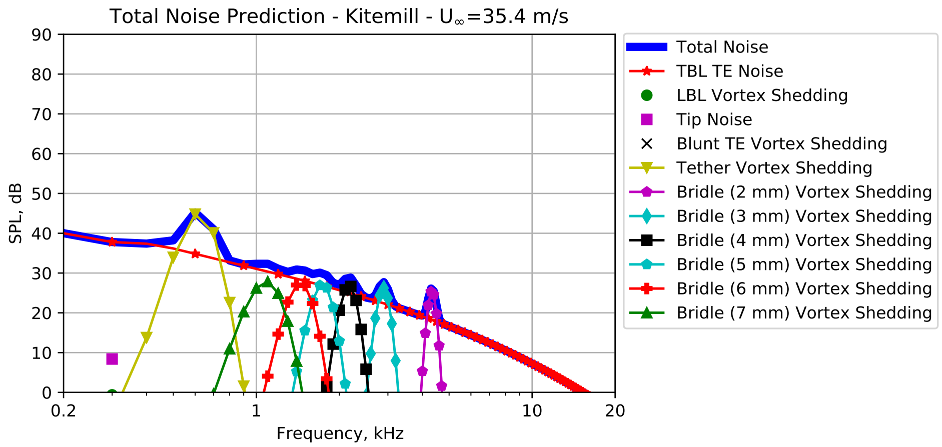

Figure 4.24: Sound pressure level spectrum for $U_\infty = 35.4$ m/s of the V9.60.

The experimental results, presented in Subsection 4.1.2, showed a broadband spectrum for both t=186 s and t=193 s. For t=186 s, two additional bumps can be distinguished around 300 Hz and 1000 Hz. For t=193 s, a similar phenomenon can be observed, although the bumps have shifted slightly to higher frequencies and having their peaks at higher sound pressure levels. The predicted results on the other hand show a broadband spectrum as well for both cases, with some peaks as well. One peak is caused by the vortex shedding of the tether, which is centered around 400 Hz for the lower velocity case and 600 Hz for the higher velocity case. The other peaks are caused by the vortex shedding of the bridle lines and appear in the frequency range between 800 Hz and 4000 Hz, while having much lower sound pressure levels compared to the tether vortex shedding.

Also for this prediction, it should be noted that the Doppler effect was not taken into account, as also for these cases the Mach numbers are low, which means the Doppler effect remains limited.

In Figure 4.25 and Figure 4.26 the predicted spectra are plotted against the measured data. The comparison between the predicted and measured results reveals some differences in the acoustic characteristics. The predictions tend to slightly shift the peak frequency of the bump at the lower frequency range towards higher values compared to the measured data. However, it is worth noting that the broadband component of the predicted spectrum, particularly for the lower velocity case, exhibits a close match within the frequency range of 1000 Hz to 4000 Hz.

In the case of the higher velocity scenario, the predicted spectrum shows higher sound pressure levels in both the mid-frequency range and high-frequency range compared to the measured data. This discrepancy suggests that the prediction might be overestimating the noise levels in these frequency regions for the given conditions.

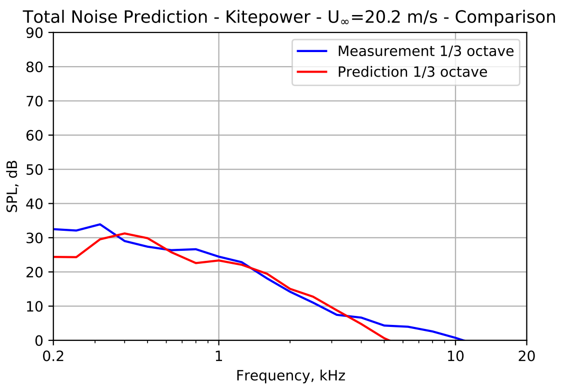

Figure 4.25: Measured data versus predicted data of *Kitepower* for U_{∞}=20.2 m/s.

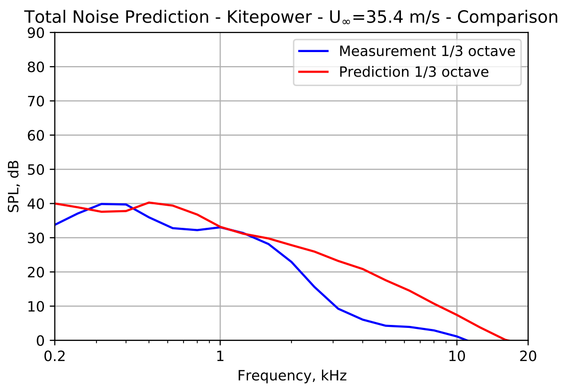

Figure 4.26: Measured data versus predicted data of *Kitepower* for U_{∞}=35.4 m/s.

The predicted directivity plots of the V9.60 kite of *Kitepower* have been obtained as well and are presented in Figure 4.27. Again, one should keep in mind that the predicted directivity plot only takes the turbulent boundary layer trailing edge noise into account. For all frequency ranges, the plots show patterns similar to dipoles, although the higher frequency ranges contain more discrepancies. As could already be seen in Figure 4.23 and Figure 4.24, the turbulent boundary layer trailing edge noise is significantly lower for the low velocity case compared to the high velocity case. The same can be observed when looking at the directivity plots in Figure 4.27. Overall, it can be seen that for all frequencies dipoles can be expected with slight increase in deformations of this patterns for higher frequencies, especially on the left-hand side of the directivity plot. These irregularities can occur due to various factors, like airflow disturbances for example, which can affect the way sound waves propagate and interact with the surrounding environment, leading to deviations from the smooth dipole or cardioid pattern. However, the main take away from these plots is that the directivity plots show a pattern that can be expected for the loading the kites impose on the air.

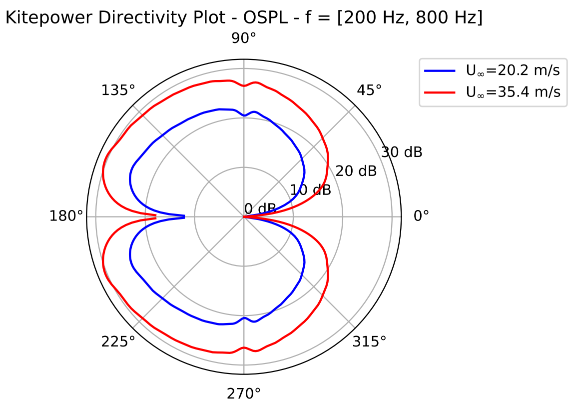

(a) f=[200 Hz,800 Hz]

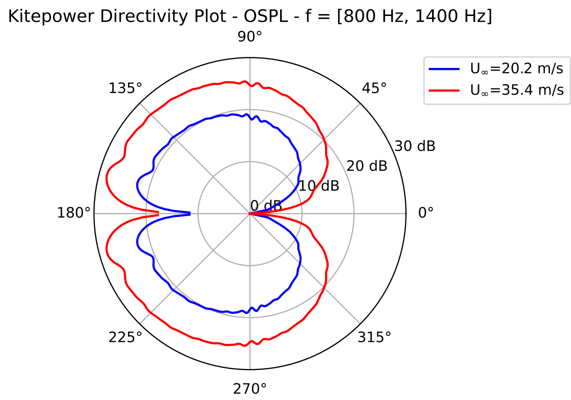

(b) f=[800 Hz,1400 Hz]

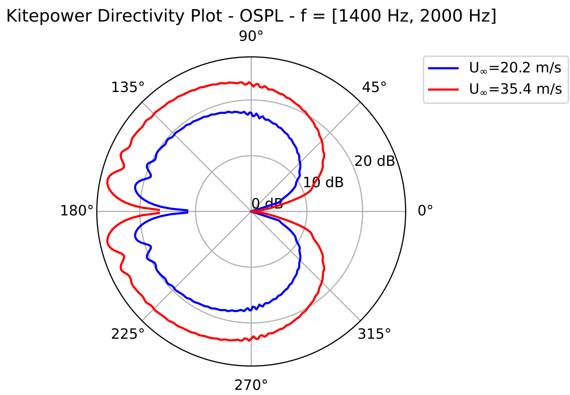

(c) f=[1400 Hz,2000 Hz]

Figure 4.27: Predicted directivity plots for the V9.60.

4.3. KEY FINDINGS

This section presents the key findings of the study conducted to identify the noise sources in airborne wind energy systems making use of either a fixed-wing kite or a LEI, soft kite. The key findings presented in this section shed light on the noise profiles and highlight notable observations from both the analytical simulations and experimental measurements. The subsequent subsections will go into the specific findings and results obtained from the analytical simulations and experimental measurements conducted on the *Kitemill* and *Kitepower* systems.

4.3.1. KITEMILL

The analysis of the airborne wind energy system of *Kitemill* gave important insights into the noise characteristics and sources associated with this type of system and operation. The key findings from the experimental data and analytical predictions are summarized below:

- **Flight Path Analysis:** The spectrogram of the experimental data during the production phase exhibited a repetitive pattern corresponding to the flight path of the kite.
- **Peak Frequencies:** The noise analysis of the experimental data identified prominent peaks around 1500 Hz and 2000 Hz. Notably, the higher frequency peak was observed when the kite was flying at higher velocities.
- **Effect of Velocity and Distance:** The noise spectra of the experimental data revealed that as the kite moved closer to the microphone, the sound intensity increased. Additionally, higher velocities resulted in a shift of the peak frequency towards higher frequencies.
- **Scaled Data:** The scaled sound pressure levels showed that the emitted noise scaled with the inverse square law with respect to the distance. The tonal peak is observed around $St_c = 15$.

- **Analytical Predictions:** The analytical models used in the study indicated two main sources of noise: laminar boundary layer vortex shedding and tether vortex shedding. These sources contributed to a peak centered around 1700 Hz and 2200 Hz in the predicted spectra for the low and high velocity case, respectively.

- **Frequency Range Prediction:** While the analytical models provided reasonable predictions, they exhibited certain limitations. The lower frequency range was underestimated, likely due to the background noise not being included in the prediction. In the mid-frequency range, the prediction showed increased sound pressure levels, and the higher frequency range tended to be overestimated as well.

- **Directivity Analysis:** The directivity prediction for the turbulent boundary layer trailing edge noise demonstrated the presence of dipoles. These dipoles exhibited slight deformations at higher frequency ranges, particularly at the top and bottom of the dipoles.

These key findings shed light on the noise characteristics of *Kitemill*'s airborne wind energy system, highlighting the influence of flight parameters and identifying the dominant noise sources. The discrepancies between experimental data and analytical predictions provide valuable insights for further refinement of the models and possible noise reduction strategies.

4.3.2. KITEPOWER

The analysis of the *Kitepower* airborne wind energy system provided significant findings on its noise characteristics and sources associated with this type of system and operation. These findings, derived from both experimental data and analytical predictions are outlined below:

- **Flight Path Analysis:** The spectrogram of the experimental data during the flight of the figure-of-eight pattern revealed a repetitive pattern corresponding to each loop flown by the kite.

- **Peak Frequencies:** The noise analysis of the experimental data showed peaks in the sound pressure level around 300-400 Hz and 1000-2000 Hz, with higher frequencies occurring during periods of increased kite velocities.

- **Kite Deformations:** Video footage captured during the test flight showcased phenomena such as trailing edge flutter and seam-rippling, which are likely to contribute to enhanced sound pressure levels, particularly at lower frequencies at which the phenomena occur, as also discussed in Subsection 2.3.5. However, like mentioned before, the kite is still in the research and development phase, which means it is anticipated to address and eliminate these deformations in the final product, ensuring their absence in the commercialized version.

- **Effect of Velocity:** The experimental data's noise spectra highlighted a relationship between the spectra and the kite velocity. Higher velocities corresponded to slightly higher sound intensities, but mainly caused noise emitted at higher frequency ranges.

- **Scaled Data:** The scaled sound pressure levels showed that the emitted noise scaled with the square law with respect to the distance and best scaled with $n = 4.5$ with respect to the velocity of the kite, which aligns with the scaling for broadband trailing edge noise.

- **Analytical Predictions:** The analytical models provided two primary types of noise sources: turbulent boundary layer trailing edge noise and vortex shedding from the tether and bridle lines. The turbulent boundary layer trailing edge noise contributed to the broadband component of the spectrum, while the tether and bridle lines contributed to some peaks over a range of frequencies, with the tether, leading to the higher intensity peak at the lowest frequency.

- **Frequency Range Prediction:** The analytical predictions slightly underestimated the lower frequency range for the low velocity case. The mid-frequency range showed closer agreement, although with slightly higher sound pressure levels in the prediction for the higher velocity case. The higher frequency range tended to be overestimated for the higher velocity case, while the low velocity case shows a close match. Differences between the prediction and the measurements could be attributed to factors such as trailing edge flutter, seam-rippling, and background noise, which were not accounted for in the prediction.

– **Directivity Analysis:** The directivity prediction for the turbulent boundary layer trailing edge revealed dipoles with slight deformations, particularly on the left-hand side, as the frequency range increased.

These findings provide valuable insights into the noise characteristics and sources associated with the *Kitepower* airborne wind energy system. They contribute to a better understanding of the system's noise generation mechanisms and can aid in future noise reduction strategies.

4.4. PREVIOUS STUDY COMPARISON

In Subsection 2.3.1, the pioneering study conducted by Szücs [30] was discussed on the acoustics of the airborne wind energy system developed by *Kitepower*. Szücs' study provided valuable insights into the noise characteristics of the system, although with some notable differences compared to the current study.

One significant difference between the two measurement campaigns is the distance from the generator at which the measurements were taken. Szücs' study focused on distances up to 200 meters, while the current study extended focus on the distance of approximately 650 meters from the winch/generator. This extended distance allows for a full exclusion of the generator noise and full focus on the noise characteristics of the airborne components of the system.

Another noteworthy distinction is the use of a windscreen in the current study, which was not employed in Szücs' study. The windscreen helped to isolate and analyze the noise generated by the system rather than by the wind, which became a dominant factor in Szücs' measurements. Additionally, the equipment used in the two campaigns differed. Szücs utilized the Philips SBCMD650 dynamic microphone designed for general recording purposes, while this study made use of the B&K 2250 microphone, which offers high accuracy and low self-noise for precise sound measurements, due to its built-in preamplifier.

Szücs' measurements were obtained from the 20 kW system of *Kitepower*, whereas our study focused on the larger 100 kW system. This difference in system could lead to some variations in the noise generation and propagation that should be considered as well when looking at both studies.

Analyzing the specific measurements of Szücs at 100 meters, it was observed that higher sound pressure levels were centered around 500 Hz, which were identified as noise generated by the kite. At a distance of 10 meters from the generator, tether noise ranging from 500 Hz to 1000 Hz was identified. Comparing these findings with the current study, a more detailed spectrogram is obtained that revealed a noise pattern extending up to approximately 2000 Hz. Despite the wind remaining a dominant factor, the current study provides valuable insights into the lower frequency range as well. Also, it is found that indeed the kite is the dominant factor in the noise emission at a large distance. However, the current study also shows the presence of noise from the tether and bridle lines at a large distance, although less dominant, especially for the thinnest bridle lines, but not completely unnoticeable in the spectra.

Overall, both studies have contributed significantly to the understanding of airborne wind energy system noise. By building upon the pioneering study conducted by Szücs, the current study expands the knowledge base with an extended measurement range, better controlled environmental conditions, and more advanced measurement equipment.

5

Discussion

5.1. Implications and Recommendations for AWE

The analysis of the airborne wind energy systems of *Kitemill* and *Kitepower* has resulted in important insights into the noise characteristics and sources associated with these systems. Futhermore, it provides a foundation for possible noise reduction strategies and guiding future research.

The key findings as discussed in Section 4.3 have notable implications for the field of airborne wind energy, providing valuable insights into the noise characteristics and sources associated with the different airborne wind energy systems. The implications and recommendations of these findings are discussed below:

- **Velocity Control:** The relationship between kite velocity and noise intensity provides insights into noise control measures. Implementing velocity control mechanisms, such as adjusting the kite's flight speed, can help manage noise emissions during different operational conditions. So it appears that lower velocities will reduce the noise produced by a fixed-wing kite, with a similar phenomenon applying to soft kites, although some extra factors have to be taken into account. As, for the soft kites, one should note that the emitted noise is not solely linked to the velocity, as the relationship is also likely to be linked to the position of the kite and the intensity of phenomena such as trailing flutter and seam-rippling.
- **Noise Reduction Strategies:** The identification of dominant noise sources, such as laminar boundary layer vortex shedding (fixed-wing kite), turbulent boundary layer trailing edge noise (soft kite), tether vortex shedding, trailing edge flutter and seam-rippling (soft kite), allows for targeted noise reduction strategies in airborne wind energy systems. By understanding the dominant noise-generating mechanisms, approaches can be explored to mitigate noise emissions. For example, modifying the tether from a braided tether to a helical strake braiding (see Figure 5.2), which disrupts the creation of the vortices and modulates the local Strouhal number [101]. Also, tripping the boundary layer from laminar to turbulent could aid in the reduction of the noise that is caused for the fixed-wing kite, due to the laminar boundary layer vortex shedding. Tripping the boundary layer could for example be obtained by making use of so called 'turbulators' or zig zag tape (see Figure 5.1). For the soft kite, kite deformations, such as trailing edge flutter and seam-rippling, were observed to seemingly contribute to increased sound pressure levels. Developing measures to mitigate these deformations, such as adding reinforced stitching or panels in certain critical areas.
- **Regulatory Compliance:** Noise emissions are a crucial consideration in the deployment of airborne wind energy systems, particularly in proximity to residential areas or environmentally sensitive regions. The findings of this study contribute to a better understanding of noise characteristics, enabling developers to assess and ensure compliance with (future) regulatory requirements and noise standards.

- **Environmental Impact:** Noise pollution can have adverse effects on local wildlife and ecosystems. By reducing the noise emissions of airborne wind energy systems, the study's findings support efforts to minimize the environmental impact of renewable energy technologies.

By implementing these recommendations and considering the implications of the research findings, steps can be made in minimizing the noise impact of airborne wind energy systems.

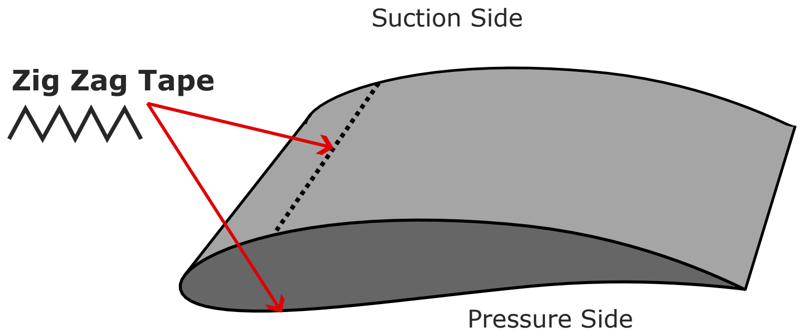

Figure 5.1: Illustration of zig zag tape placed on a wing.

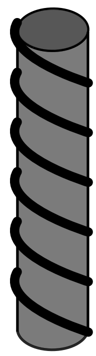

Figure 5.2: Illustration of helical strake braid. The cylinder represents the standard braided tether, while the helical strake goes around it.

5.2. Limitations and Future Research

The present study on airborne wind energy systems and their noise characteristics has provided valuable insights on aspects of aeroacoustics of airborne wind energy systems. However, several limitations were encountered, and opportunities for future research and investigation have been identified.

One of the primary limitations of the current study lies in the analytical methods employed. While analytical simulations have provided valuable insights, they were initially developed for rigid wings in wind tunnels and may not fully capture the specific maneuvers and phenomena associated with both fixed-wing and soft kites. Notably, characteristics unique to soft kites, such as trailing edge flutter and seam-rippling, were not fully accounted for in the models. Therefore, future research should focus on refining analytical methods to accurately represent the complexities of airborne wind energy systems, particularly those involving soft kites.

Even more so, the input of the analytical model for the case of *Kitepower* relied on a rough estimation, due to the unavailability of CFD results for the boundary layer parameters. In future research, more reliable boundary layer data will have to be obtained and used in the analytical model to obtain better accuracy in the predicted results.

Another limitation concerns the data collection and analysis. The study relied on a limited number of measurements from both *Kitepower* and *Kitemill*. To obtain a comprehensive understanding of noise characteristics, future research should include multiple measurements for different flight conditions and distances from the kite/winch. By obtaining a broader range of data, including directivity measurements and/or using microphone arrays that can find exact locations of radiated noise, researchers can gain insights into dominant noise sources and their locations during different flight phases and conditions.

The availability of resources, specifically related to the acoustics of airborne wind energy systems, posed a significant challenge during the research process. Conducting thorough investigations often required delving into other fields where similar features were found as to the specific component of the airborne wind energy system. Future research efforts should aim to contribute to a broader understanding and knowledge of the acoustics of airborne wind energy systems, thereby establishing a solid foundation for this field of study.

Looking ahead, there are several areas that call for further research. One direction is the implementation of suggested changes or improvements to assess their impact on noise reduction. This includes exploring modifications to the tether, tripping the laminar boundary layer to turbulent of fixed-wing kites, and reinforcing critical areas of soft kites to mitigate trailing edge flutter and seam-rippling.

In addition, the effects of the recirculation zone on the radiated noise of LEI soft kites, as well as the interaction with the trailing edge and scattered noise require further exploration. Investigating the precise timing and characteristics of these phenomena in relation to the radiated noise will provide valuable insights for noise reduction strategies.

As airborne wind energy systems continue to evolve, with companies increasingly compelling to examine the influence of system size on acoustic characteristics. Future research should investigate the potential differences in the acoustic spectra resulting from varying system sizes to ensure a comprehensive understanding of noise emissions.

In conclusion, while the current study has made significant contributions to the field of airborne wind energy and noise analysis, it is essential to acknowledge its limitations and pave the way for future research. By refining analytical methods, expanding data collection, exploring noise reduction strategies, and addressing unresolved questions, researchers can advance the understanding of airborne wind energy system acoustics and develop effective noise mitigation techniques.

6 Conclusion

The objective of this study was to investigate the noise characteristics and sources associated with airborne wind energy systems, specifically those utilizing fixed-wing kites and soft, LEI kites. The hypothesis of this thesis can be assessed, which proposed that:

> The noise generated by the tether will significantly contribute to the overall noise emissions in both the *Kitepower* and *Kitemill* systems. Additionally, the *Kitepower* system is expected to exhibit turbulent boundary layer noise, while the *Kitemill* system is expected to primarily produce laminar vortex shedding noise.

Through a combination of analytical simulations and experimental measurements, relevant insights have been obtained, providing a foundation for noise reduction strategies and future research in the field of airborne wind energy.

The analysis of *Kitemill*'s airborne wind energy system revealed important findings regarding the noise emitted during its operation. The spectrogram analysis of experimental data showed a repetitive pattern corresponding to the flight path of the kite, highlighting the influence of flight parameters on noise production. Prominent peaks in the sound pressure level were identified around 1500 Hz and 2000 Hz, with higher frequencies observed at higher kite velocities. The noise spectra revealed that sound intensity increased as the kite moved closer to the microphone. The analytical models indicated laminar boundary layer vortex shedding and tether vortex shedding as the main sources of noise, causing peaks in the predicted spectra.

Similarly, the analysis of *Kitepower*'s airborne wind energy system provided significant findings. The spectrogram analysis of experimental data showed a repetitive pattern corresponding to the figure-of-eight flight pattern. Peaks in the sound pressure level spectra were observed around 300-400 Hz and 1000-2000 Hz, with higher frequencies occurring during periods of increased kite velocities. Video footage captured deformations such as trailing edge flutter, which was found likely to contribute to increased sound pressure levels, particularly at lower frequencies. However, one should keep in mind that this type of deformation is expected to be eliminated these in the final product, ensuring their absence in the commercialized version. The analytical models identified turbulent boundary layer trailing edge noise and vortex shedding from the tether and bridle lines as the primary noise sources.

The analysis of both the *Kitemill* and *Kitepower* AWE systems supports the hypothesis that the noise generated by the tether significantly contributes to the noise emissions. Additionally, the findings confirm the expected noise characteristics, with the *Kitepower* system exhibiting prominent turbulent boundary layer trailing edge noise and the *Kitemill* system primarily producing laminar vortex shedding noise.

These findings have important implications for airborne wind energy systems. The identification of dominant noise sources enables targeted noise reduction strategies. Velocity control mechanisms can be implemented to manage noise emissions during different operational conditions, but also measures such as modifying the tether could aid to a noise reduction. For fixed-wing kites, one could look into the possibility of tripping the boundary layer from laminar to turbulent to alter and perhaps even lower the produced noise. For soft kites, measures such as addressing kite deformations can contribute to noise reduction. The understanding of noise characteristics also supports compliance with (future) regulatory requirements and aids in minimizing the environmental impact of these technologies.

While this study has provided valuable insights, there are limitations that should be addressed in future research. The analytical methods used may not fully capture the maneuvers and characteristic phenomena of the kites, particularly in the case of soft kites. Additional measurements under various flight conditions and distances from the kite are needed to obtain a comprehensive understanding of the noise characteristics. Future research should also explore the effects of recirculation zones and the interaction with the trailing edge and the radiated noise for soft kites. Furthermore, future research efforts should aim to contribute to a broader understanding and knowledge of the acoustics of airborne wind energy systems, and thereby establishing a solid foundation for this field of study.

To conclude, this study has contributed to the understanding of noise characteristics and sources in airborne wind energy systems. The insights gained can guide noise reduction strategies, aid in (future) regulatory compliance, and support the development of environmentally friendly renewable energy technologies. Continued research and collaboration among academia, industry, and regulatory bodies are crucial to further advance our knowledge in this field and ensure the sustainable growth of airborne wind energy.

A

SOFT LEI KITE CHARACTERISTICS

A.1. FLOW ON 2D FLEXIBLE SAILS

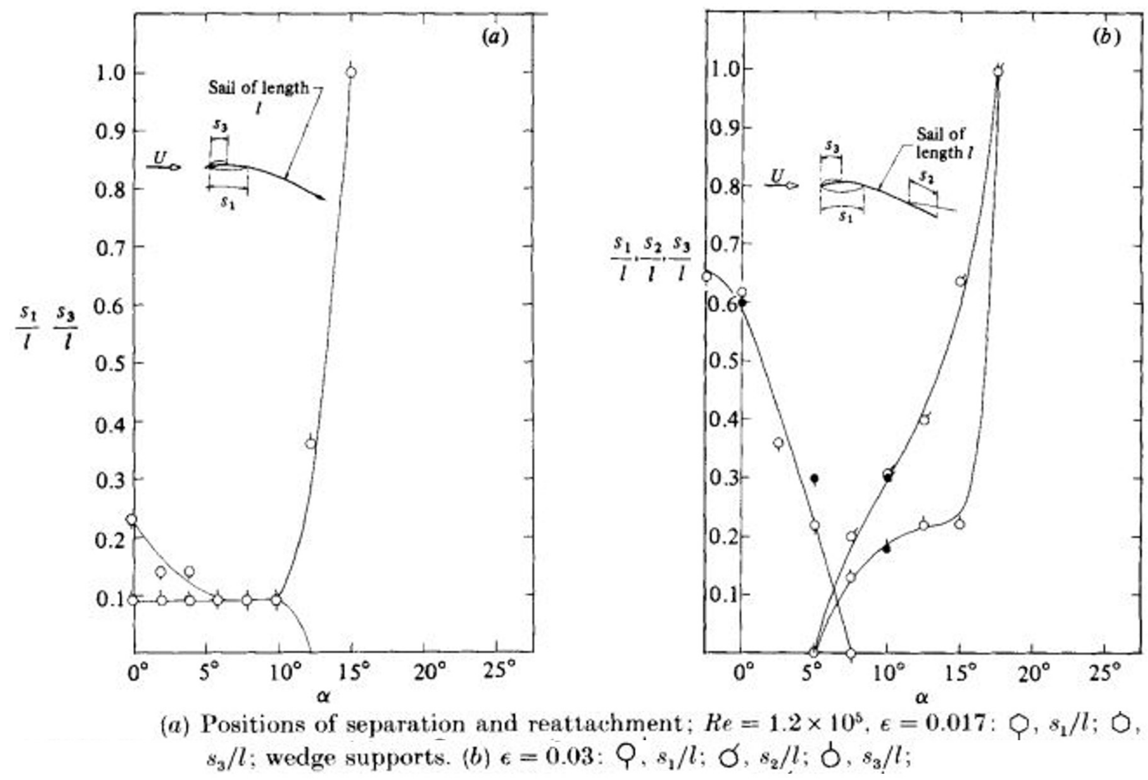

Figure A.1: Separation and reattachment positions for a 2D membrane wing. ϵ represents the excess-length ratio ($\frac{l-c}{c}$), with l the length of the membrane and c the distance between the LE and TE. Obtained from Newman & Low [45].

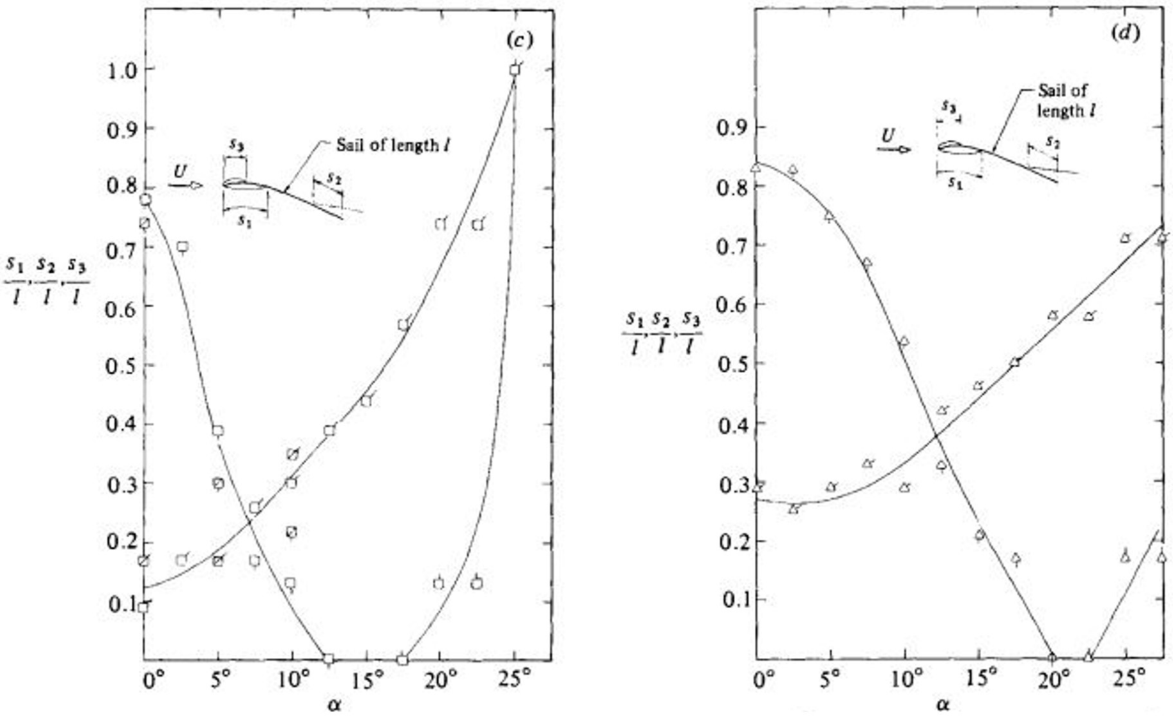

(c) $\epsilon = 0.05$: ◻, s_1/l; ◻, s_2/l; ◻, s_3/l; open symbols: $Re = 1.2 \times 10^5$; $Re = 0.7 \times 10^5$. (d) $\epsilon = 0.10$: △, s_1/l; △, s_2/l; △, s_3/l.

Figure A.1: Separation and reattachment positions for a 2D membrane wing. ϵ represents the excess-length ratio ($\frac{l-c}{c}$), with l the length of the membrane and c the distance between the LE and TE. Obtained from Newman & Low [45]. (continued)

B

Boundary Layer Parameters

B.1. Boundary Layer Thickness

The boundary layer thickness is defined as the thickness for which the velocity profile reaches a velocity that is equal to 99% of the freestream velocity [102]. The properties of the laminar boundary layer are found from the flat-plate boundary layer theory, while the properties of the turbulent boundary layer are obtained by making use of the one-seventh-power law [103, 104]. The seventh-root profile with the boundary layer properties is plotted in Figure B.1. The boundary layer thickness of a laminar and turbulent boundary layer can be expressed in terms of the Reynolds number Re_x:

$$\mathrm{Re}_x = \frac{U_\infty x}{\nu}. \tag{B.1}$$

The formulation of the boundary layer thickness is then as follows:

$$\delta_{LBL} = 4.91\frac{x}{\left(\mathrm{Re}_x\right)^{1/2}}, \tag{B.2}$$

$$\delta_{TBL} = 0.16\frac{x}{\left(\mathrm{Re}_x\right)^{1/7}}, \tag{B.3}$$

where the subscript *LBL* indicates the laminar boundary layer and *TBL* the turbulent boundary layer

B.2. Displacement Thickness

The displacement thickness δ^* of the boundary layer is equal to the distance the surface would have to move in the y-direction to reduce the flow passing by a volume that is equivalent to the real effect of the boundary layer [105]. Just as the boundary layer thickness, the displacement thickness is found by making use of the flat-plate theory and the seventh-root velocity profile [103] for the laminar and turbulent boundary layer, respectively. The displacement thickness is therefore expressed as:

$$\delta^*_{LBL} = \frac{1.72x}{\left(\mathrm{Re}_x\right)^{1/2}} = 0.35\delta_{LBL}, \tag{B.4}$$

$$\delta^*_{TBL} = \frac{0.020x}{\left(\mathrm{Re}_x\right)^{1/7}} = 0.125\delta_{TBL}. \tag{B.5}$$

B.3. Momentum Loss Thickness

The momentum thickness or momentum loss thickness of a boundary layer is defined as the distance that, when multiplied by the square of the free stream velocity, equals the integral of the momentum defect [105].

In other words, the momentum loss thickness represents a measure of the total plate drag. The equation of the momentum thickness θ is written as:

$$\theta_{LBL} = \int_0^{\delta} \frac{u}{U}\left(1 - \frac{u}{U}\right) dy = \frac{0.664}{\left(\mathrm{Re}_x\right)^{1/2}} = 0.135\delta_{LBL}. \tag{B.6}$$

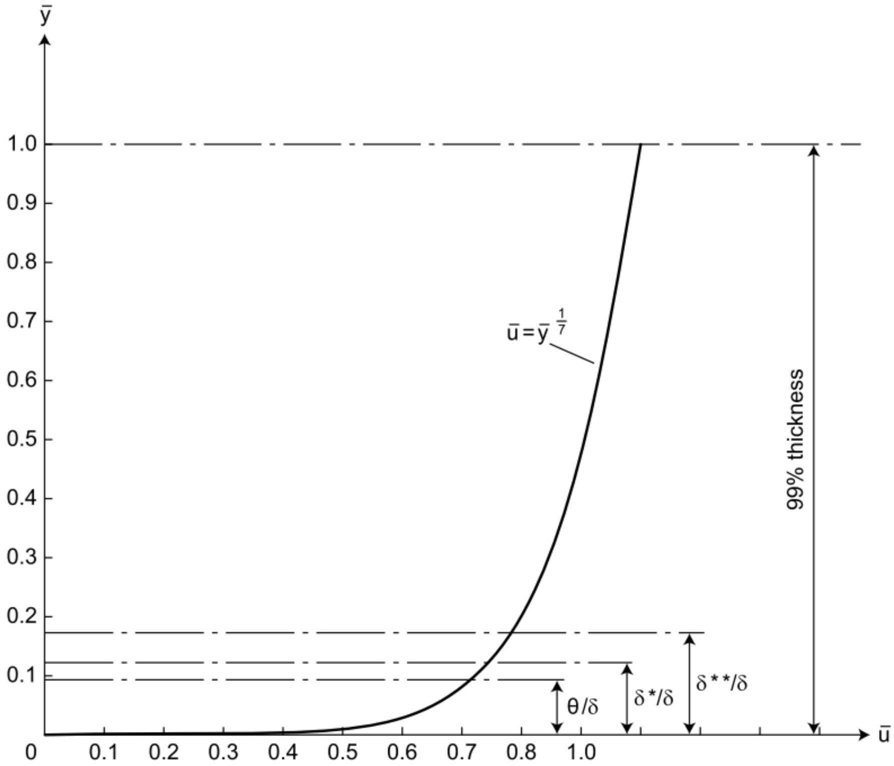

Figure B.1: Turbulent velocity profile. Obtained from Houghton et al. [103].

The terms used in Equation B.6 represent the velocity profile u, external velocity U and the boundary layer thickness δ, which are also shown in Figure B.2. However, this theory holds for a laminar flow over a flat-plate. For turbulent flow, the momentum thickness gets evaluated as:

$$\theta_{TBL} \approx \int_0^{\delta} \left(\frac{y}{\delta}\right)^{1/7} \left[1 - \left(\frac{y}{\delta}\right)^{1/7}\right] dy = 0.1\delta_{TBL}. \tag{B.7}$$

B.4. SHAPE FACTOR

The boundary layer shape factor equals the ratio of displacement thickness to the momentum thickness (see Equation B.8). The shape factor represents the change in the overall mean velocity profile. The shape factor is known to be around 2.4 for a turbulent flow and 3.5 for a laminar flow [106].

$$H = \frac{\delta^*}{\theta} \tag{B.8}$$

B.5. SKIN FRICTION COEFFICIENT

The skin friction coefficient is an important characteristic associated with the boundary layer. The skin friction coefficient is defined as a dimensionless quantity from the wall shear stress [107], which is formulated as:

$$c_f = \frac{\tau_w}{\frac{1}{2}\rho_e U_e^2}. \tag{B.9}$$

Once again, this property of the turbulent boundary layer can be expressed by making use of the seventh-root velocity profile [108], which is defined as:

$$c_{f,LBL} = \frac{0.664}{\left(\mathrm{Re}_x\right)^{1/2}} = 0.135\delta_{LBL}, \tag{B.10}$$

$$c_{f,TBL} = \frac{0.027}{\left(\mathrm{Re}_x\right)^{1/7}} = 0.169\delta_{TBL}. \tag{B.11}$$

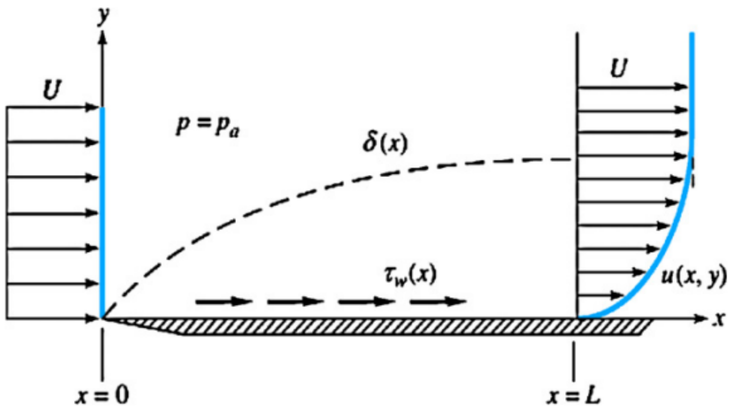

Figure B.2: Growth of a boundary layer on a flat plate. Obtained from Hafeez and Ndikilar [105].

C

Validation Analytical Methods

C.1. Amiet Model

NACA0018						
U_0, m/s	20		20		40	
α, °	0		7.8		7.8	
Suction Side (SS) or Pressure Side (PS)	SS	PS	SS	PS	SS	PS
δ^*/c	0.0100117		0.0233653	0.0051368	0.0191209	0.0043717
θ, m	0.0053523		0.0090043	0.0031823	0.0078066	0.0027611
C_f	0.0014389		0.0003439	0.0027199	0.0003744	0.0023726
dP/dx, Pa/m	458	461	212	374	1054	1649
H	1.87		2.59	1.61	2.45	1.58

Table C.1: Boundary layer parameters for the cases as discussed in the paper of Teruna et al. obtained through XFOIL [76] at $x/c = 0.98$.

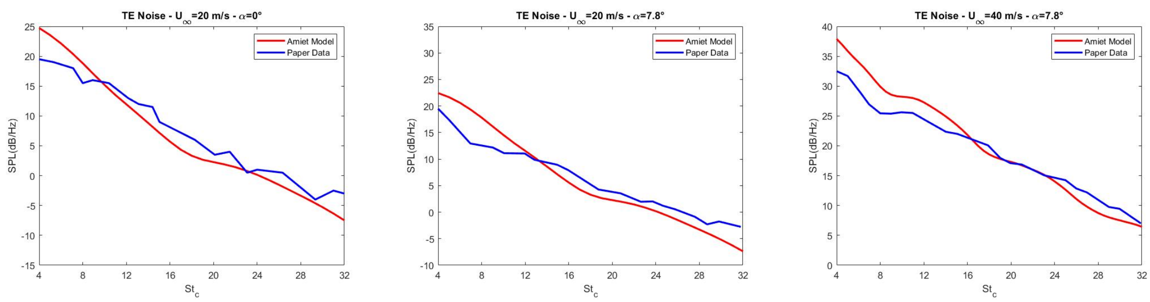

(a) $V_\infty = 20$ m/s, AoA=0°

(b) $V_\infty = 20$ m/s, AoA=7.8°

(c) $V_\infty = 40$ m/s, AoA=7.8°

Figure C.1: Trailing edge noise model comparison of Amiet model versus results of the paper of Teruna et al. [78] at observer location $x/c = -0.68$, $y/c = 4.95$.

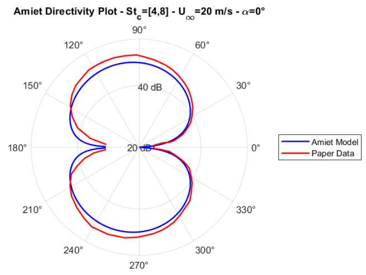

(a) V_∞ = 20 m/s, AoA=0°, St=[4,8]

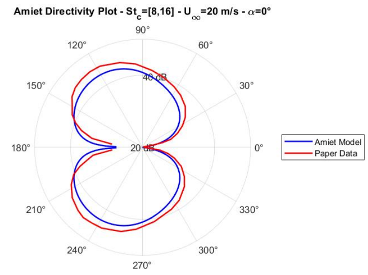

(b) V_∞ = 20 m/s, AoA=0°, St=[8,16]

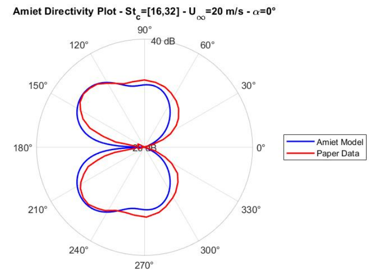

(c) V_∞ = 20 m/s, AoA=0°, St=[16,32]

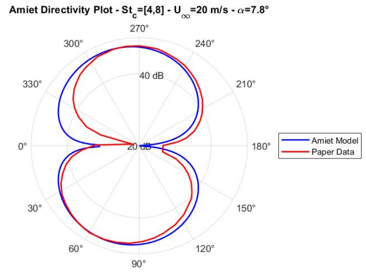

(d) V_∞ = 20 m/s, AoA=7.8°, St=[4,8]

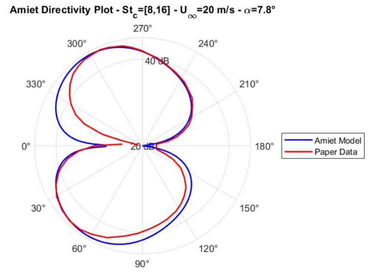

(e) V_∞ = 20 m/s, AoA=7.8°, St=[8,16]

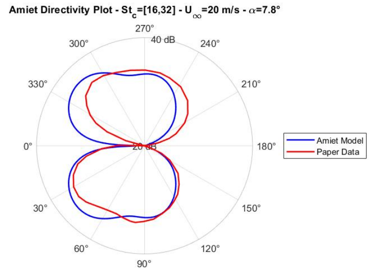

(f) V_∞ = 20 m/s, AoA=7.8°, St=[16,32]

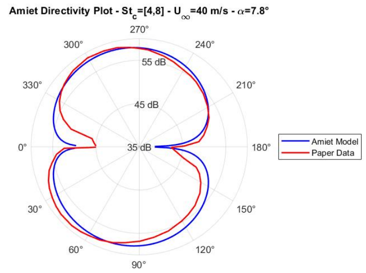

(g) V_∞ = 40 m/s, AoA=7.8°, St=[4,8]

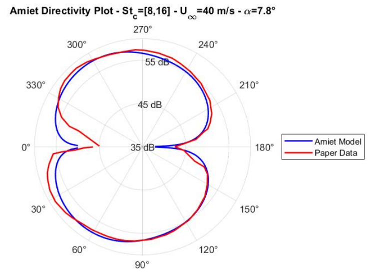

(h) V_∞ = 40 m/s, AoA=7.8°, St=[8,16]

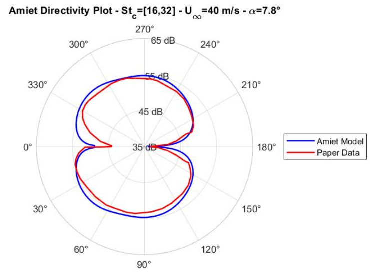

(i) V_∞ = 40 m/s, AoA=7.8°, St=[16,32]

Figure C.2: Directivity trailing edge noise model comparison of Amiet model versus results of the paper of Teruna et al. [78] at distance 1.22 m from the trailing edge.

C.2. BPM MODEL

C.2.1. TURBULENT BOUNDARY LAYER TRAILING EDGE NOISE

NACA0012						
case #	1	2	3	4	5	6
c, m	0.3048				0.1524	
U, m/s	31.7	39.6	55.5	39.6		
α, °	0			4	9.9	12.6
δ_s/c	0.04438	0.04239	0.03975	0.05645	0.28284	0.59579
δ_p/c	0.04438	0.04239	0.03975	0.03000	0.02417	0.02163

Table C.2: Input parameters for the turbulent boundary layer trailing edge noise model.

For the model of the turbulent boundary layer trailing edge noise, the results of six different cases are analyzed. In the report of Brooks, Pope and Marcolini [37], a NACA0012 airfoil is used to obtain data of. The results are obtained for different chord lengths varying from 5.08 cm to 30.48 cm with a span of 45.72 cm. These airfoils are subjected to different velocities and angles of attack. Six of these cases have been selected for this validation, of which the conditions and boundary layer parameters are shown in Table C.2. Note that these values are obtained for the tripped boundary layer. The comparison between the results of the model and the report are shown in Figure C.3.

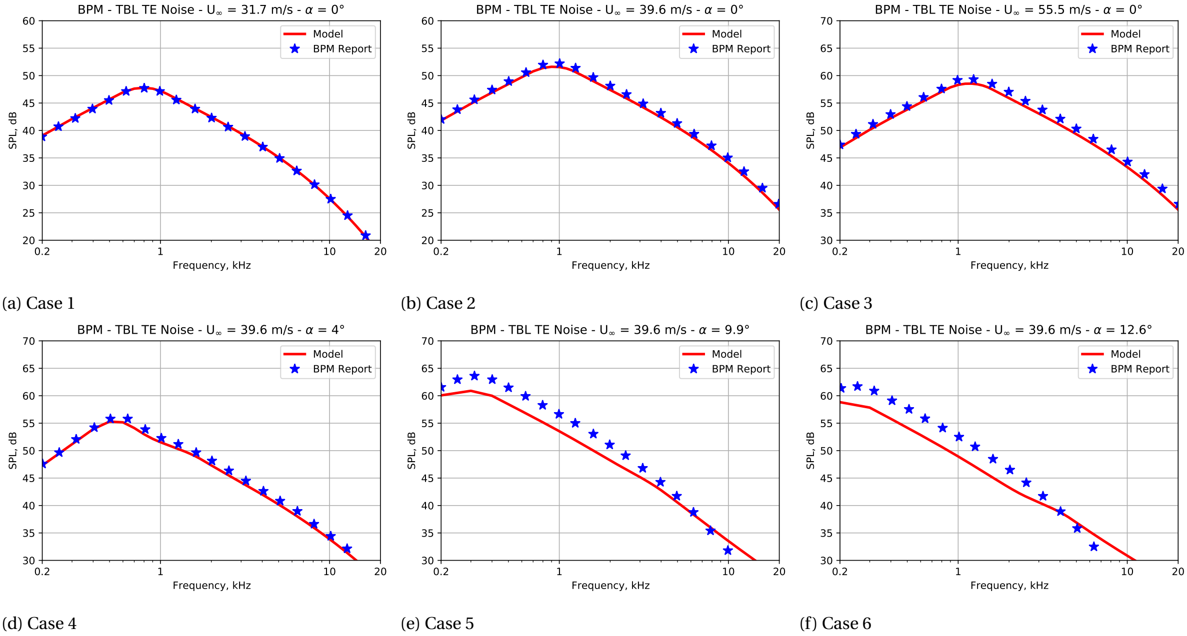

(a) Case 1 (b) Case 2 (c) Case 3

(d) Case 4 (e) Case 5 (f) Case 6

Figure C.3: Turbulent boundary layer trailing edge noise model comparison versus the results of the experimental values in the report of Brooks, Pope and Marcolini [37].

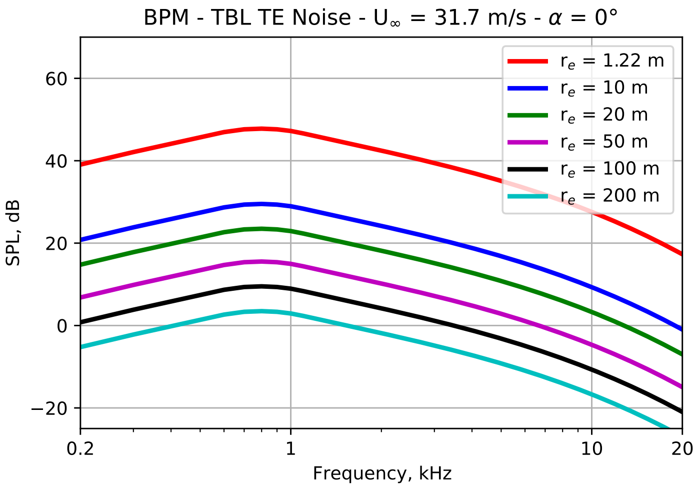

Figure C.4: Turbulent boundary layer trailing edge noise for varying distances.

C.2.2. LAMINAR BOUNDARY LAYER VORTEX SHEDDING NOISE

For the validation of the laminar boundary layer vortex shedding noise model six different cases are considered. In all cases, the airfoil is subjected to a freestream velocity of 39.6 m/s. Half of the cases makes use of an airfoil with a chord of 30.48 cm, while the other half makes use of an airfoil with a chord of 15.24 cm. The angle of attack is varying for each case and ranges from 0° to 3° for the airfoil with the larger chord and ranges from 0° to 7.2° for the smaller chord airfoil.

Important to note is that the BPM report makes use of the untripped boundary layer parameters for the laminar boundary layer vortex shedding noise analyses. The boundary layer parameters used for this analysis can be found in Table C.3.

NACA0012						
case #	1	2	3	4	5	6
c, m	0.3048			0.1524		
U, m/s	39.6					
α, °	0	1.5	3	0	5.4	7.2
δ_p/c	0.02467	0.02148	0.01890	0.02869	0.01833	0.01629

Table C.3: Input parameters for the laminar boundary layer vortex shedding noise model.

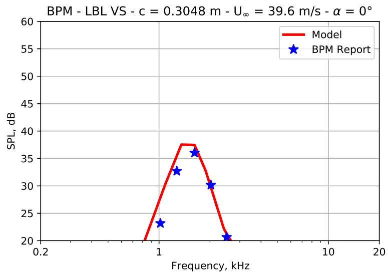

(a) Case 1

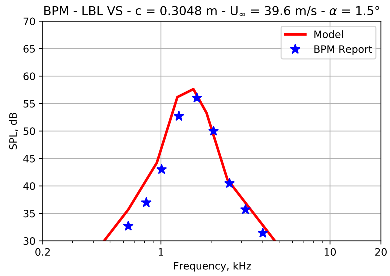

(b) Case 2

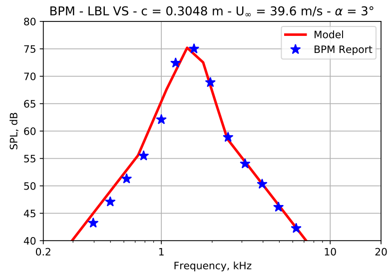

(c) Case 3

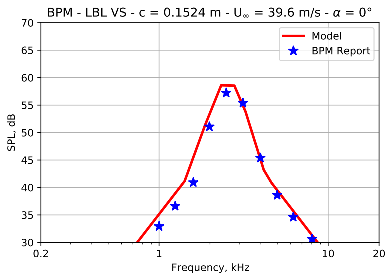

(d) Case 4

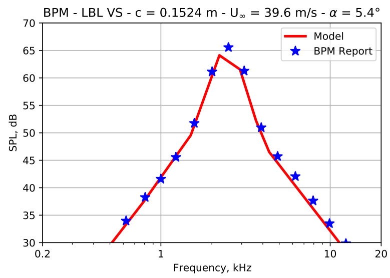

(e) Case 5

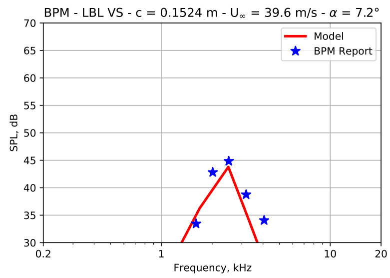

(f) Case 6

Figure C.5: Laminar boundary layer vortex shedding noise model comparison versus the results of the experimental values in the report of Brooks, Pope and Marcolini [37].

C.2.3. BLUNTNESS TRAILING EDGE VORTEX SHEDDING NOISE

The bluntness trailing edge vortex shedding noise is analyzed for three different trailing edge heights ranging from 1.1 mm to 2.5 mm. The chord length of this airfoil is equal to 60.96 cm and the freestream velocity is set to 38.6 m/s. For this noise source, the BPM report [37] makes use of the tripped boundary layer conditions again, for which the input parameters can be found in Table C.4.

NACA0012			
case #	1	2	3
c, m	0.6096		
U, m/s	38.6		
α, °	0		
h_{TE}, mm	1.1	1.9	2.5
$\delta*_s$/c	0.00860		
$\delta*_p$/c	0.00860		

Table C.4: Input parameters for the bluntness trailing edge vortex shedding noise model.

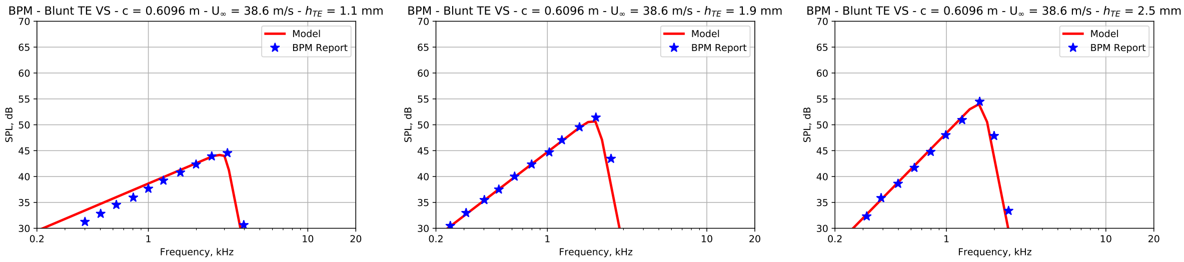

(a) Case 1

(b) Case 2

(c) Case 3

Figure C.6: Bluntness trailing edge vortex shedding noise model comparison versus the results of the experimental values in the report of Brooks, Pope and Marcolini [37].

C.2.4. TIP VORTEX FORMATION NOISE

The tip noise is compared to data prediction made in the report of Brooks, Pope and Marcolini [37], as the experimental data does not include the tip noise. The prediction is applied to a 0.1524 m chord airfoil with a span of 0.3848 m, which is subjected to a freestream velocity of 71.3 m/s. The angle of the tip is set to 7.668°.

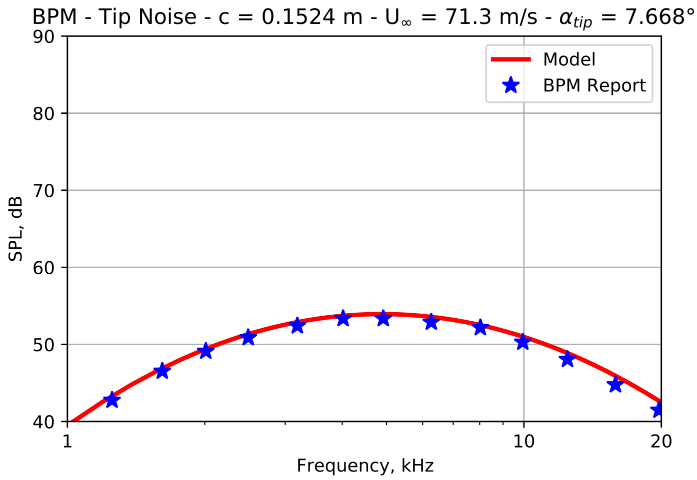

Figure C.7: Tip noise model comparison versus the results of the predicted values in the report of Brooks, Pope and Marcolini [37].

D
Sensitivity Analysis Analytical Methods

D.1. Input Parameters

Case #	1	2	3	4	5	6	7	8	9	10	11	12
Boundary layer characteristic	Laminar			Turbulent			TBL with increased PS			TBL with increase SS		
Freestream velocity, m/s	20	40	60	20	40	60	20	40	60	20	40	60

Table D.1: Sensitivity analysis BPM cases input.

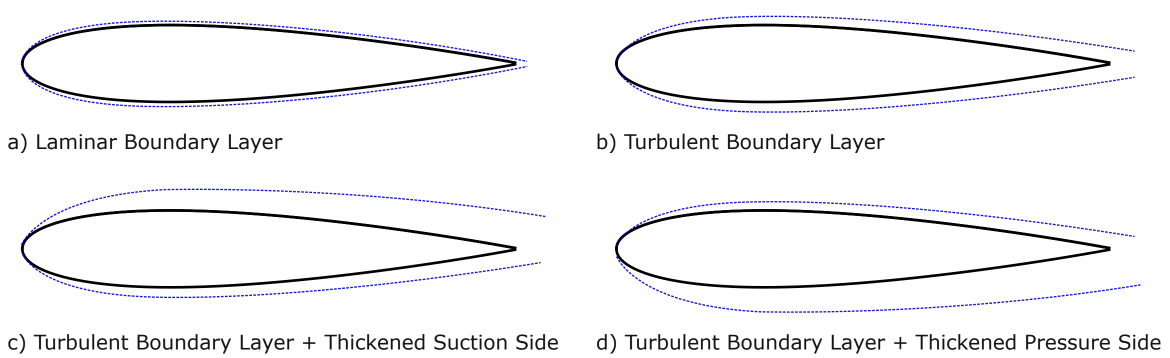

Figure D.1: Visualization of the boundary layer characteristics.

The sensitivity analysis of the BPM model is carried out for 12 cases, which vary the boundary layer characteristics and freestream velocity. For this analysis, the chord is set to be equal to 0.5 m, the span equal to 1 m and the trailing edge height at 0.1 mm. The freestream velocities are ranging from 20 m/s to 60 m/s. For the boundary layer, four different situations are considered: laminar boundary layer, turbulent boundary layer and turbulent boundary layers for which in one case the pressure side (PS) boundary layer height is increased and for the other case the suction side (SS) boundary layer height is increased. To get a better understanding of what the boundary layer of each type looks like, a visualization of each type is shown in Figure D.1. Please note that the presented figure is intended to solely visualize the different boundary layer heights and is not based on any specific real-world case. The situation for which the pressure side of the boundary layer is thickened, is particularly interesting for the LEI kite, as the recirculation zone could induce a thickening at the trailing edge of the kite. The characteristics of each case are given in Table D.1. The boundary layer parameters are obtained by making use of the equations given in Subsection 3.1.3. Note that for all cases in this sensitivity analysis, the angle of attack is kept at 5°.

For the sensitivity analysis of the Amiet model, three factors will be varied: Reynolds number, angle of attack and the boundary layer characteristics, meaning tripped or untripped boundary layers. This analysis makes use of the NACA0012 with the same span and chord as that for the BPM sensitivity analysis. Unlike the BPM analysis, the boundary layer parameters are obtained from XFoil [76]. In total, the sensitivity analysis of the Amiet model will look at 6 different cases for which the characteristics are shown in Table D.2.

Case #	1	2	3	4	5	6
Freestream velocity, m/s	20	40	60	40		
Angle of Attack, °	0			5	10	0
Tripped/Untripped	untripped					tripped

Table D.2: Sensitivity analysis Amiet cases input.

D.2. AMIET MODEL

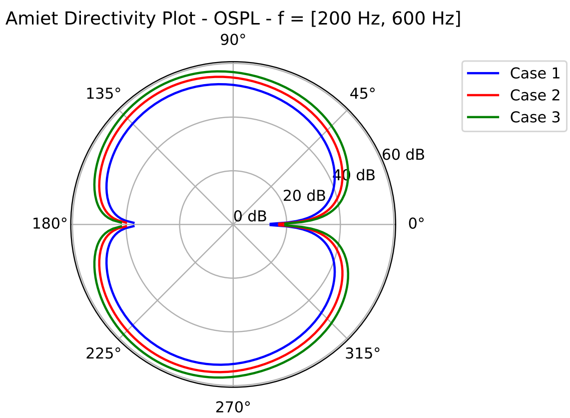

(a)

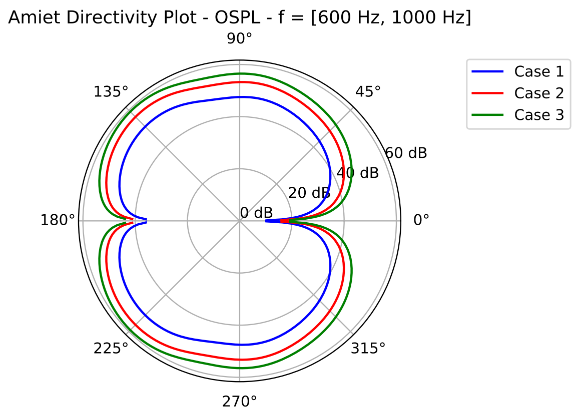

(b)

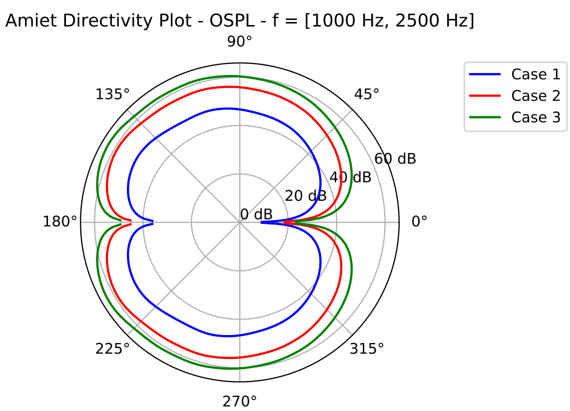

(c)

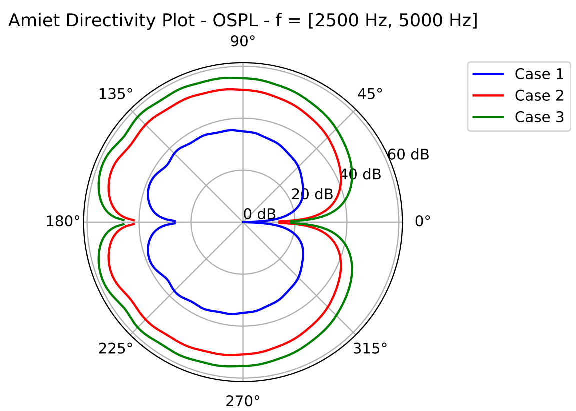

(d)

Figure D.2: Amiet model sensitivity study results

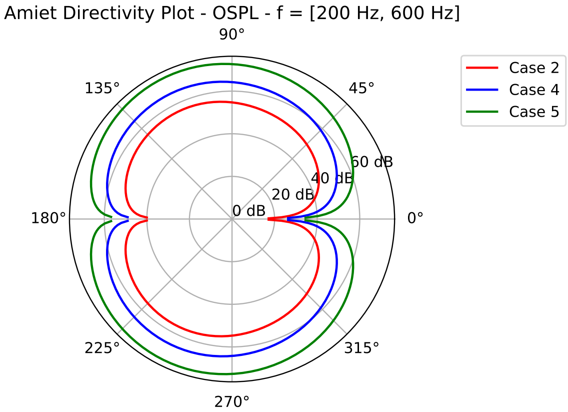

(e)

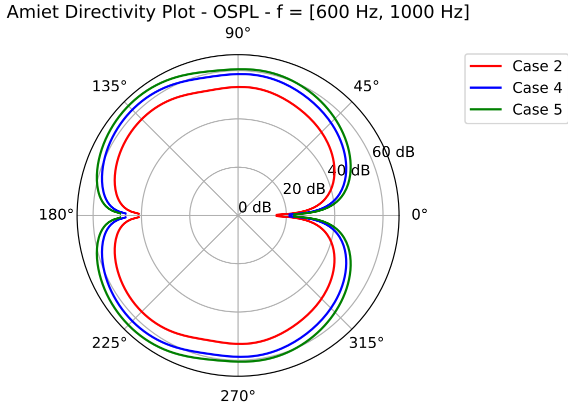

(f)

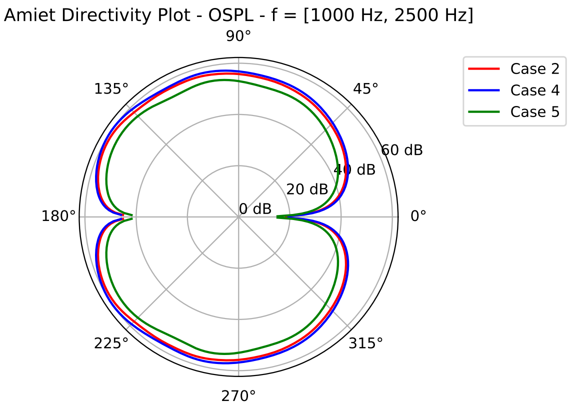

(g)

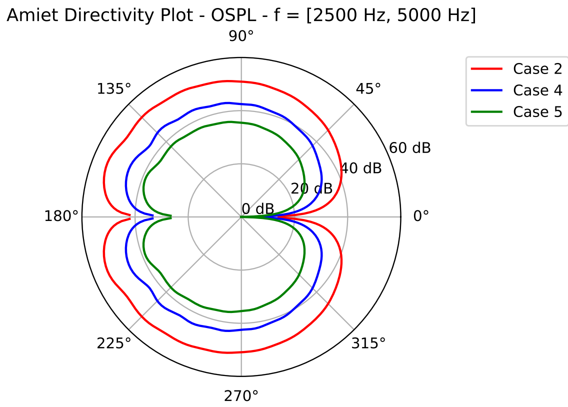

(h)

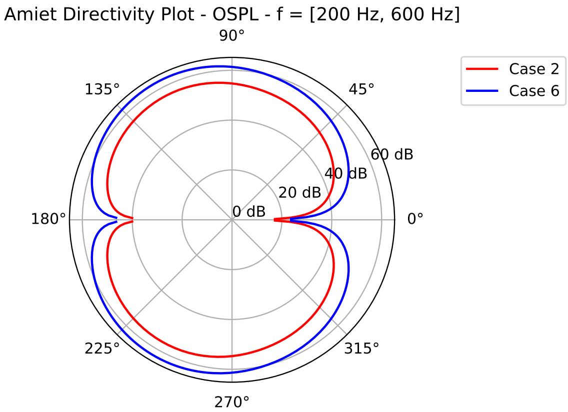

(i)

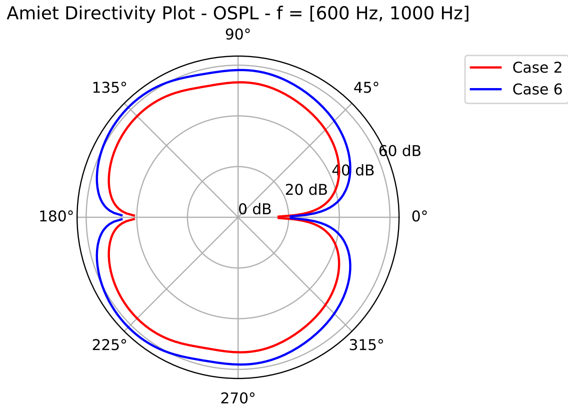

(j)

Figure D.2: Amiet model sensitivity study results (continued)

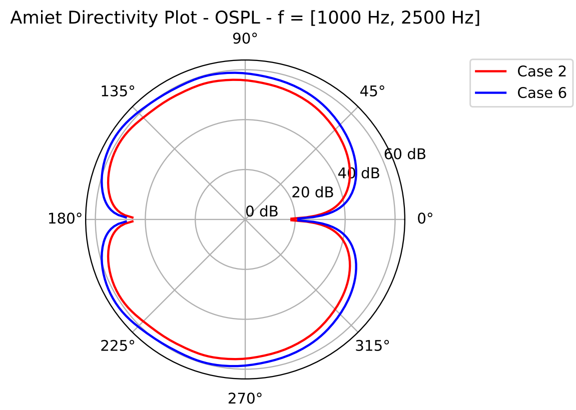

(k)

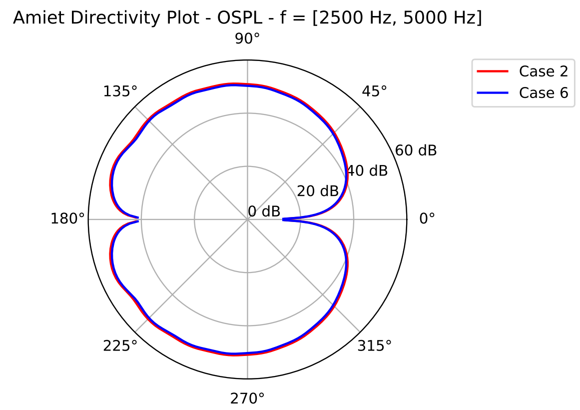

(l)

Figure D.2: Amiet model sensitivity study results (continued)

D.3. BPM MODEL

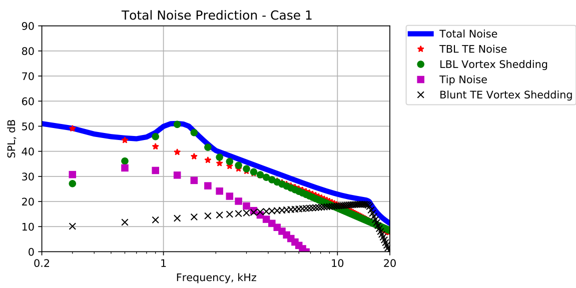

(a) Case 1

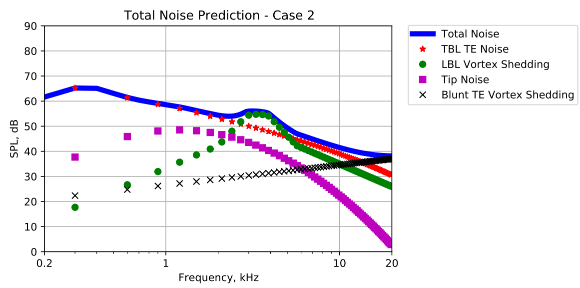

(b) Case 2

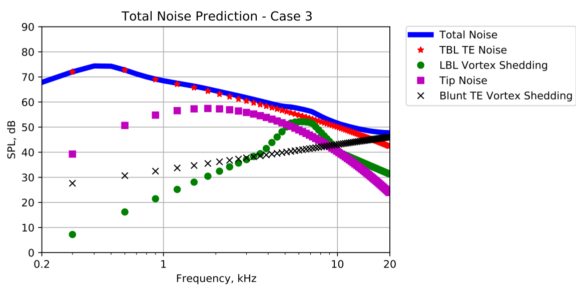

(c) Case 3

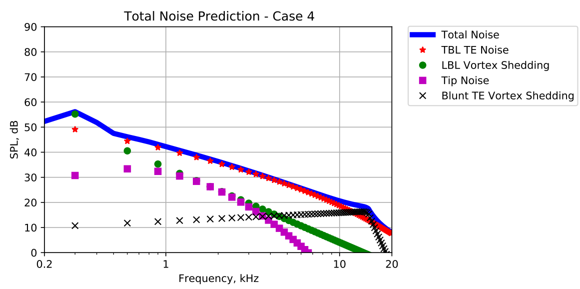

(d) Case 4

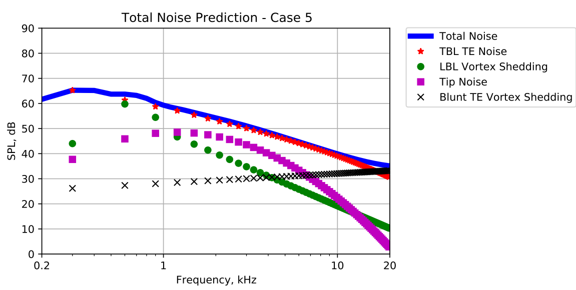

(e) Case 5

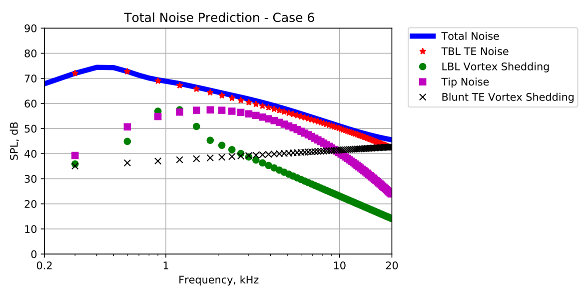

(f) Case 6

Figure D.3: BPM model sensitivity study results

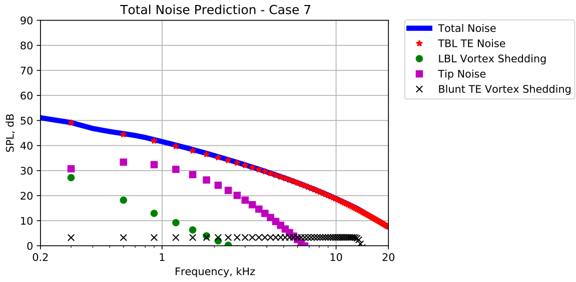

(g) Case 7

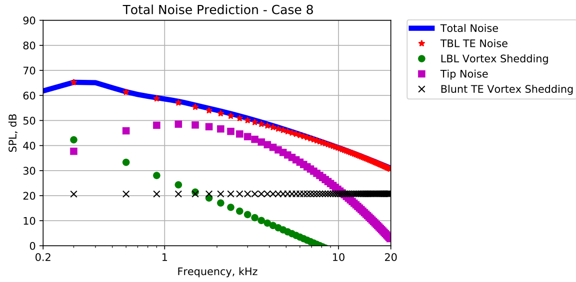

(h) Case 8

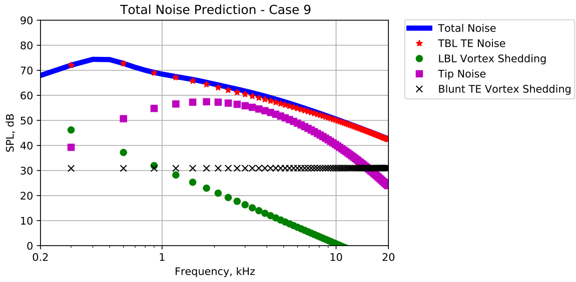

(i) Case 9

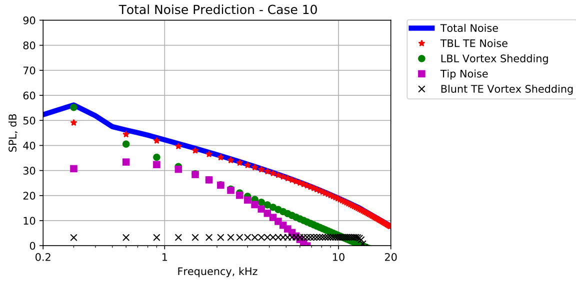

(j) Case 10

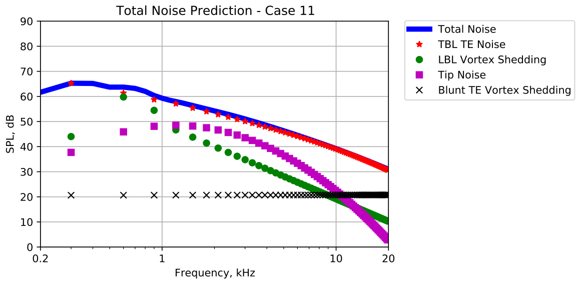

(k) Case 11

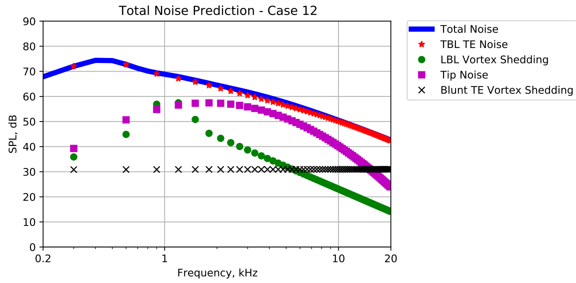

(l) Case 12

Figure D.3: BPM model sensitivity study results (continued)

Bibliography

[1] A. Van Gries. "Durch Drachen getragene Windkraftmaschine zur Nutzbarmachung von Höhenwinden". Patent DE656194. 1935.

[2] W. Schmidt and W. Anderson. "Kites: Pioneers of Atmospheric Research". In: *Airborne Wind Energy* (2013), pp. 95–116. DOI: 10.1007/978-3-642-39965-7_6.

[3] H. Oberth. "Verbessertes Drachenkraftwerk". Patent Application DE2720339. 1977.

[4] M. L. Loyd. "Crosswind Kite Power (for large-scale wind power production)". In: *Journal of Energy* 4.3 (1980), pp. 106–111. DOI: 10.2514/3.48021.

[5] European Commission. *Questions and Answers on emergency measures to accelerate the deployment of renewable energy*. November 2022. URL: https://ec.europa.eu/commission/presscorner/detail/en/qanda_22_6658.

[6] International Energy Agency. *Renewable Energy Market Update*. May 2022. URL: https://www.iea.org/reports/renewable-energy-market-update-may-2022.

[7] Earth.Org. *Top 5 Fastest-Growing Renewable Energy Sources Around the World*. May 2021. URL: https://earth.org/fastest-growing-renewable-energy-sources/.

[8] The Guardian. *Timeline: The history of wind power*. October 2008. URL: https://www.theguardian.com/environment/2008/oct/17/wind-power-renewable-energy.

[9] S. Deshmukh et al. *Wind turbine noise and its mitigation techniques: A review*. February 2019. DOI: 10.1016/j.egypro.2019.02.215.

[10] Rampion Offshore Wind Farm. *Wind turbine generators | Rampion Offshore Wind*. March 2018. URL: https://www.rampionoffshore.com/wind-farm/components/turbines/.

[11] Hale Trailer Brake and Wheel. *Wind turbine blade sizes and transport: A guide*. May 2022. URL: https://www.utilitydive.com/spons/wind-turbine-blade-sizes-and-transport-a-guide/623444/.

[12] Softlean ERP. *Location Of Wind Turbines With The Most Favourable Local Conditions*. February 2020. URL: http://softleanerp.com/2018/07/18/location-of-wind-turbines-with-the-most-favourable-local-conditions/.

[13] Kitepower. *Kitepower Falcon 100kW Airborne Wind Energy System*. April 2022. URL: https://thekitepower.com/product/.

[14] *About Airborne Wind Energy – Airborne Wind Europe*. URL: https://airbornewindeurope.org/about-airborne-wind-energy/.

[15] L. Fagiano et al. *The International Airborne Wind Energy Conference 2021: Book of Abstracts*. Conference Paper. Milan, Italy, June 2022. DOI: 10.4233/uuid:696eb599-ab9a-4593-aedc-738eb14a90b3.

[16] H. Schmidt et al. "The Social Acceptance of Airborne Wind Energy: A Literature Review". In: *Energies* 15.4 (2022). DOI: 10.3390/en15041384.

[17] R. Schmehl. *Airborne Wind Energy: An introduction to an emerging technology*. June 2019. URL: https://awesco.eu/awe-explained/.

[18] F. Friedl. *Fault-Tolerant Design of a Pumping Kite Power Flight Control System*. Master Thesis. February 2015. URL: http://resolver.tudelft.nl/uuid:e704e8aa-2371-437b-8de9-80b3b7067241.

[19] E. Oland and A. van der Brink. *Technical Progress in Kitemill*. Conference Paper. June 2022. URL: http://resolver.tudelft.nl/uuid:39e797a0-7959-44bb-9ccf-efb5351123d4.

[20] R. Bosman et al. "Airborne wind energy tethers with high-modulus polyethylene fibers". In: *Airborne Wind Energy* (2013), pp. 563–585. DOI: 10.1007/978-3-642-39965-7_33.

[21] Kitemill AS. *Great Performance Statistics*. June 2022. URL: https://www.kitemill.com/news/energy-produced-during-testing.

[22] Kitepower. *Kitepower Falcon 100kw airborne wind energy system*. April 2022. URL: https://thekitepower.com/product/.

[23] Kitepower. *Kitepower-25-40-60-sqm-kites*. February 2019. URL: https://assets.change.inc/images/_850x478_crop_center-center_none/476421/Kitepower_25_40_60_sqm_kites-1.webp.

[24] V. Salma, F. Friedl, and R. Schmehl. "Improving reliability and safety of Airborne Wind Energy Systems". In: *Wind Energy* 23.2 (2019), pp. 340–356. DOI: 10.1002/we.2433.

[25] J. Oehler and R. Schmehl. "Aerodynamic characterization of a soft kite by in situ flow measurement". In: *Wind Energy Science* 4.1 (2019), pp. 1–21. DOI: https://doi.org/10.5194/wes-4-1-2019.

[26] R. van der Vlugt, J. Peschel, and R. Schmehl. "Design and experimental characterization of a pumping kite power system". In: *Airborne Wind Energy* (2013), pp. 403–425. DOI: 10.1007/978-3-642-39965-7_23.

[27] J. Oehler et al. *Kite power flight data acquired on 24 March 2017*. Data Set. 2018. DOI: 10.4121/uuid:37264fde-2344-4af2-860c-effda9caa3e8.

[28] R. van der Vlugt et al. "Quasi-steady model of a pumping kite power system". In: *Renewable Energy* 131 (2019), pp. 83–99. DOI: 10.1016/j.renene.2018.07.023.

[29] R. Leuthold. *Multiple-Wake Vortex Lattice Method for Airborne Wind Energy Membrane-Wing Kites*. Master Thesis. March 2015. URL: http://resolver.tudelft.nl/uuid:4c2f34c2-d465-491a-aa64-d991978fedf4.

[30] A. Szücs. *Acoustic impact of airborne wind energy technology on the environment*. Bachelor Thesis. 2017. DOI: https://doi.org/10.5281/zenodo.7851787.

[31] Kitemill AS. *The solution*. URL: https://www.kitemill.com/the-solution.

[32] S. Goldstein. *Modern Developments in Fluid Dynamics, Vol. 2*. Dover Publications, 1938.

[33] S. B. Cunha et al. "Pipeline Viv: Analytical solution, experiments and parameter identification". In: *Volume 5: Polar and Arctic Sciences and Technology; CFD and VIV* (2009). DOI: 10.1115/omae2009-79756.

[34] S. Dunker. "Tether and Bridle Line Drag in Airborne Wind Energy Applications". In: *Airborne Wind Energy* (2018), pp. 29–56. DOI: 10.1007/978-981-10-1947-0_2.

[35] R. King. "A review of vortex shedding research and its application". In: *Ocean Engineering* 4.3 (1977), pp. 141–171. DOI: 10.1016/0029-8018(77)90002-6.

[36] S. Dunker, W. Meile, and G. Brenn. "Experiments in Line Vibration and Associated Drag for Kites". In: *23rd AIAA Aerodynamic Decelerator Systems Technology Conference* (2015). DOI: 10.2514/6.2015-2154.

[37] T. Brooks, D. Pope, and M. Marcolini. "Airfoil self-noise and prediction". In: *NASA Reference Publication* (July 1989).

[38] C. Doolan and D. Moreau. "Airfoil Noise Mechanisms and Control". In: *Flow Noise: Theory*. Springer Nature Singapore, 2022. ISBN: 978-981-19-2484-2. DOI: 10.1007/978-981-19-2484-2_8.

[39] S. Lee et al. "Turbulent boundary layer trailing-edge noise: Theory, computation, experiment, and application". In: *Progress in Aerospace Sciences* 126 (2021). DOI: 10.1016/j.paerosci.2021.100737.

[40] S. Pröbsting. Doctoral Thesis. 2015. URL: http://resolver.tudelft.nl/uuid:8a938547-a829-4a79-b77c-a92633a9652a.

[41] D. Moreau and C. Doolan. *An experimental study of airfoil tip vortex formation noise*. Conference Paper. November 2016. URL: http://www.acoustics.asn.au/conference_proceedings/AASNZ2016/papers/p29.pdf.

[42] Y. Lian et al. "Membrane wing aerodynamics for micro air vehicles". In: *Progress in Aerospace Sciences* 39.6-7 (2003), pp. 425–465. DOI: 10.1016/s0376-0421(03)00076-9.

[43] J. N. Nielsen. "Theory of Flexible Aerodynamic Surfaces". In: *Journal of Applied Mechanics* 30.3 (1963), pp. 435–442. DOI: 10.1115/1.3636575.

[44] M. Mendenhall, S. Spangler, and N. Nielsen. *Investigation of Methods for Predicting the Aerodynamic Characteristics of Two-Lobed Parawings*. Technical Report. September 1968. URL: https://ntrs.nasa.gov/api/citations/19680024293/downloads/19680024293.pdf.

[45] B. Newman and H. Low. "Two-dimensional impervious sails: experimental results compared with theory". In: *Journal of Fluid Mechanics* 144 (1984), pp. 445–462. DOI: 10.1017/s0022112084001683.

[46] M. Folkersma, R. Schmehl, and A. Viré. "Boundary layer transition modeling on leading edge inflatable kite airfoils". In: *Wind Energy* (2019). DOI: 10.1002/we.2329.

[47] TU Delft. *Zig-zag seams along the attachment of the canopy to the leading edge tube - TU Delft V3 kite*. May 2013.

[48] M. Howe. "Structural and acoustic noise produced by turbulent flow over an elastic trailing edge". In: *Proceedings of the Royal Society of London. Series A: Mathematical and Physical Sciences* 442.1916 (1993), pp. 533–554. DOI: 10.1098/rspa.1993.0120.

[49] R. Nardini M.and Sandberg and S. Schlanderer. "Computational study of the effect of structural compliance on the noise radiated from an elastic trailing-edge". In: *Journal of Sound and Vibration* 485 (2020). DOI: 10.1016/j.jsv.2020.115533.

[50] C. Pimenta, W. Wolf, and A. Cavalieri. "A fast numerical framework to compute acoustic scattering by poroelastic plates of arbitrary geometry". In: *Journal of Computational Physics* 373 (2018), pp. 763–783. DOI: 10.1016/j.jcp.2018.07.019.

[51] Nilton, M. et al. "Effects of structural damping on acoustic scattering by flexible plates". In: *Proceedings of the Royal Society A: Mathematical, Physical and Engineering Sciences* 475.2230 (2019), p. 20190285. DOI: 10.1098/rspa.2019.0285.

[52] M. Khorrami and D. Lockard. "Effects of Geometric Details on Slat Noise Generation and Propagation". In: *International Journal of Aeroacoustics* 9.4-5 (June 2010), pp. 655–678. DOI: 10.1260/1475-472x.9.4-5.655.

[53] Chen, G. et al. "Noise control for high-lift devices by slat wall treatment". In: *Aerospace Science and Technology* 115 (August 2021). DOI: 10.1016/j.ast.2021.106820.

[54] M. Dereta. *Kite control with GoPro video camera mounted to record kite and bridle dynamics during flight*. 2012. URL: http://www.kitepower.eu/images/stories/technology/system_components/kitecontrol/controlunit_in_flight2.jpg.

[55] M. Matsumoto. "VORTEX SHEDDING OF BLUFF BODIES: A REVIEW". In: *Journal of Fluids and Structures* 13.7-8 (1999), pp. 791–811. DOI: 10.1006/jfls.1999.0249.

[56] M. Sarioglu and T. Yavuz. "Vortex shedding from circular and rectangular cylinders placed horizontally in a turbulent flow". In: *Turkish Journal of Engineering and Environmental Sciences* 24 (January 2000), pp. 217–228.

[57] National Oceanic and Atmospheric Administration, National Aeronautics and Space Administration, and United States Air Force. *U.S. Standard Atmosphere, 1976*. Technical Report. October 1976. URL: https://www.ngdc.noaa.gov/stp/space-weather/online-publications/miscellaneous/us-standard-atmosphere-1976/us-standard-atmosphere_st76-1562_noaa.pdf.

[58] D. Kurtz. *A review of aerodynamic noise from propellers, rotors, and lift fans - NASA Technical Reports Server (NTRS)*. Technical Report. January 1970. URL: https://ntrs.nasa.gov/api/citations/19700005920/downloads/19700005920.pdf.

[59] B. Marinus. "Multidisciplinary Optimization of Aircraft Propeller Blades". PhD Thesis. November 2011. URL: https://acoustique.ec-lyon.fr/publi/marinius_thesis.pdf.

[60] M. Haddaoui. *Development of a Propeller Source Noise Model*. July 2019. URL: http://resolver.tudelft.nl/uuid:f8e13c98-08b6-4280-ad2d-034fd8a6b63e.

[61] B. Magliozzi, D. Hanson, and R. Amiet. *Aeroacoustics of Flight Vehicules: Theory and Practice*. WRDC Technical Report. August 1991, pp. 90–3052. URL: https://ntrs.nasa.gov/api/citations/19920001380/downloads/19920001380.pdf.

[62] L. Hannah. “Ground, Terrain and Structure Effects on Sound Propagation”. In: *New Zealand Acoustics* 20.3 (2007). URL: https://www.acoustics.org.nz/sites/www.acoustics.org.nz/files/journal/pdfs/Hannah_L_NZA2007_c.pdf.

[63] R. Amiet. “Noise due to turbulent flow past a trailing edge”. In: *Journal of Sound and Vibration* 47.3 (1976), pp. 387–393. DOI: 10.1016/0022-460x(76)90948-2.

[64] R. Amiet. “Acoustic radiation from an airfoil in a turbulent stream”. In: *Journal of Sound and Vibration* 41.4 (1975), pp. 407–420. DOI: 10.1016/s0022-460x(75)80105-2.

[65] M. Roger and S. Moreau. “Back-scattering correction and further extensions of Amiet’s trailing-edge noise model. part 1: Theory”. In: *Journal of Sound and Vibration* 286.3 (2005), pp. 477–506. DOI: 10.1016/j.jsv.2004.10.054.

[66] D. Casalino and M. Barbarino. “A stochastic method for airfoil self-noise computation in frequency-domain”. In: *16th AIAA/CEAS Aeroacoustics Conference* (2010). DOI: 10.2514/6.2010-3884.

[67] S. Lee. “Empirical wall-pressure spectral modeling for zero and adverse pressure gradient flows”. In: *AIAA Journal* 56.5 (2018), pp. 1818–1829. DOI: 10.2514/1.j056528.

[68] G. Corcos. “The structure of the turbulent pressure field in boundary-layer flows”. In: *Journal of Fluid Mechanics* 18.03 (1964), p. 353. DOI: 10.1017/s002211206400026x.

[69] R. Amiet. “Noise due to turbulent flow past a trailing edge”. In: *Journal of Sound and Vibration* 47.3 (1976), pp. 387–393. DOI: 10.1016/0022-460x(76)90948-2.

[70] T. Brooks and T. Hodgson. “Trailing edge noise prediction from measured surface pressures”. In: *Journal of Sound and Vibration* 78.1 (1981), pp. 69–117. DOI: 10.1016/s0022-460x(81)80158-7.

[71] P. Garcia and P. Gérard. “Bruit d’un Profil dans un Écoulement”. In: *La Recherche Aérospatiale* 3 (1989), pp. 1–7.

[72] S. Pérennès and M. Roger. “Aerodynamic Noise of a Two-Dimensional Wing with High-Lift Devices”. In: *AIAA Paper* 98-2338 (1998).

[73] S. Moreau and M. Roger. “Effect of Airfoil Aerodynamic Loading on Trailing Edge Noise”. In: *AIAA Journal* 1 (2005). DOI: https://doi.org/10.2514/1.5578.

[74] Y. Rozenberg, G. Robert, and S. Moreau. “Wall-Pressure Spectral Model Including the Adverse Pressure Gradient Effects”. In: *AIAA Journal* 50.10 (October 2012), pp. 2168–2179. DOI: http://dx.doi.org/10.2514/1.J051500.

[75] O. Stalnov, P. Chaitanya, and P. Joseph. “Towards a non-empirical trailing edge noise prediction model”. In: *Journal of Sound and Vibration* 372 (2016), pp. 50–68. DOI: 10.1016/j.jsv.2015.10.011.

[76] M. Drela. *XFOIL: An Analysis and Design System for Low Reynolds Number Arifoils*. Technical Report. 1989. URL: https://web.mit.edu/drela/Public/papers/xfoil_sv.pdf.

[77] J. Anderson. *Fundamentals of aerodynamics*. McGraw-Hill Education, 2011.

[78] C. Teruna et al. “On the noise reduction of a porous trailing edge applied to an airfoil at lifting condition”. In: *Physics of Fluids* 33.5 (May 2021). DOI: 10.1063/5.0047512.

[79] T. F. Brooks and M. A. Marcolini. “Airfoil Tip Vortex Formation Noise”. In: *AIAA Journal* 24.2 (1986), pp. 246–252. DOI: 10.2514/3.9252.

[80] H. Fujita. “The characteristics of the aeolian tone radiated from two-dimensional cylinders”. In: *Fluid Dynamics Research* 42.1 (2010), p. 015002. DOI: 10.1088/0169-5983/42/1/015002.

[81] C. Norberg. “Fluctuating lift on a circular cylinder: Review and New Measurements”. In: *Journal of Fluids and Structures* 17.1 (2003), pp. 57–96. DOI: 10.1016/s0889-9746(02)00099-3.

[82] E. Latorre Iglesias, D. Thompson, and M. Smith. “Experimental study of the aerodynamic noise radiated by cylinders with different cross-sections and yaw angles”. In: *Journal of Sound and Vibration* 361 (2016), pp. 108–129. DOI: 10.1016/j.jsv.2015.09.044.

[83] M. Long. “Fundamentals of Acoustics”. In: *Architectural Acoustics* (2014), pp. 39–79. DOI: 10.1016/b978-0-12-398258-2.00002-7.

[84] M. Pawlaczyk-Łuszczyńska et al. “Response to noise emitted by wind farms in people living in nearby areas”. In: *International Journal of Environmental Research and Public Health* 15.8 (2018), p. 1575. DOI: 10.3390/ijerph15081575.

[85] S. Brezas and V. Wittstock. "Factors that affect the sound power emitted by reference sound sources". In: *DAGA Nürnberg* (2015). DOI: https://www.ptb.de/cms/fileadmin/internet/fachabteilungen/abteilung_1/1.7_angewandte_akustik/1.72/Publikationen/2015/2015_BRZ_DAGA_Factors_that_affect_the_sound_power_emitted_by_reference_sound_sources..pdf.

[86] R. B. Randall. *Frequency analysis*. Brüel et Kjaer, 1987. ISBN: 8787355078.

[87] Brüel et Kjaer. *Technical Documentation - Hand-held Analyzer Types 2250, 2250-L and 2270 with Microphone Type 4189 - Instruction Manual*. February 2015.

[88] S. Boll. "Suppression of acoustic noise in speech using spectral subtraction". In: *IEEE Transactions on Acoustics, Speech, and Signal Processing* 27.2 (1979), pp. 113–120. DOI: 10.1109/tassp.1979.1163209.

[89] B. McCarthy. *Sound Systems - Design and optimization: Modern techniques and tools for sound system design and alignment*. Focal Press, 2016.

[90] H. Zumbahlen. *Linear Circuit Design Handbook*. Newnes, 2008.

[91] R. G. Lyons. *Understanding Digital Signal Processing*. Pearson Education International, 2013.

[92] D. Johnson. *Electrical Engineering*. Rice University, 2023. URL: https://eng.libretexts.org/@go/page/11984?pdf.

[93] F. Harris. "On the use of windows for harmonic analysis with the discrete Fourier transform". In: *Proceedings of the IEEE* 66.1 (1978), pp. 51–83. DOI: 10.1109/proc.1978.10837.

[94] W. H. Press et al. *Numerical recipes: The art of scientific computing*. Cambridge University Press, 2007.

[95] D. Simons and M. Snellen. "Chapter 3 Propagation of sound in the atmosphere". In: *Aircraft Noise and Emissions*. TU Delft, July 2020, pp. 40–109.

[96] T. Geyer, E. Sarradj, and C. Fritzsche. "Measurement of the noise generation at the trailing edge of porous airfoils". In: *Experiments in Fluids* 48.2 (2009), pp. 291–308. DOI: 10.1007/s00348-009-0739-x.

[97] A. Martyr and D. Rogers. *Engine testing: Electrical, hybrid, IC engine and Power Storage Testing and Test Facilities*. Butterworth-Heinemann, an imprint of Elsevier, 2021.

[98] I. E. Commision. "International Standard IEC 61672-1:2013". In: *Electroacoustics - Sound level meters* (2013).

[99] R. Schmehl and J. Oehler. Video. 2018. DOI: https://doi.org/10.5446/37583.

[100] S. Oerlemans. "Wind tunnel aeroacoustic tests of six airfoils for use on small wind turbines; period of performance: August 23, 2002 through March 31, 2004". In: *Subcontractor report NREL/SR-500- 35339, National Renewable Energy Laboratory* (2004). DOI: 10.2172/15007773.

[101] J. Nebres and S. Batill. "Flow around a cylinder with a spanwise large-scale surface perturbation". In: *31st Aerospace Sciences Meeting* (1993). DOI: 10.2514/6.1993-657.

[102] K. P. Griffin, L. Fu, and P. Moin. "General method for determining the boundary layer thickness in nonequilibrium flows". In: *Physical Review Fluids* 6 (2 February 2021). DOI: 10.1103/PhysRevFluids.6.024608.

[103] E. Houghton et al. "Chapter 3 - Viscous Flow and Boundary Layers". In: *Aerodynamics for Engineering Students (Seventh Edition)*. Ed. by E. Houghton et al. Seventh Edition. Butterworth-Heinemann, 2017, pp. 151–254. DOI: https://doi.org/10.1016/B978-0-08-100194-3.00003-1.

[104] Ç. Y. A. and J. M. Cimbala. *Fluid Mechanics: Fundamentals and Applications*. McGraw-HillHigher Education, 2006.

[105] H. Hafeez and C. Ndikilar. "4 - Boundary layer equations in fluid dynamics". In: *Applications of Heat, Mass and Fluid Boundary Layers*. Woodhead Publishing, 2020, pp. 67–94. DOI: https://doi.org/10.1016/B978-0-12-817949-9.00012-8.

[106] F. M. White. *Fluid mechanics*. McGraw-Hill, 2016.

[107] J. Cousteix. "Aircraft Aerodynamic Boundary Layers". In: *Encyclopedia of Physical Science and Technology (Third Edition)*. Ed. by R. A. Meyers. Third Edition. New York: Academic Press, 2003, pp. 301–317. ISBN: 978-0-12-227410-7. DOI: https://doi.org/10.1016/B0-12-227410-5/00906-6.

[108] M. Potter, D. Wiggert, and B. Ramadan. *Mechanics of Fluids: si edition*. 2016.